UNIVERSITÀ DEGLI STUDI DI PADOVA
DIPARTIMENTO DI FISICA: "GALILEO GALILEI"
FACOLTÀ DI SCIENZE MM.FF.NN.

Tesi di Laurea Magistrale in Fisica

Search for Heavy Stable Charged Particles in the CMS experiment exploiting the time resolution of the Drift Tube chambers.

RELATORE: Prof.ssa Anna T. Meneguzzo

CORRELATORE: Prof. Roberto Carlin

LAUREANDO: Marco Meneghelli

Anno Accademico 2008–2009

Contents

List of Figures

Preface

The Standard Model (SM) of elementary interactions, a quantum field theory based on symmetry principles, has been tested with exquisite precision in a large class of experiments. Its predictive power has been verified up to the second order of precision for the electroweak sector, while the predictions relative to flavor physics result so strong that the Nobel prize 2008 has been assigned to scientists that introduced into the SM the possibility of flavor oscillations. However there are still various open questions. Has the SM to be considered as a nature basic theory? The Higgs boson, predicted by the theory and responsible for both electroweak spontaneous symmetry breaking and masses of all the other particles, has not been found despite the direct searches at LEP and Tevatron. Otherwise there are also many reasons for considering the SM to be an effective theory under the TeV scale: by looking at the high energy physics together by considering some cosmological problems it seems that many of the SM predictions are phenomenological manifestations of more "elementary" processes. For this reason a large amount of theories for physics beyond the SM have arisen for the last decades by composing what nowadays is called generally "new physics".

In order to give answers to these problems the "Large Hadron Collider" (LHC), at Geneva CERN, the most powerful high energy physics machine, has been built. At the LHC the protons will collide with a center of mass energy of 14 TeV, one order of magnitude more than the most powerful collisions actually existing. One of the four experiments built along the LHC circumference is the "Compact Muon Solenoid" (CMS). It has been designed with the aim of looking for every signal of new physics around the TeV scale in addition to search for the Higgs boson.

This thesis is an experimental work on the possibility of searching for new "exotica" Heavy Stable Charged Particles (HSCP) at the CMS experiment using the Drift Tube chambers of the barrel (DT). The HSCPs, predicted by several theoretical models, are characterized by low speed ($\beta \sim 0.5$) together with high momentum. We are interested in the electrically charged HSCPs that behave like muons, crossing the whole CMS detector. We can separate HSCPs from muons by measuring the speed of particles detected

in the muon system.

The Drift Tube chambers allow a reconstruction of tracks segments that assigns a time parameter together with the position and slope. From this we can infer the absolute time of passage of a particle in a chamber: if we have a good resolution it will be possible to discriminate the kind of particles by measuring their speed.

The first two chapters of the thesis present the LHC and CMS. Their main physical goals and experimental apparatus are presented. In the second chapter the Drift Tube chambers are described in detail since all our experimental work is based on the data collected by these detectors. Particular relevance is reserved to DT structure and electronic local trigger system description.

In order to perform every physical analysis at CMS, the detecting system must be optimize in terms of data selecting, data acquisition and event reconstruction. The third chapter of the thesis is devoted to a study on the DT trigger chain fine synchronization performed using cosmic data. The opportunity to do this is linked to the time parameter assigned to each track segment.

In the last chapter we study how to evaluate the speed of a particle that cross the muon system. To do this we need to optimize the time measurement and its resolution; the time parameters of the segments must also be referred to a physical time scale. We thus estimate the obtainable β resolution for cosmic and prompt muons. These studies are performed on cosmic real data and on MC simulated data. Finally a simulated data sample of HSCP is analyzed and the speed of the particles is estimated. We evaluate the resolution necessary to separate HSCP candidates from muons background.

Chapter 1

Physics at the LHC

The most update description of the constituents of matter and of their interaction laws is based on symmetry principles, conservation laws and spontaneous gauge symmetry breaking. The Standard Model successfully describes in a unified theory the Strong, Electromagnetic and Weak interaction in a electroweak spontaneous symmetry breaking scenario. We can write the Standard Model Lagrangian function in a very compact form as follows:

$$\mathscr{L} = -\frac{1}{4}F_{\mu\nu}F^{\mu\nu} + i\overline{\psi}\gamma^{\mu}D_{\mu}\psi + \psi^{T}\lambda\psi h + h.c. + |D_{\mu}h|^{2} + V(h) \qquad (1.1)$$

The experiments at LEP electron-positron collider at CERN verified the Standard Model prevision up to the second order of radiative correction in particular for the gauge sector physics of the Z and W that we can read from the 1.1 formula above. The Tevatron collider at Fermilab and other experiments tested the flavor physics and the related mesons oscillation with CP violation contained also in 1.1. The least understood part is the Higgs sector of SM and the related electroweak gauge spontaneous symmetry breaking (at the end of 1.1). All the direct searches of the Higgs boson have given negative results up to the available energy and the signal-background separation possibilities. The excluded Higgs mass regions due to the tests made at LEP and Tevatron are $m_{higgs} < 114.4$ GeV and a region of 10 GeV around 165 GeV [8]. The verification of the full Standard Model mechanism which includes the Higgs symmetry Breaking mechanism with the discovery of the Higgs boson is indeed one of the main goals of physics today and this is the major aim for which the Large Hadron Collider at CERN has been projected and built. The mass of the Higgs boson is not defined within the Standard Model theory (it is one of the theory parameters) and an hadron machine is the most suited to span new particles search in a unknown large range mass.

But there are also many reasons, both theoretical and experimental, to search beyond the SM physics. The former ones are *the hierarchy problem*,

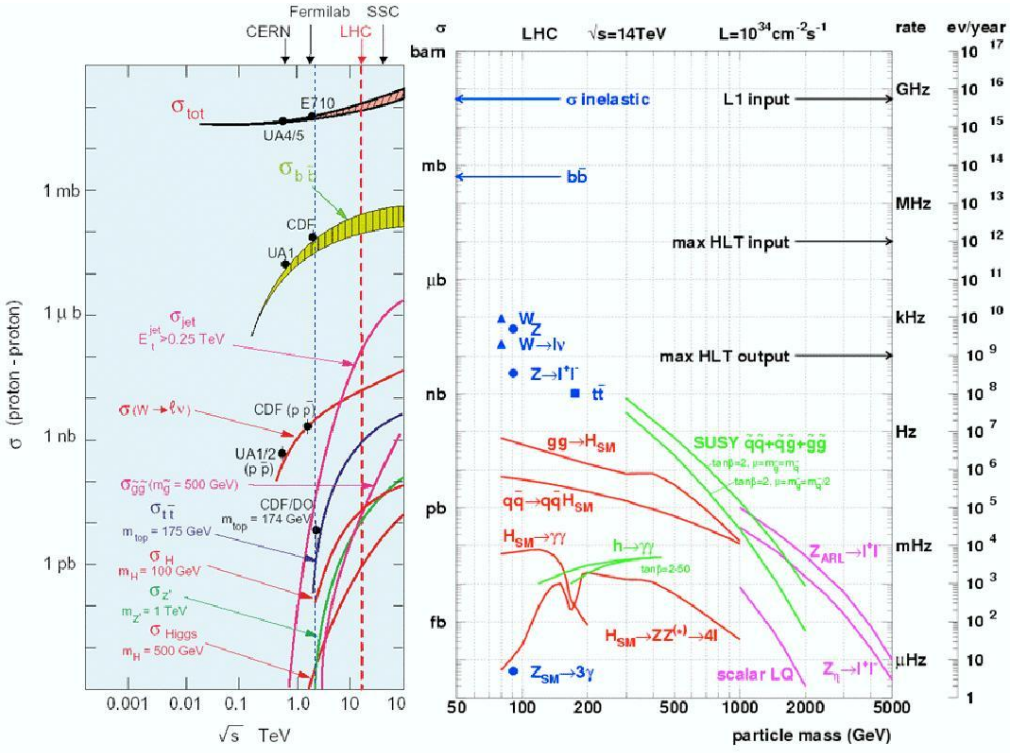

Figure 1.1: *Predicted ross sections and rates for the main physical processes at the LHC*

the Grand Unification and the *Flavor problems*, the latter are *the neutrinos masses and oscillations* and the cosmological problems of *Dark Matter* and *matter-antimatter asymmetry.* Innumerable theoretical models have been developed in the last decade to solve these problems and the very significant aim of the LHC collider is to confirm or to disavow experimentally these models. We cite for example the *Super Symmetry (SUSY)* that predicts a correspondence between bosons and fermions; for each SM particle is predicted a new particle with opposite statistic behavior. Since we never saw supersymmetric particles the SUSY must be broken in such a way that the supersymmetric partners of the SM particles have large masses (of the order of 100 GeV but not larger than TeV in order to permit the solution of the hierarchy problem). SUSY can also solve the Dark Matter problem with the introduction of a new discrete symmetry, the R-parity, that forbid the Lightest Supersymmetric Particle (LSP) to decay to a SM particle. In order to be a Dark Matter candidate the LSP should be massive ($\sim$ 100 GeV) and neutral. Many SUSY models predict good candidates such as neutralinos or gravitinos.

LHC with the foreseen center of mass energy (of 14 TeV) and luminosity

will explore the TeV range physics and will be able to detect the new particles predicted if they exist. In Fig. 1.1 we plot the predicted cross sections for the most relevant physical processes the scientist are interested in. We can clearly see the dependence of the cross section by the energy of the collisions. Cross sections like those of Higgs production and top production are, at the energy of the LHC, orders of magnitude greater than at the energy of Tevatron. We can also see in Fig. 1.1 the great amount of background processes with respect to the processes we are interested in. One of the most difficult challenges at the LHC has been to build an efficient system of trigger in order to discriminate the interesting events from the background.

Search for Heavy Stable Charged Particles at the LHC

As reported in the introduction we discuss in this thesis some aspect of the foreseen search of a very specific process signal of new physics ,"Heavy Stable Charged Particle" , which is part of the so called "EXOTICA Search", at the CMS experiment built for LHC machine. As we clarify more precisely later we checked carefully the realistic capability to detect such signals using one of the characteristic of the CMS detector; the results comes from the understanding of the real detector performance studied with cosmic rays and they will be compared with the ones used in simulation of the HSCP and others pp processes.

Let's here report briefly the Several theoretical models which predict the possible existence of new long-lived charged particles. These particles could be charged under $U(1)$ gauge group, i.e. electrically charged, and/or under $SU(3)$ color group. In the latter case hadronized states are expected to appear. In this thesis we will be interested in massive particles carrying only electric charge. HSCPs arise in models in which one or more new states exist and which carry a new conserved, or almost conserved, global quantum number. Supersymmetry with R-parity and extra dimensions with KK-parity provide examples of such models.

Quasi-stable sleptons are predicted in the framework of Gauge Mediated Supersymmetry Breaking (GMSB) supersymmetric models. These models try to explain how supersymmetry breaking happens in a theory that includes gravity. In these models the gravitino is very light and hence the lightest supersymmetric particle for any relevant choice of theory parameters. In GMSB the next-to-lightest supersymmetric particle (NLSP) dacays only via gravitational coupling and can be very long lived. In most of the non-excluded parameter space the stau is the NLSP and is quasi-stable. Production of the stau at the LHC can proceed via a virtual photon or Z or via production of heavier supersymmetric particles. Thus one or more stau can appear in the final state as slow muon-like particles.

Quasi-stable lepton-like particles are also predicted by the Universal Extra Dimensions model (UED). It predicts that for all SM particles there

exist corresponding so-called Kaluza-Klein (KK) states in extra dimensions, which have the same quantum numbers and spins as their SM partners but higher mass. All KK states conserve a KK symmetry, so that the lightest KK particle, usually the KK photon, is stable. In a certain region of the parameter space of the theory the KK lepton may become quasi-stable, with a lifetime larger than SM muon. The dominant mode for KK lepton production at LHC is direct pair production with a cross section of 20 fb for 300 GeV KK-τ.

HSCPs could be produced by the Large Hadron Collider (LHC) as a result of direct pair-production processes or as final products of the decay chain of heavier exotic particles. The typical signature of these particles is a muon-like behavior: they cross all the detection system of an experiment leaving ionization tracks. They have high transverse momentum but, because of their great mass, low velocities. From special relativity we know that $\beta = \frac{v}{c} = \frac{p}{\sqrt{p^2+m^2}}$, so,if the particle mass is not negligible, the β factor will assume values significantly minor than 1. At the LHC the HSCPs could give rise to missing energy signals since their mass is unknow. More features about the HSCP search will be presented in chapter 4.

1.1 The LHC

[1] The *Large Hadron Collider (LHC)*, build at *CERN*, is one of the greatest technological challenges ever attempted. With a length of 27 km, the collider, entirely made up of superconducting magnets, accelerates two bunched protons beams in opposite direction up to an energy of 7 TeV, reaching a luminosity of $10^{34} cm^{-2} s^{-1}$ and makes them collide in four points along its circumference.

Energy per proton	7 TeV
Dipole field	8.33 T
Design luminosity	$10^{34} cm^{-2} s^{-1}$
Bunch separation	25 ns
No. of buches	2808
No. of particles per bunch	$1.15 \cdot 10^{11}$

The very aim of LHC is to explore the TeV scale in order to give some answers to the innumerable theories that have been developed in the last decade. To explore a wide energy range an hadron collider is more appropriate than a electron collider. An hadron collider is in practice a quark/gluon collider, the real collisions indeed occur between quark and/or gluons of which the protons are made (partons). If $\sqrt{s}$ is the energy in the center of mass the real center of mass energy of each collisions is $\sqrt{x_1 x_2 s}$ where x_i is the fraction of momentum that each parton carries. So the collisions in

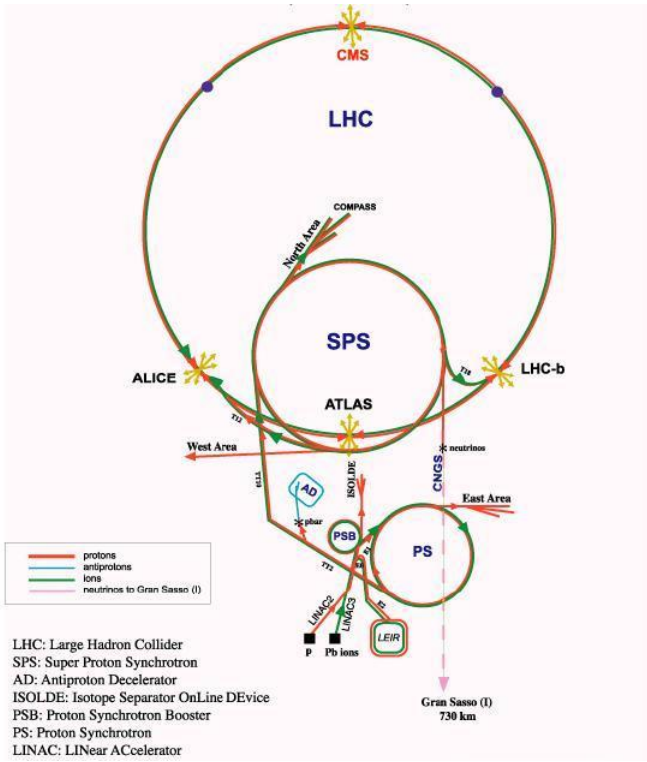

Figure 1.2: *The LHC, overall structure*

an hadron collider can range between zero and $\sqrt{s}$, thus the whole energy range available is explored.

Four experiments are build along the LHC circumference: *CMS (Compact Muon Solenoid)*, *ATLAS (A Toroidal LHC ApparatuS)*, *ALICE (A Large Ion Collider Experiment)*, *LHCb (LHC Beauty experiment)*. They have different aims.

CMS and ATLAS are very similar: they study all the final states of p-p collisions and their aim is to find the Higgs boson and all the New Physics of the TeV scale. ALICE is constructed to study the quark-gluon plasma from the collisions of lead ions. LHCb studies the CP violation in the b-quark physics.

Because of the incident of September 2008 the LHC in 2009 will start running with an energy of 5 TeV per proton and with a luminosity of $10^{32}\text{cm}^{-2}\text{s}^{-1}$.

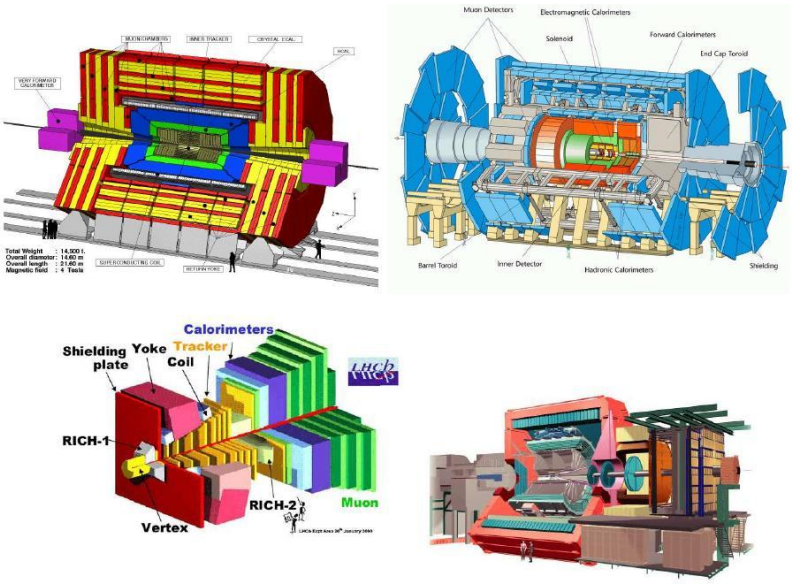

Figure 1.3: *The four experimets built at the LHC. From top-left: CMS, ATLAS, LHCb, ALICE*

Chapter 2

Compact Muon Solenoid & Drift Tubes

The *Compact Muon Solenoid (CMS)* experiment was specifically designed in order to search for the Higgs boson and every signal of New Physics from the protons collisions at the LHC. The name itself declares the main features of CMS: the biggest superconducting magnet of the world, creating a 4 Tesla solenoid field, is the core of a very compact detection structure designed with particular attention to the muon and electromagnetic systems.

For this thesis work we will be interested in particular in the performances of one class of the sub-detectors of the muon detection system, the Drift Tubes chambers of the barrel. In this chapter we will firstly describe the CMS detection and trigger structure. Then we will focus on the Drift Tubes chambers detectors describing both their local electronic trigger system and the procedure for track segments reconstruction: particular relevance will be reserved for the muon track construction algorithms.

2.1 Detector & sub-detectors overview

2.1.1 Physics and detector requirements

The CMS design is build around the main physical processes that will be studied thanks to the collected data. The main aim of CMS is to *search for the Higgs boson*: the favorite decay channels of the Higgs depend strongly by its mass. The natural width of the Higgs boson in the intermediate mass region ($[114, 182]$ GeV) is only a few of MeV: the observed width of a Higgs signal will be dominated by the instrumental mass resolution. In the mass interval $[114, 130]$ GeV the two-photons decay is one of the principal channels likely to yield a significant signal. The Higgs boson should be detectable via its decay into two Z bosons if its mass is larger than about 130 GeV (below the $2m_Z$ one of the Z is virtual). For $m_h \in [2m_Z, 600]$GeV the ZZ decay with

4 leptons in the final state is the best signal to be investigated. The hadronic decays of the Higgs could be very difficult to be studied because of the large QCD background of the LHC; hence the search is preferentially conducted using final states that contain isolated leptons and photons, despite the small branching ratios.

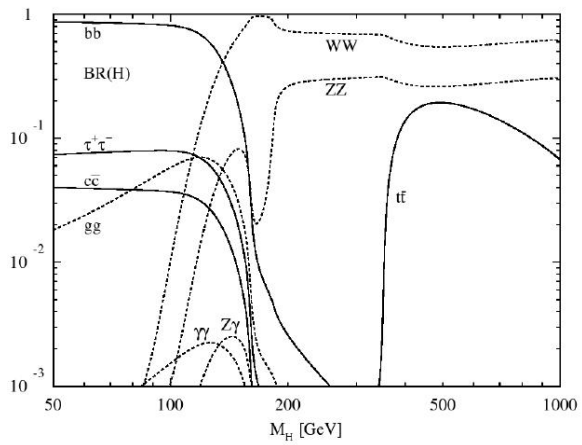

Figure 2.1: *Higgs bosons decay predicted branchin ratios as function of the Higgs mass*

The *search for Supersymmetric particles* is one of the goals of CMS. The decays of SUSY particles, such as squarks and gluinos, involve cascades that, if R-parity is conserved, always contain the Lightest SUSY particle (LSP). The latter is expected to interact very weakly, thus leading to significant Etmiss in the final state. The rest of the cascade results in a abundance of leptons and jets. In the GMSB the presence of hard isolated photons is expected.

Search for massive vector bosons as Z' lead to final states involving the presence of leptons from decays such as $Z' \rightarrow e^+e^-$ and $Z' \rightarrow \mu^+\mu^-$. Ways of distinguishing between different models involve the measurement of the natural width and the forward backward asymmetry, both of which require good momentum resolution at high pT ($\delta_{p_T}/p_T < 0.1$ at $p_T = 1$TeV).

The LHC will also allow *studies of QCD, electroweak and flavor physics.* Precision studies can give indications for physics beyond the Standard Model, providing complementary information with respect to the direct searches. Top quark will be produced at the LHC with a rate measured in Hz giving the opportunity to test the SM couplings and spin of the top quark.

The *detector requirements* to meet the goals of the LHC physics programme can be summarized as follows:

- Good muon identification and momentum resolution over a wide range

of momenta in the region $|\eta| < 2.5$; good di-muon mass resolution ($\sim$ 1% at 100 GeV); ability to determine unambiguously the charge of muons with $p < 1TeV$.

- Good charged particle momentum resolution and reconstruction efficiency in the inner tracker. Efficient triggering and offline tagging of τ and b-jets, requiring pixel detectors close to the interaction region.

- Good electromagnetic energy resolution, good di-photon and di-electron mass resolution ($\sim$ 1% at 100 GeV), wide geometric coverage ($|\eta| < 2.5$), measurement of the direction of photons; π^0 rejection and efficient photon and lepton isolation at high luminosities.

- Good E_t^{miss} and di-jet mass resolution, requiring hadron calorimeters with a large hermetic geometric coverage ($|\eta| < 5$).

The CMS design meet these requirements. The detector structure is described in the following sections. The main distinguishing features of CMS are a high-field solenoid, a full silicon-based inner tracking system, a fully active scintillating crystals-based electromagnetic calorimeter and a complete muon detection system.

2.1.2 CMS overall structure

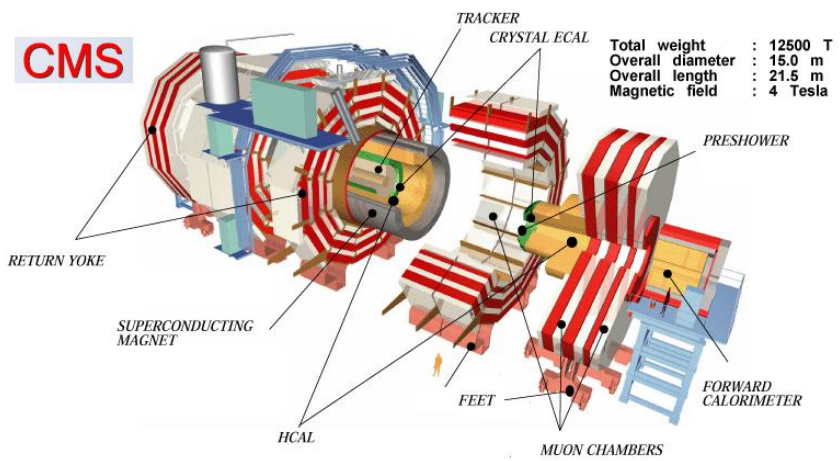

Figure 2.2: *The CMS overall structure*

CMS presents the cylindrical structure shown in Fig. 2.2 . In order to detect all the possible final states of the protons interactions the detector is almost hermetic. The overall dimensions of the CMS detector are a length of 21.5 m, a diameter of 14.6 m and a total weight of 12,500 tons. The

CMS structure is build around the superconducting solenoid 7 m long with a diameter of 6 m. The magnetic field in the inner region is 3.8 T while in the muon detectors region the field lines are collected in the iron return yokes and the field has approximately the value of 1.7 T . Strong magnetic fields are needed in order to ensure large bending power to measure precisely the momentum of charged particles ($\delta_{p_T}/p_T < 10\%$ at 1 TeV). Radially CMS is divided in different detection zones. The inner region (contained inside the magnet): coming from the interaction point we encounter firstly a tracking zone made of silicon detectors (tracker); then there are the electromagnetic and hadronic calorimeters for the detection and destruction of electrons and photons the former, of all hadrons the latter. Externally the magnet the muon detection system is built.

Tracker

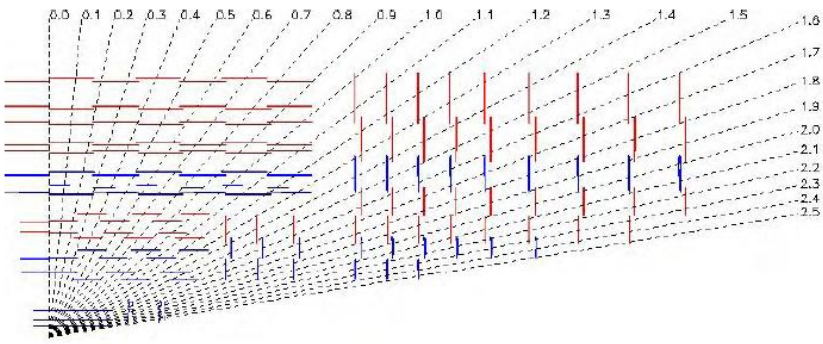

Figure 2.3: *The silicon Tracker structure*

The tracker [6] is the closest to interaction point detector of CMS. Entirely made of silicon semiconductors detectors is divided into three regions delineated by considering the charged particle flux at various radii at high luminosity. Closest to the interaction vertex where the particle flux is the highest ($10^7/s$ at $r \simeq 10$ cm), pixel detectors are placed; the size of a pixel is $100 \times 150 \mu m^2$. In the intermediate region ($20 < r < 55cm$) the particle flux is low enough to enable use of silicon microstrip detectors with a minimum cell size of $10cm \times 80\mu m$. The layout of the tracker is showed in Fig. 2.3. The outer radius extends to nearly 110 cm while the total length is approximately 540 cm.

The performance of the tracker is illustrated in Fig. 2.4, which shows the transverse momentum and impact parameter resolutions in the $r - \phi$ and z planes for a single muon with a p_T of 1, 10 and 100 GeV, as a function of pseudorapidity.

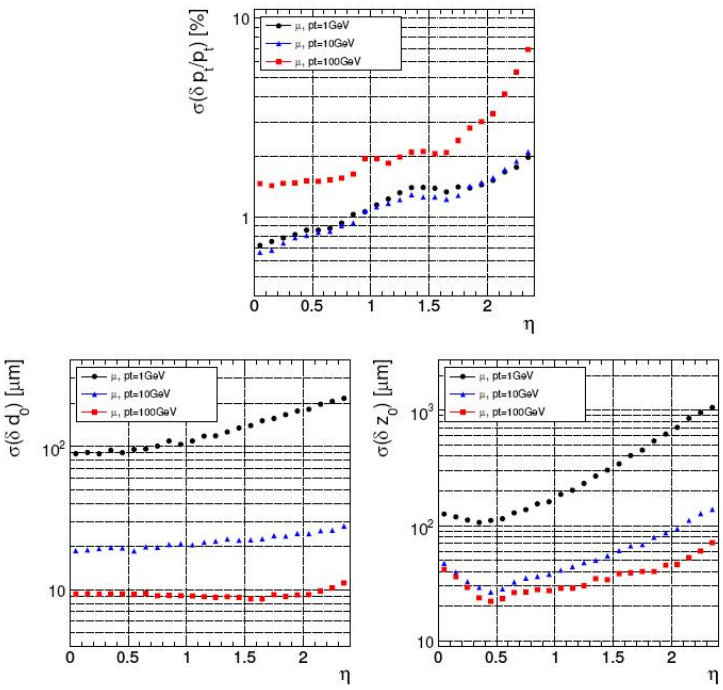

Figure 2.4: *Tracker resolution*

Electromagnetic calorimeter

The Electromagnetic Calorimeter (ECAL) [4] is a hermetic, homogeneous calorimeter comprising 61200 lead tungstate ($PbWO_4$) crystals mounted in the central barrel part, closed by 7324 crystals in each of the 2 end-caps.

CMS has chosen lead tungstate scintillating crystals for its ECAL. These crystals have short radiation ($X_0 = 0.89$ cm) and Moliere (2.2 cm) lengths, are fast (80% of the light is emitted within 25 ns) and radiation hard (up to 10 Mrad). However, the relatively low light yield (30 γ/MeV) requires use of photodetectors with intrinsic gain that can operate in a 4 T magnetic field. Silicon avalanche photodiodes (APDs) are used as photodetectors. The use of $PbWO_4$ crystals has thus allowed the design of a compact calorimeter inside the solenoid that is fast, has fine granularity, and is radiation resistant.

The performance of a supermodule was measured in a test beam. Representative results on the energy resolution as a function of beam energy are shown in Fig. 2.5 The energy resolution, measured by fitting a Gaussian function to the reconstructed energy distributions, has been parameterized as a function of energy:

$$\left(\frac{\sigma}{E}\right)^2 = \left(\frac{S}{\sqrt{E}}\right)^2 + \left(\frac{N}{E}\right)^2 + C^2$$

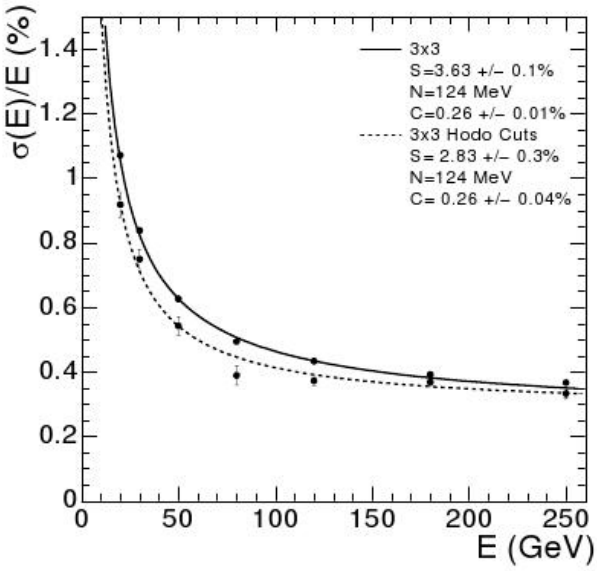

Figure 2.5: *Electromagnetic calorimeter resolution as function of energy*

where S is the stochastic term, N the noise and C the constant term.

Hadron calorimeter

The design of the hadron calorimeter (HCAL) [5] is strongly influenced by the choice of magnet parameters since most of the CMS calorimetry is located inside the magnet coil and surrounds the ECAL system. An important requirement of HCAL is to minimize the non-Gaussian tails in the energy resolution and to provide good containment and hermeticity for the E_T^{miss} measurement. Hence, the HCAL design maximizes material inside the magnet coil in terms of interaction lengths. Brass has been chosen as absorber material as it has a reasonably short interaction length, is easy to machine and is non-magnetic. Maximizing the amount of absorber before the magnet requires keeping to a minimum the amount of space devoted to the active medium. The tile/fiber technology has been the choice. It consists of plastic scintillator tiles read out with embedded wavelength-shifting fibers.

The hadronic calorimeter, between the three inner detectors, has been penalized in favor of the electromagnetic calorimeter and the tracker system. The absorber material has been maximized, at the expense of the active material, in order to contain the hadronic products of the collisions. In order to improve the energy resolution hadron forward (HF) calorimeters in the end-caps and a layer of scintillators outside the coil, the hadron outer (HO) have been added. For gauging the performance of the HCAL, it is

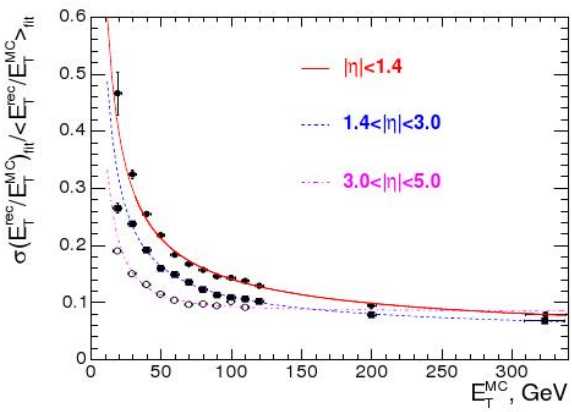

Figure 2.6: *Hadron calorimeter resolution as function of energy*

usual to look at the jet energy resolution and the missing transverse energy resolution. The granularity of the sampling in the 3 parts of the HCAL has been chosen such that the jet energy resolution, as a function of ET, is similar in all 3 parts. This is illustrated in Fig. 2.6 . The resolution of the missing transverse energy (E_T^{miss}) in QCD di-jetevents with pile-up is given by $\sigma(E_T^{miss}) \simeq 1.0 sqrt \Sigma E_T$ if energy clustering corrections are not made, while the average E_T^{miss} is given by $\langle E_T^{miss} \rangle \simeq 1.25\sqrt{\Sigma E_T}$.

Muon system

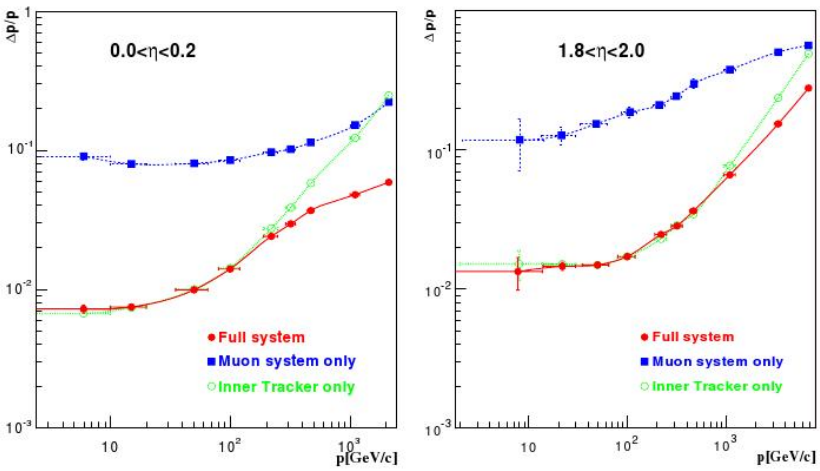

Figure 2.7: *Muon reconstruction resolution*

The required performance of the muon system is defined by the narrow states decaying into muons and by the unambiguous determination of the charge of muons at p = 1 TeV . Centrally produced muons are measured in the inner tracker and in the return flux. The detection system used outside the CMS magnet is called the Muon system [3]. It is divided in a middle region, the barrel, around the interaction point and composed by five wheels and two end-caps, divided in five disks each one. Measurement of the momentum of muons using only the muon system could be not sufficient to reach the desired resolution. In Fig. 2.7 we show the resolution δ_p/p as function of the momentum when different detectors are used for the momentum measure. At low momenta the momentum resolution is essentially dominated by the multiple scattering. At high momentum the best momentum resolution is obtained by combining the inner tracker and the muon detector measurements.

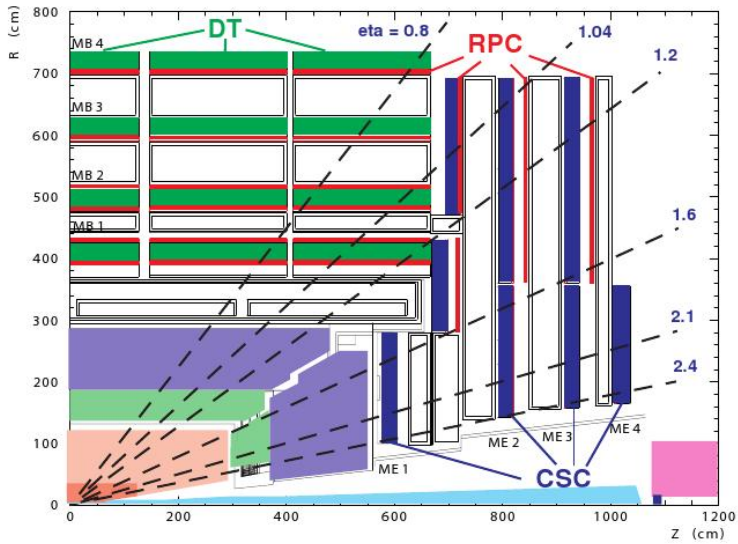

Figure 2.8: *Muon reconstruction resolution*

Three types of gaseous detectors are used in the muon system to identify and measure muons. The Drift Tubes (DT) in the barrel, the Cathode Strip Chambers (CSC) in the end-caps and the Resistive Plat Chambers (RPC) both in the barrel and in the end-caps. The DTs or CSCs and the RPCs operate within the first level trigger system, providing 2 independent and complementary sources of information. They measure the position and direction of the prticles exploiting the return flux of the solenoid magnetic field. They perform momentum measurement independently from the measurement performed in the central region of the CMS detector. In Fig. 2.8

we can see the structure of the muon system.

The barrel region is divided into 5 dodecahedral wheels, thus there are 12 sectors per wheel numbered from 1 to 12 by starting from the sector in the positive x direction. Four parallelepiped DT chambers are located in each sector together with a variable number of RPCs . The sandwich of DTs and RPCs are called Muon Barrel stations and are indicated with MBx. MB1, MB2, MB3 and MB4 from the inner to the outer one. In the sectors 4 and 10, i.e. the vertical ones, there are two MB4 stations; conventionally the seconds of these stations are assigned to "sectors" 13 and 14. The pseudorapidity range covered by DT is $|\eta| < 1.2$. The stations in the barrel (and the disks in the foreward) are separated by iron which collects the return magnetic flux. The iron has the double task of stopping particles debris of hadron shower escaping the hadron calorimeter and producing a non saturated (1.7 Tesla) field parallel to the beam line. It allow an almost field-less region for the DT chambers and yield the bending for transverse momentum measurement . Due to the calorimeter material in front of the first station muons coming from the interaction region reach the first station if generated with momentum greater then 4-5 GeV. Otherwise they reach the last DT station if they have a momentum higher than about 7 GeV. Drift Tubes chambers will be described in detail in section 2.2. They are the sub-detectors studied in this thesis work. The Muon Endcap system comprises 468 CSCs in the 2 endcaps. Each CSC is trapezoidal in shape and consists of 6 gas gaps, each gap having a plane of radial cathode strips and a plane of anode wires running almost perpendicularly to the strips. The signal on the wires is fast and is used in the Level-1 Trigger. However, it leads to a coarser position resolution.

CMS frame of reference

The CMS conventional 3D frame of reference has its origin in the nominal interaction point, the x-axis pointing radially inward toward the center of the LHC, the y-axis pointing vertically upward; the z-axis points along the beam direction toward the Jura mountain from the LHC point 5. The azimuthal angle ϕ is measured from the x-axis in the x-y plane (transverse plane). The polar angle θ is measured from the z-axis. Pseudorapidity is defined as $\eta = -\log\tan\theta$

The operations of CMS during data taking consist on the identification of the physical interesting events, described in Trigger section, on the storing of the information of all the detector parts of CMS performed by the data acquisition (DAQ), and on the reconstruction and analysis of the collected data performed in different stages: on-line at high level trigger (HLT), off-line at the different cluster farms foreseen for that Tier 0 at CERN, Tier1 and Tier2 spread in all the word around.

In the following sections we will describe the trigger of CMS and the reconstruction of muons.

2.1.3 CMS Trigger

Despite the high energies that we can reach at LHC, one of the main features of an hadronic collider is the enormous background of events. For the nominal LHC design luminosity of $10^{34} cm^{-2} s^{-1}$ we expect a rate of 109 interactions every second due to the protons bunch collisions that occurs every 25 ns .

We need to reduce this rate by a factor of at least 107 to 100 Hz , the maximum that can be archived by the on-line computer farm. A very efficient trigger system is necessary to select the most interesting events [9]. CMS has chosen to reduce this rate in two steps, thus there are two trigger levels. The first, named *Level 1 trigger (L1)* , is based on custom electronics while the second, the *High Level Trigger (HLT)*, relies upon commercial processors. The hardware L1 trigger reduces the event rate from 1 GHz to 100 kHz while the software HLT brings the rate to the final 100 Hz .

We focus on the electronic Level 1 trigger design.

Level 1 trigger

The trigger is the start of the physics event selection process. A primary decision to retain an event has to be made within 3.5 μs witha frequancy of 40 MHz (every 25 ns). This decision is based on the event's suitability for inclusion in one of the various data set to be used for analysis [10]. These data sets are designed to be significant for searches of top quark, higgs boson, supersymmetry and other of the main targets for which the LHC has been built. Typical are, for example, di-lepton or multi-lepton data sets or lepton plus jet data sets that are used for top and higgs searches.

The CMS L1 trigger is based on the identification of muons, electrons, photons, jets and missing transverse energy. Physics requirements on L1 are chosen to provide a high efficiency for the hard scattering physics to be studied at the LHC. This physics include signals such as top decays, higgs decays, W-W scattering, supersymmetry etc. The main physics requirement for a lepton or jet event in an acceptable pseudorapidity range is the presence of *high transverse momentum*. Trigger is also required in the presence of considerable quantity of *missing transverse energy*.

The trigger has to be inclusive and local. The local philosophy implies an initial selections of electrons, muons, photons and jets that relies on local information tied directly to their distinctive signatures, rather on global topologies. This is possible to do since the only global entities are neutrinos

(from a global sum of missing transverse energy). The time between beam crossing at the LHC is 25 ns, which is too short for the trigger system to provide a decision. The data are therefore stored in a pipeline and the first level trigger decision is transmitted to the detector electronics within 3.2 μs after the crossing.

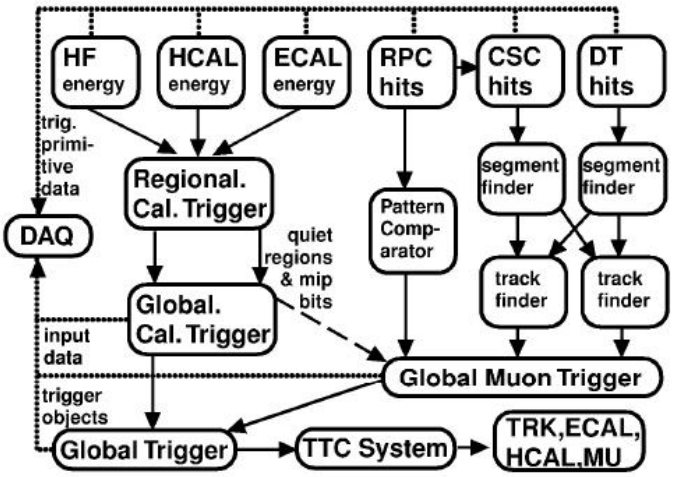

Figure 2.9: *Level-1 trigger scheme*

The L1 trigger involves the calorimetry and muon systems. In particular the L1 trigger system is organized into three mayor subsystem: the L1 calorimeter trigger, the L1 muon trigger and the L1 global trigger. The muon trigger is further organized into subsystem representing the 3 muon detector systems: the Drift Tube trigger in the barrel, the Cathode Strip Chamber trigger in the endcap and the Resistive Plate Chamber trigger covering both barrel and endcap. A scheme of the L1 trigger is reported in Fig. 2.9 .

The decision whether to trigger on a specific crossing or to reject that crossing is transmitted via the *Trigger Timing and Control (TTC)* system to all the detector subsystem frontend and readout systems.

In section 2.2.1 we describe in details the Drift Tubes local trigger.

2.2 The Drift Tubes chambers of the barrel

The CMS detectors we are interested in for this thesis work are the *Drift Tubes chambers (DT)* [13] [1] [3], gas detectors of the muon detection system located in the barrel region. Four DT chambers of variable size are located

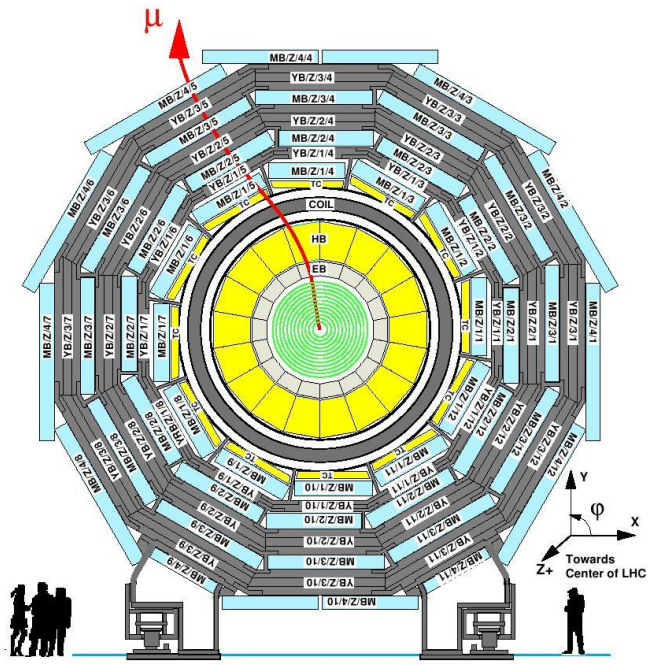

Figure 2.10: *Transverse view of CMS, the Drift Tubes disposition*

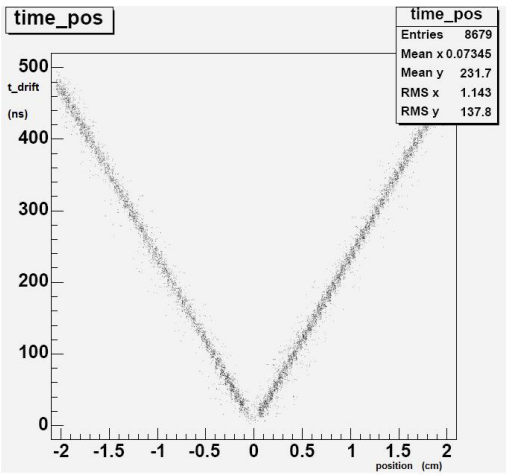

Figure 2.11: *Linearity t_{drift}-position. Verification of the constancy of the drift velocity.*

in each sector separated by iron (see Fig. 2.10). From now on we use the codes from MB1 to MB4 to the four DT chambers in each sector.

The DT are gas detectors formed by aluminum tubes (from 2 m to 4 m long) whose section is a cell rectangular 4.2×1.3 cm^2 arranged in 12 parallel

layers which are organized in groups of four (*Superlayers SL*). The expected rate in such a cell dimension (2.5 meter long) is below 10 Hz at the highest luminosity. There are two SLs with tubes parallel to the B field and the beam line for bending measurement in the transverse plane; the other SL is posed normally and see the tracks in the longitudinal plane. At the center of the cell runs for the entire length of the tube a steel wire (diameter 50 μm) which acts as the anode while the walls of the cells (called I-beams because of the shape of I) are the cathodes; electrodes (i.e. strips of aluminum placed with mylar) are placed parallel both above and below the wire for shaping the electric field inside the cell. As shown in Fig. 2.12 the structure of the cathodes was specifically designed so that, with suitable potentials (3600 V on wire, 1800 V on strips and -1200 V on the cathodes), only the electrons produced in a range of a few millimeters, normal to the plane of the wires, are influenced by an almost constant electric field that causes them to drift toward the anode.

The cells are filled with a gas mixture with 85% of Ar and 15% of CO_2 at atmospheric pressure. Such a gas mixture was selected for safety reasons and for the good performance even in presence of magnetic field. The electrons drift velocity (v_{drift}) is almost constant (54 μm/ns) as we can see in Fig. 2.11 . The constancy of the drift velocity is basic to identify in time the proton interaction that has generated the track (bunch crossing assignment) and the position and direction already at first level trigger. The chambers operate under proportionality regime with multiplication factor of the primary electrons of about 10^4, this means that when the primary electrons arrive in the proximity of the wire (at 300-400 μm), the intensity of the electric field causes a mechanism of avalanche ionization of the gas that produces a detectable signal on the wire-anode.

In every chamber the two external superlayers, superlayers SL_ϕ, 30 cm distant, measure the trajectory in the plane transverse to the beam. A third (SL_θ, absent in MB4) measures the position along the direction of the beam. An aluminum structure called "honeycomb" 128 mm wide is located between the SL_ϕ and SL_θ (between the two SL_ϕ in MB4) to give

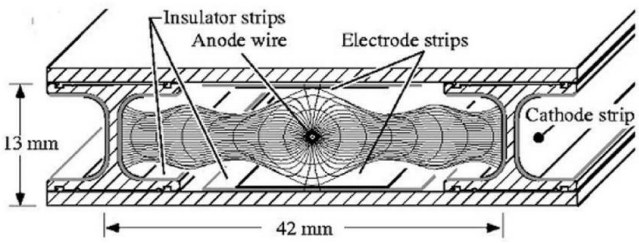

Figure 2.12: *Section of a drift tube, with the electrc field lines highlighted*

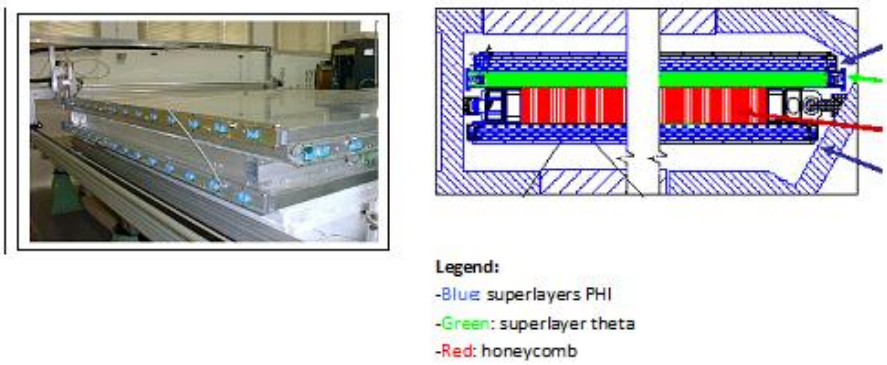

Figure 2.13: *Section of a Drift Tubes chamber. The superlayers and the honeycomb structure are visible.*

rigidity to the chamber and increase the lever arm of the two SL_ϕ (see Fig. 2.13).

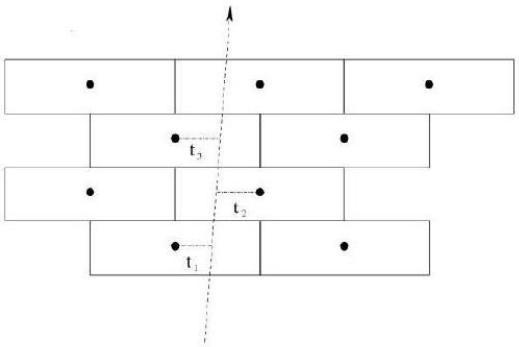

Figure 2.14: *Cells of a superlayer interested by the passage of a particle. The drift times are shown.*

A SL is shown in Fig. 2.14 to any drift time in a cell correspond two hits symmetric with respect to the wire position. Layers are staggered of half-cell. The staggering allows to solve the left-right position ambiguity.

The hits, and so the tracks, are reconstructed from the drift times (also shown in Fig. 2.14),recorded by Time to Digital Converter (TDC), by knowing the drift velocity ($\simeq 54\mu m/ns$). The wire drift times signals are used by the DT local trigger devices for primitive generation. They are recorded from TDC with an accuracy of 25/32 ns once the moment of interaction of protons (bx) is correctly identified. Both trigger devices and TDCs work and and are read out with clock frequency derived from the 40 MHz of the LHC

machine. 40 MHz frequency is of basic importance in CMS and constitutes the clock timing for of the entire system. The resolution of each cell is of the order of 200 μm and of 0.001 rad in direction .

The accuracy used at first level trigger is about a factor 6 larger but still sufficient to allow a p_T measurement as described later in the trigger description.

All the DT chambers design is constructed around the electronic trigger system. We will see it in details in the following sections. The segment reconstruction algorithm will we described next.

2.2.1 Drift Tubes Local Trigger

The muon trigger [11] provides the identification of the muon and its bunch crossing and a measure of the muon track curvature that enables a sharp cut on momentum for rate reduction. These tasks are separated in the Drift Tubes local trigger [12]. Trigger primitives are the segments reconstructed inside each chamber. *Drift Tube Track Finder (DTTF)*, a regional algorithm, links the chamber trigger segments and identify a track with its momentum and position information, at the frequancy of 40 MHz. The DTTF info are then used for the global muon trigger.

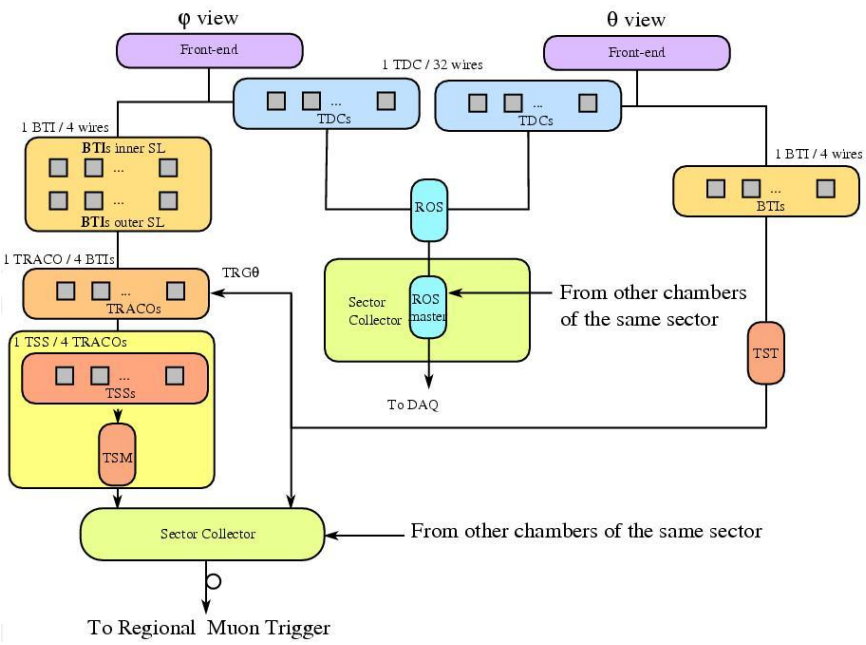

Figure 2.15: *DT level-1 trigger scheme*

A general scheme of DT local trigger is reported in Fig. 2.15. Each muon chamber is instrumented in the transverse plane (ϕ view) and in longitudinal

plane (theta view). The front-end trigger device is called *Bunch and Track Identifier (BTI)* . It performs a rough track reconstruction within each superlayer and uniquely assigns the parent bunch crossing of the candidate track. The BTI is followed by a *Track Correlator (TRACO)* that associates portions of a track in the same chamber combining groups of BTIs of the phi view among them. The TRACO enhances the angular resolution and produce a quality hierarchy of the triggers.

TRACO trigger data are transmitted to the chamber *Trigger Server (TS)* whose purpose is performing track selection in a multitrack environment. The $TS\phi$ selects two tracks (looking for the lowest bending angle) among all tracks transmitted by the TRACO.

Data from the four muon station of each CMS sector are conveyed towards a *Sector Collector (SC)* that codes the trigger informations (track position, bending angle, trigger quality) and sends them to *Regional Muon Trigger*.

Bunch and Track Identifier

The BTI is the first device of the DT local trigger [12]. It generates a trigger at the alignment of the hits produced in the group of drift tubes interested by the muon. The coincidence of these hits happens at fixed time after the muon traversed the array of drift tubes; this fact allows the bunch crossing identification. The BTI can also extract from the hits the direction and the position of the track segment. The BTI working principle is the generalized mean-timer method . It has been developed to work on groups of four layers. This method relies on the fact that that the particle path is a straight line and the wire position along the path are equidistant. Considering the drift times of any three adjacent planes of staggered tubes the following relation is always true:

$$T_{max} = \frac{t_1 + 2t_2 + t_3}{2}$$

T_{max} is the maximum time drift to the wire, it depends on the drift velocity (in the absence of magnetic field the drift velocity is 54 μm/s , thus the T_{max} is 390 μs).

This relation allows the identification of the parent bunch crossing of a track. Since the method works on a group of four layers the bunch crossing identification is possible even if the drift time of a tube is missing, due to inefficiency or to a presence of a delta ray. Each BTI is connected to nine wires (i.e. nine cells) as shown in Fig. 2.16 .

The evaluated parameters are the position, computed in the superlayer center, and the angular k-parameter $k = h \cdot \tan(\psi)$, being ψ the angle with respect to the normal to the chamber plane and h the distance of two layers, 13 mm. Parameters are evaluated every time for six couples pf planes; a BTI trigger is generated if at lest three of the six k-parameters evaluated are in

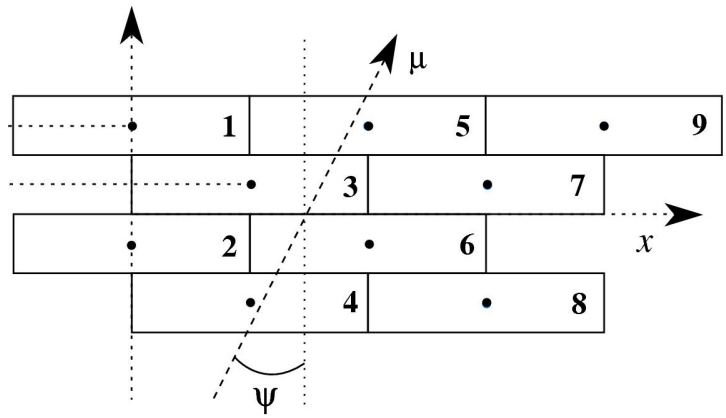

Figure 2.16: *Group of cells connected to a BTI. Relevant parameters for segment primitive reconstruction.*

coincidence. If there is a coincidence of all the six k-parameters the trigger corresponds to the alignment of four hits and it is marked as High Quality Trigger (HTGR), while in other case, it is due to the alignment of three hits and it is marked as Low Quality Trigger (LTGR). The angular resolution is track pattern dependent and is in general worse for LTGRs.

Track Correlator

The BTI is followed in the electronics chain by a Track Correlator that interconnects the two superlayers of the ϕ view [12]. Received the information from the BTI devices connected it finds the couple of BTI track segments that fits the best track. The reconstruction algorithm selects among all the candidates in the inner SL_ϕ and outer SL_ϕ the best track segment, according the preferences given to the trigger quality and to the track proximity to the radial direction (i.e. its p_T).

The parameters computed for the correlated tracks are:

$$K_{cor} = \frac{D}{2} \cdot \tan\psi = x_i - x_o$$

$$x_{cor} = \frac{x_i + x_o}{2}$$

The TRACO actions significantly improves the angular resolution, while the resolution of the position remains unchanged.

These parameters are converted to the chamber reference system. Position is transformed to the radial angle and k-parameter to bending angle as shown in Fig. 2.17 .

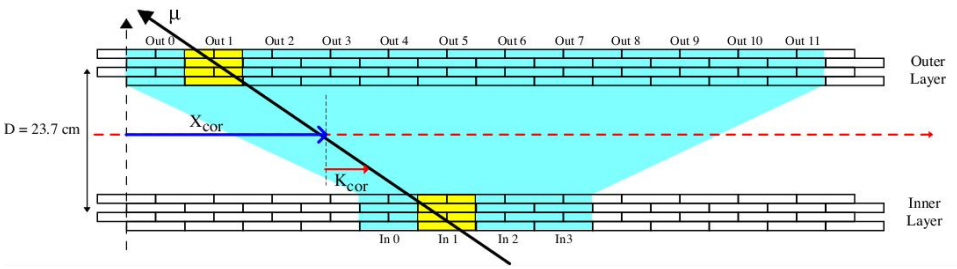

Figure 2.17: *The segment reconstruction on the two SL_ϕ. Relevant parameters are shown.*

Using the correlation between the BTI segments is also possible to improve the quality trigger information. This quality is coded with numbers from 0 to 6 as reported in the following table.

Description	Symbol	Code
HTGR in inner and outer SL	HH	6
One HTGR and one LTGR	HL	5
Two LTGRs	LL	4
HTGR on the outer SL	Ho	3
HTGR on the inner SL	Hi	2
LTGR on the outer SL	Lo	1
LTGR on the inner SL	Li	0
Null Track		7

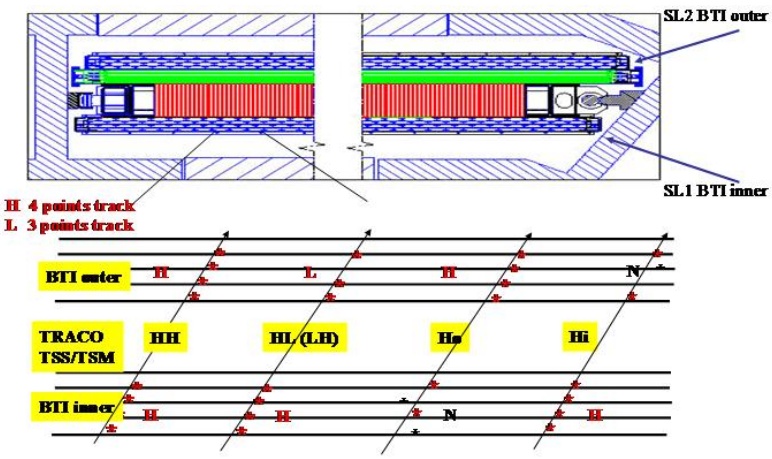

Figure 2.18: *The segment reconstruction on the two SL_ϕ. Quality flags.*

Trigger Server and Sector Collector

[12] *The Trigger Server* has to select the two best trigger candidates among the track segments selected by all TRACOs in a muon station and sends them to the Sector Collector, where they will be forwarded to the Regional Muon Trigger. The selection should be based on both the bending angle and the quality of the track segment; since only one TS is mounted on each station, it represents the bottleneck of the on-chambers trigger devices. The TS is composed by two subsystems: one for the transverse view (TS_ϕ) and one for the longitudinal view (TS_θ).

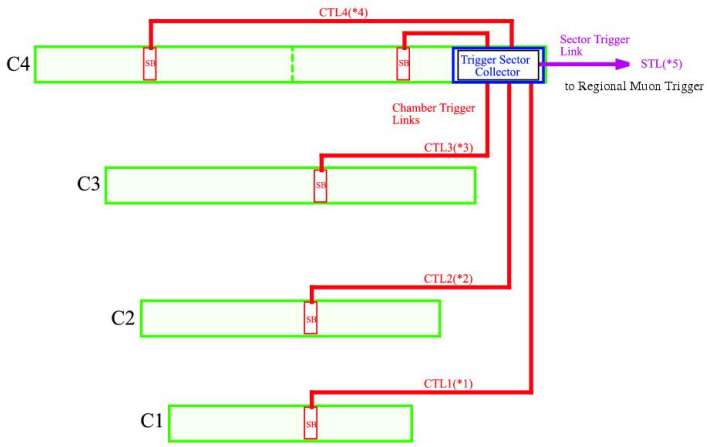

Figure 2.19: *The segment reconstruction on the two SL_ϕ. Quality flags.*

There is one *Sector Collector* for each sector (four station from MB1 to MB4). Trigger data from TS are grouped to form sector trigger packets and sent to the Regional Muon Trigger as shown in Fig. 2.19 .

In the following table we report a summary of standard data forwarded to Regional Muon Trigger from each muon chamber station.

	Quantity
Phi view	phi
	Phi bending
	Quality
	I/II track flag
	Overlap
Theta view	Position
	Quality

2.2.2 Muon track reconstruction

In this section we will see how the tracks of the particles are constructed in the CMS Drift Tubes system. We have seen that the trigger system performs a rough reconstruction of tracks and segments in order to be able to select the interesting events, typically events that have a large transverse momentum. After the trigger selection has been made the entire CMS detection system is allowed to register data. In the Drift Tube chambers the electronic chain registers serially all the times in the TDCs for a time of the order of $\sim 3\mu$s . When the decision to register the events has been taken, the times, temporally stored in the TDCs, are sent to the read-out [1] and the particles tracks must be reconstructed inside the whole detector.

We will see here how track segments and the whole particles tracks are reconstructed using the TDC times t_{TDC}. Muon reconstruction is performed in three stages:

- *Local reconstruction* (local-pattern recognition): starting from a seed (i.e. a group of hits compatible with the interaction vertex or with an initial direction and momentum) the chambers compatible with the seed are identified and local reconstruction is performed inside each DT chamber.

- *Standalone reconstruction*: successively the segments of different chambers are connected to form a track. This reconstruction uses only information from the muon system.

- *Global reconstruction*: the tracks are completed using also silicon tracker hits.

For our experimental work we will use only standalone tracks and their segments.

DT hit reconstruction: calibration of time pedestal and drift velocity

A *"time box"* is the distribution of all the recorded t_{TDC} for a group of cells, typically a superlayer. A time box example is reported in the 2.20. The peak at the beginning of the time distribution is due to the occurrence of δ-ray electrons which pass closer to the anode wire than the muon track while the tail is due "feed-back" electrons (extracted from the I-beams or from the aluminum strips).

[14]In each DT cell electrons produced at a time t_{ped} by the incoming particle migrate towards the anode with a velocity v_{drift} and reach the anode

[1] A L1A signal can be generated only at 40 MHz frequency and causes the TDC to send the drift times stored in a predefined window centered around the L1A signal time.

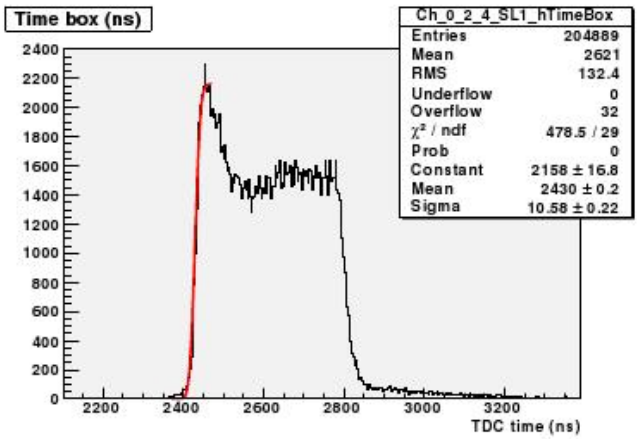

Figure 2.20: *"Time box": t_{TDC} distribution in a superlayer of a chamber. The rising edge is fitted with the "error function".*

at a time,in the recorded data of TDC, t_{TDC} . The distance of the track with respect to the anode wire is therefore given by

$$x = \int_{t_{ped}}^{t_{TDC}} v_{drift}\, dt \tag{2.1}$$

Two reconstruction algorithms are available in the CMS software to convert the measured time into a hit position. The first reconstruction algorithm assumes a constant drift velocity and a constant time pedestal within a group of cells (typically a superlayer); we can reconstruct the distances from the wires using the formula:

$$x_{ij} = (t_{TDC,ij} - t_{ped,j}) \cdot v_{drift,j} = t_{drift,ij} \cdot v_{drift,j} \tag{2.2}$$

where i is the measurement index while j is the superlayer index.

A good calibration of time pedestal t_{PED} and v_{drift} has to be done. The second reconstruction algorithm is based on a parameterization of the cell response obtained with GARFIELD [15]. This parameterization includes the dependence on the track impact angle, α, and on the stray magnetic ?eld B. We will use in our analysis hits reconstructed using the first algorithm, so we will describe here the t_{PED} and v_{drift} calibration procedure.

The recorded time in the TDC, t_{TDC}, includes other contributes in addition to the electrons drift time in the cell:

- the time of flight (TOF) of the particle from the interaction point to the cell;
- the time of signal propagation along the anode wire;

- delays due to cable length and to the electronic system;

These offset must be estimated and subtracted to the TDC time to estimate the real drift time.

First, it is necessary to correct the measured TDC times for the relative difference in the signal path length to the readout electronics of each wire. This relative difference is measured for each wire by sending simultaneous (within an error smaller than 150 ps) "test-pulses" to the front-end electronic.

Pratically we estimate the t_{PED} as the common offset, called t_{trig}, of the recorded t_{TDC} distributed in the time box of a group of cells together (a superlayer). The t_{trig} estimation method is based on a fit (also shown in 2.20) of the rising edge of the time box with the integral of the gaussian function (error function):

$$f(t) = \frac{1}{2} I \left[1 + \mathrm{erf}\left(\frac{t - \langle t \rangle}{\sigma\sqrt{2}} \right) \right]$$

The inflexion point of the rising edge of the time box, t , does not directly represent the time pedestal of the distribution, but can be related to it by defining:

$$t_{trig} = t - k \cdot \sigma, \tag{2.3}$$

where k is a factor that is tuned requiring the minimization of the residuals on the reconstructed hit position, superlayer by superlayer, with respect to a line fitting the track in the plane projection. A typical value of the k-factor is 1.3 .

Due to the limited available data, the t_{trig} is usually computed by a group of cells, one superlayer. In this case the measured t_{trig} includes the average TOF and the average signal time of propagation along the anode wires. If the chamber is uniformly illuminated, which is the case for pp collisions, this average TOF is approximately equivalent to that of a muon crossing the superlayer center, while the average signal propagation time is equivalent to the propagation time for a signal produced in the middle of the wire.

The v_{drift} is also computed for each superlayer. The calibration procedure of the drift velocity consists of an estimation of a weighted average value of the T_{max} (using the mean time algorithm) for many track pattern an a successively derivation of the v_{drift} using the formula:

$$v_{drift} = \frac{L/2}{\langle T_{max} \rangle}$$

DT segments reconstruction algorithms

For our analysis we will use segments data reconstructed using the **3-parameters fit** algorithm [16] [18]. It is a spatial fit among the hits of one or two superlayers (one in θ view, two in ϕ view) that computes, besides the position and the inclination of the segment inside the chamber, *the time of each segment* (t_0) with respect to the assumed pedestal coming from the calibration procedure. The algorithm constructs the segment from the hits leaving the time of passage of the particle in the chamber as a free fit parameter, together with the position and the inclination of the segment. The method requires only an approximated value of time pedestal to be used as input parameter for time to position conversion. Obviously we need at least four hits to evaluate three parameters in a fit. The segment are reconstructed for both the ϕ view and θ view, thus we have two values of t_0. The ϕ view fit is more reliable because of the presence of more hits.

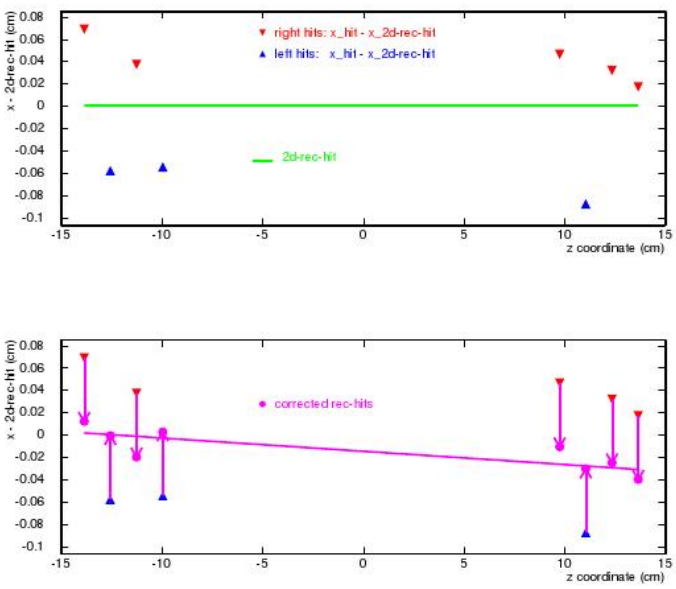

Figure 2.21: *Effect on the segment reconstruction of the t_0 correction: the common shift of the hits.*

This algorithm is particularly useful for *cosmic muons*. They hit the revelation system out-of-time with respect to the machine clock unlike the muons coming from the pp interaction that always reach the muon revelation system at discrete steps of 25 ns . If we built the segments fitting the hits without t_0 as free parameter we would have reconstructed segments with an absolute offset with respect to the hits. Leaving t_0 as a free parameter we

make the algorithm in conditions to correct this offset by minimizing the χ^2 of the fit even with respect to t_0 . In Fig. 2.21 is shown the effect of this correction on the segment reconstruction.

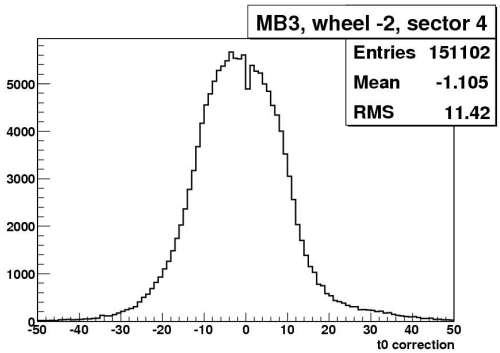

Figure 2.22: *A typical cosmic t_0 distribution in a DT chamber.*

We show in 2.22 a typical (for cosmic data) distribution of t_0 for a CMS DT chamber. We see that the t_0 correction can arrive up to 50 ns over the t_{trig}, that is the time-zero of Fig. 2.22.

The fit is independently performed in the $r-\phi$ and $r-z$ superlayers of a chamber to deliver the so called 2-dimensional (2D) track segment, the 2D segments are paired using all the possible combinations in the chamber, to form the collections of "4D" segments carrying complete spatial information.

DT segments reconstruction resolution

Several studies have been done on the DT chambers performances including hit resolution and position, direction and time of the tracks in each chamber. The results of test beam data analysis lead to an angle resolution of 0.001 rad and a single hit resolution of $\simeq 200\mu$m [19].

In a period of 1 month of cosmic data taking several millions of cosmic muons have been collected with a magnetic field of 3.8 T inside the solenoid. The results we present here *are relative to the cosmic data* collected in the autumn 2008 [20]. These data are called "Cosmic Run At Four Tesla" (CRAFT).

The distribution of the residual of reconstructed hits in the $r-\phi$ SLs with respect to the position in the layer plane predicted from the extrapolation of the reconstructed track segments is shown in 2.23 for the four stations of Sector 4 in the central wheel of the barrel detector. In all the chambers the ihit residuals distribution has a σ of the order of 300 μm when segment are reconstructed using the 3-parameters fit.

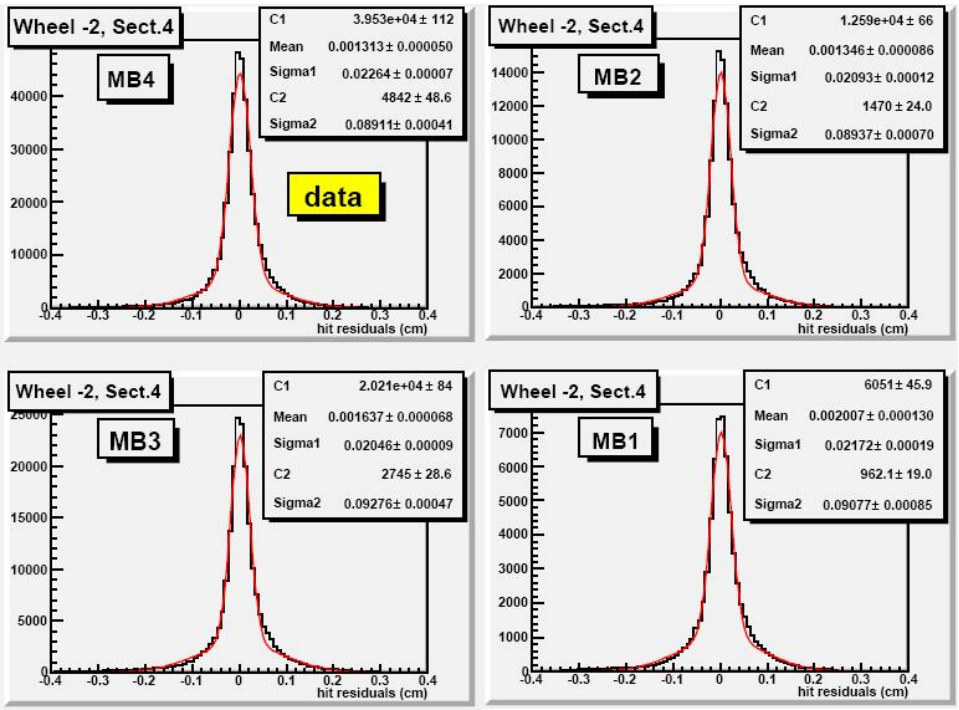

Figure 2.23: *Residual distribution for the Sector 4 of wheel 0.*

Stand Alone muon track reconstruction

The *standalone muon reconstruction* [7] uses only data from the muon detectors, the silicon tracker is not used. Both tracking detectors (DT and CSC) and RPCs participate in the reconstruction.

The reconstruction of muons from pp interaction point starts with the track segments from the muon chambers obtained by the local reconstruction. The state vectors (track position, momentum, and direction) associated with the segments found in the innermost chambers are used to seed the muon trajectories, working from inside out, using a specifically built algorthm (the Kalman-filter technique [21]). The predicted state vector at the next measurement surface is compared with existing measurements and updated accordingly. A suitable χ^2 cut is applied in order to reject bad hits, mostly due to showering, delta rays and pair production. In case no matching hits (or segments) are found, e.g. due to detector inefficiencies, geometrical cracks, or hard showering, the search is continued in the next station. The state is propagated from one station to the next using the GEANE package [22], which takes into account the muon energy loss in the material, the effect of multiple scattering, and the non-uniform magnetic field in the muon system. The track parameters and the corresponding er-

rors are updated at each step. The procedure is iterated until the outermost measurement surface of the muon system is reached. A backward filter is then applied, working from outside in, and the track parameters are defined at the innermost muon station. Finally, the track is extrapolated to the nominal interaction point (defined by the beam-spot size: $\sigma_{xy} = 15\mu m$ and $\sigma_z = 5.3cm$) and a vertex-constrained fit to the track parameters is performed.

When cosmic data are analyzed there are some differences between the pp muons that must be taken into account. Cosmic muons come prevalently from the top of the CMS detector with random direction and arrival times. *Cosmic muons standalone track reconstruction* presents little variations. The hits used as seed for the track reconstruction are preferably taken in the external zone of the barrel rather than in the inner parts of CMS. The initial trajectory direction is no more limited by the request for the particle to come from the CMS interaction vertex. For cosmic muons that penetrate the whole detector leaving two tracks both in the top and in the bottom regions of CMS the track reconstruction is done independently in the two zones, like the two tracks was due to two different particles (2-leg standalone reconstruction). Only in a second moment the two legs can be linked in order to form a unique track.

Chapter 3

DT trigger fine synchronization with Cosmic-rays

A major problem to be solved for a trigger of a detector on the LHC environment is the synchronization with the machine clock. The synchronization is required in order to reconstruct the same event in different parts of the CMS detector. In general the synchronization of a detection system consists in a appropriate setting of the electronic devices that control the detector response to physical events. In this chapter we will focus on the synchronization of the level 1 local trigger chain of the Drift Tubes chambers of the barrel that consists of setting, in every chamber, the appropriate action of an electronic device called TTCrx fine delay. Several studies on the trigger synchronization have been made since 2004 [23] using the test beam data.

Now we want to show how it is possible to perform the DT trigger fine synchronization using cosmic data collected up to 2008. We will show that the trigger fine synchronization procedure is directly correlated to the study of High Quality trigger efficiency as function of time of the track in all chambers. We will show that such efficiency has the same dependence in all chambers with the same hardware characteristics. Finally we will explain how to use these information to perform quickly the trigger fine synchronization at the LHC start-up moment.

3.1 Synchronization of the Drift Tubes Local Trigger

[12]The tool available for Drift Tubes chambers trigger chain synchronization is the Trigger and Timing Control system (TTC) which provides the machine clock distribution to the different stations and broadcasts the gen-

eral level-1 trigger strobe called L1A (Level-1 Accept). The TTC provides also a 32-bits word carrying the bunch crossing number; in such a way any local trigger signal can be associated to a unique bunch crossing number. The synchronization procedure assumes that inside the chambers the electronic modules are timed-in. This means that signal distribution within each muon station is done in such a way that the TTC signals are received simultaneously by each trigger board. The time equalization is achieved with electrical connections between the components of the trigger chain using cables of different length. The maximum skew of the clock distribution within the trigger boards of a chamber was recently measured around 1 ns. Hence in the following description each muon station will be considered one intrinsically synchronous block, equipped with one Trigger Timing and Control Receiver (TTCrx).

Trigger board electronics samples the signals coming from the wires and processes them in order to provide trigger signals. The front-end trigger device is the Bunch and Track Identifier (BTI) which assigns any candidate trigger to a bunch crossing number distributed by the TTC system. Its result depends on the values of two relevant quantities: the drift velocity v_d and the time pedestal t_{PED} corresponding to the time of a signal generated by a muon passing exactly on the anode wire. The drift velocity is in fact input to the BTI as a configuration parameter, while there are no means of setting a t_{PED} value, since the device does not actually uses the drift times as measured by the TDC, but it continuously monitors the input connection of each wire in order to detect a signal and to sample it using the time after detection in its calculations. The sampling frequency is 80 MHz and therefore signals are latched every 12.5 ns, value which corresponds to the actual time precision used in the algorithm. The time of signal sampling de-facto implies a t_{PED} value inclusion in the BTI equations in a non-trivial way and so a wrong sampling of the signal can cause a large error in the BTI calculations. The BTI sampling time can be changed by setting a fine delay (104 ps step) provided inside the TTCrx device. Changing the sampling time of the signals is equivalent to a modification of the t_{PED} used in the track fit and therefore it is evident that the trigger efficiency and the bunch crossing assignment capability of the algorithm must depend on the actual value assigned to this delay.

A wrong assignment of the v_d parameter or t_{PED} (equivalent to a modification of the BTI sampling time) causes efficiency losses and wrong parent bunch crossing assignment of a triggering muon. Therefore the best timing relation between the sampling clock and the machine clock (i.e. the best TTCrx delay setting) must be determined, in order to have correct time measurement and correct parent interaction identification.

There are two main sources of phase difference between the LHC clock and the DT trigger sampling clock: the muon time of flight and the delays due to signal and clock distribution to the DT stations. In table we rerport

the muons time of flight from the interaction point to the chambers located at different position in the CMS detector.

TOF from IP(ns)	MB1	MB2	MB3	MB4
$W \pm 2$	27.3 ± 1.2	29.3 ± 1.5	31.9 ± 1.8	34.6 ± 2.0
$W \pm 1$	21.6 ± 2.3	24.1 ± 2.6	27.3 ± 2.9	30.5 ± 3.1
$W0$	19 ± 4.3	21.9 ± 4.4	25.4 ± 4.4	28.8 ± 4.4

The DT trigger synchronization must be done in several steps:

- *Fine synchronization*: determination of the TTCrx fine delay optimizing the trigger bunch crossing identification efficiency in every chamber.
- *Coarse synchronization*: alignment (using coarse 25 ns delays) of the output trigger bunch crossing numbers in order to assure the simultaneity of the triggers originated from the same muon in different chambers at any level of the trigger chain.
- *Absolute synchronization*: definition of the absolute time with respect to the Bunch Crossing zero signal, i.e. synchronization with all the other detectors. This procedure is done by central trigger system.

In our analysis we will focus on the DT trigger fine synchronization, thus here we will describe it in more details.

3.1.1 Trigger fine synchronization

As described before, the BTI yield a low quality trigger (LTRG) or a high quality trigger (HTRG) if it finds, respectively, three or four aligned hits in the same bx alignments. Successively the TRACO enhances the quality flag of a trigger using the correlation of the two segments of the ϕ superlayers of each station. We have already described the effect of wrong synchronization on the BTI bx assignment; also the fraction of LTGRs increases in case of a wrong synchronization, since the BTI cannot anymore find precise alignment among hits. Another effect of a wrong synchronization is a reduction of the correlated triggers (HH, HL, LL, defined in section 2.2.1) since the track parameters will be wrongly measured.

To perform the trigger fine synchronization (i.e. to find the best configuration of the TTCrx fine delays) considering the trigger efficiency we require the presence of a very high quality correlated trigger (HH or HL). These studies have been made and are reported in [23]. Figure 3.1 shows the effects on bunch crossing assignment of wrong settings of the sampling clock timing using such a configuration. The histograms show the progressive

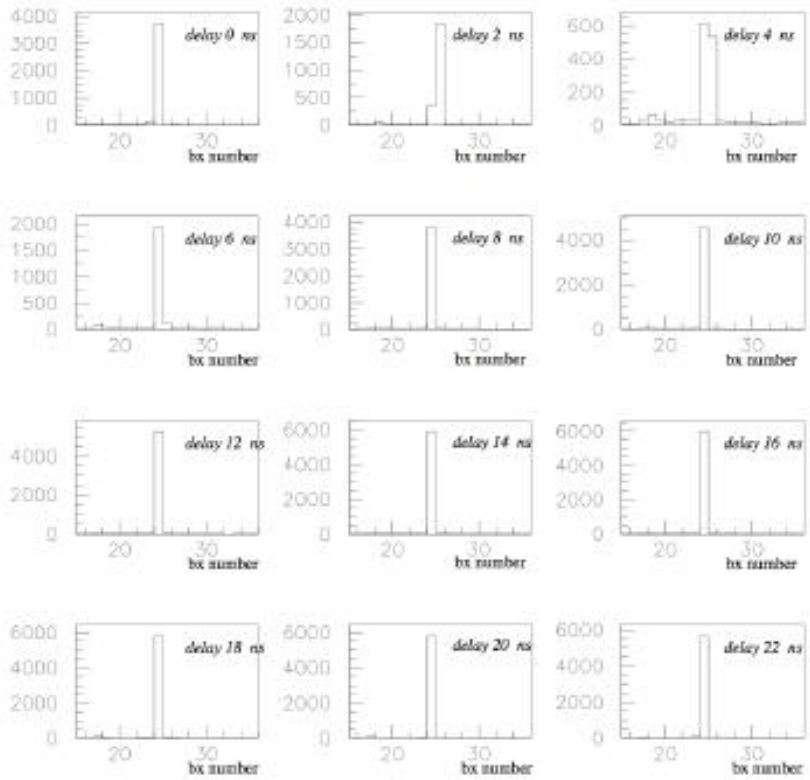

Figure 3.1: *Effects of variable delay settings on the bx assignment performed by the BTIs during the segment primitive construction.*

degradation of bunch crossing assignment quality since the bunch crossing is wrongly assigned for a fraction of events which depends on the actual delay set. The best delay is clearly set when there is no ambiguity in bunch crossing assignment.

Using the same data plotted in Fig. 3.1 we see in Fig. 3.2 that the fraction of HH triggers is smaller in correspondence of the delays where the bunch crossing assignment is worst. While the HH fraction decreases the HL fraction is instead growing partially compensating the efficiency drop. This kind of behavior fully meets our predictions. We also observe that there is a rather flat region of TTCrx delay values (about 8 ns wide) where the fraction of HH triggers is almost constant. Each station must be synchronized setting the TTCrx fine delay that maximizes the trigger efficiency with a precision defined by the width of the flat region.

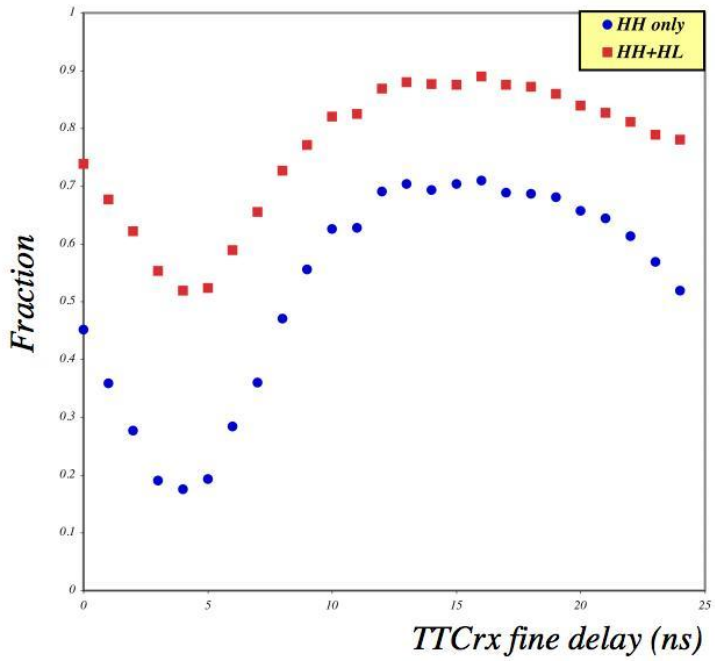

Figure 3.2: *Fraction of HH triggers as function of the TTCrx fine delay.*

3.1.2 Algorithms for fine synchronization

Algorithms have been developed on the bunched beam (40 MHz) data collected at CERN SPS in 2003 and 2004. They are based on trigger data or on TDC data collected during a scan of the TTCrx fine delays over a 1bx time window [23].

Trigger data are: the trigger quality, the impact position and the bending angle of the muon. The only quantity that can be used for fine synchronization is the quality. The best indicator is the ratio of HL trigger type to HH trigger type.This ratio should have a maximum at the worst phase and a minimum at the best phase. The measured plot is shown in Fig. 3.3. We see a well defined maximum that identifies the position at the worst phase value. A displacement backward or forward by 12.5 ns provides the best phase value.

The TDC data are the measured TDC time (t_{TDC}) that are the sum of the true drift times (t_d) and the time pedestals (t_{PED}). For every trigger the TDC data are assigned to a bunch crossing by the arrival of the L1A signal which defines the allowed time window for the data readout. Hence the TDC data will carry the offset introduced by the actual time slot assignment. If the sampling clock is correctly synchronized almost all the events will have the same bunch crossing assignment, while in the case of maximum de-

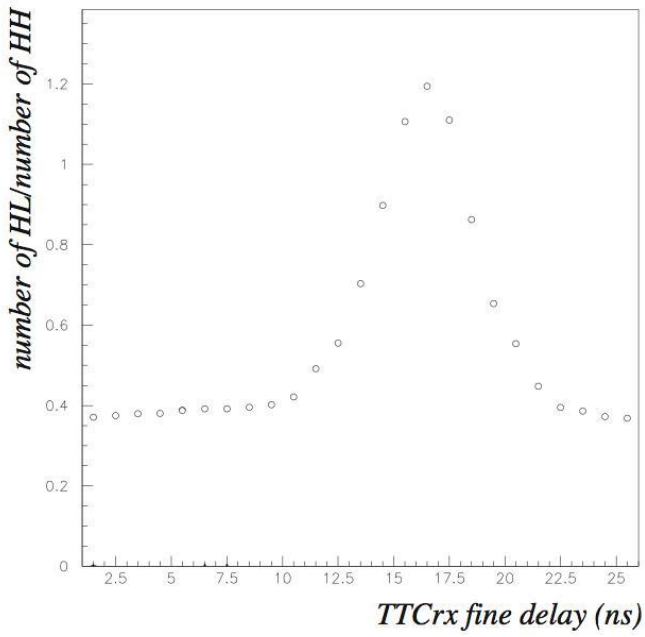

Figure 3.3: *Ratio $\frac{HL}{HH}$ as function of TTCrx fine delay.*

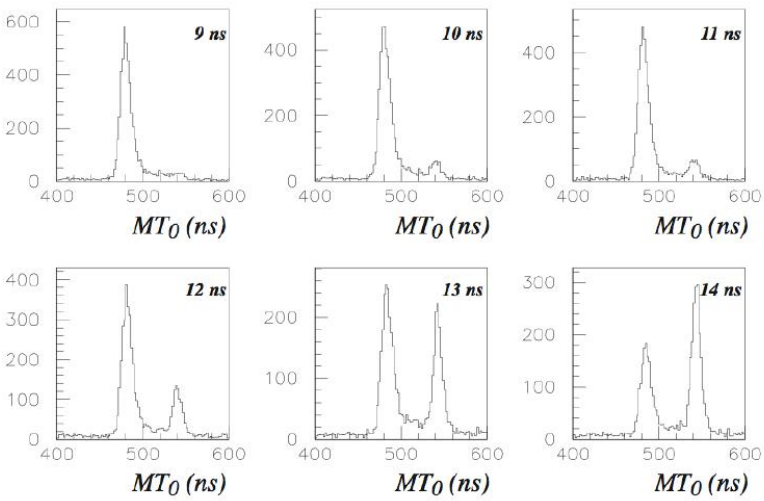

Figure 3.4: *MT0 distribution for different delay settings.*

synchronization the events will be equally shared between two consecutive bunch crossings.This effect is evident using the measured times ($T = t + t_{PED}$

) of any three consecutive layers to compute the quantity.

$$MT_0 = \frac{T_1 + 2T_2 + T_3)}{2} = \frac{(t_1 + 2t_2 + t_3)}{2} + 2t_{PED}$$

The variable MT_0 depends on the trigger latency, and indirectly, on the sampling clock phase: if the sampling clock is out of phase, the trigger output is distributed over two neighboring cycles and as a consequence t_{PED} jumps by 25 ns and the distribution shows two distinct peaks separated by 50 ns (Fig. 3.4).

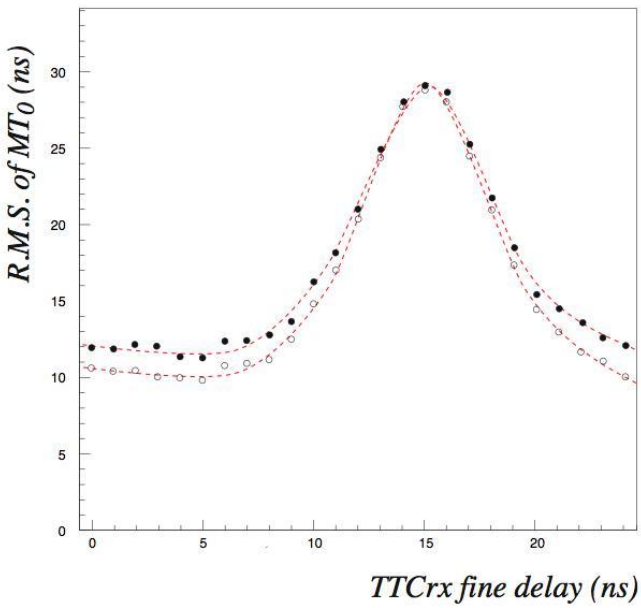

Figure 3.5: *rms of MT0 distributions as function of the TTCrx fine delay.*

The best phase sensitive quantity is the r.m.s. of the MT_0 distribution. The delay associated with the smallest r.m.s. will be the best one. We can pose quality constraints on the MT_0 distribution (in order to cut background and δ-ray effects) by using the information from the two superlayer of a each chamber (for example requiring $|MT_{01} - MT_{02}| < 3\sigma$ and $|MT_{01} - MT_{02}| < 1\sigma$). The r.m.s. distribution for two cuts is shown in 3.5 . The result is quite stable even using a relatively small number of events (as small as 1000 events for each TTCrx delay value).

We have then identified at least two ways to perform fine synchronization. Both the algorithms easily identify the worst phase, being instead flat at the right phase consistently with the fact that the best phase can be set with some good safety margin. In order to be validated they must give the same delay value obtained by the maximum efficiency search. The methods

have been compared for the same setup and the same chamber. The peak position of both quantities is compatible with the worst efficiency and the difference between best and worst phase is 12.5 ns as expected as effect of the 40 MHz clock frequency.

In the following sections we will develop an algorithm for trigger fine synchronization based on cosmic rays data.

3.2 DT Local Trigger Fine Synchronization using cosmic rays

Since 2005 a large amount of cosmic-rays data has been collected. Cosmic tracks have a flat time distribution that, when referred to the trigger, which has a 25 ns granularity, turns out to have a 25 ns flat wide distribution. Performing the trigger fine synchronization means to optimize the DT local trigger performances for a bunched beam by setting the appropriate values of TTCrx fine delay in each DT station. All the methods for fine synchronization we described in the previously section and that are described in [23] use bunch beam data collected with different TTCrx fine delay settings. They consider how some relevant quantities, used as fine synchronization indicators (such as $r.m.s.MT_0$ and $\frac{HL}{HH}$), change for different delay settings and determine what is the best delays setting. We can change our point of view and, instead of using synchronous particle with variable delay setting, we use not-synchronous particles with fixed delay setting.

Using cosmic rays and their time flatness we will be able to perform the local trigger fine synchronization if we are able to compute the cosmic muons time of passage in each chamber t_μ with respect to the time pedestal t_{PED} and if we are able to link this time with the TTCrx fine delay. The time pedestal t_{PED} is different for each DT chamber and represents the time of passage of a synchronous particle inside that chamber. Using the algorithm 3-parameter fit described in 2.2.2 we can compute track time $t_0 \stackrel{def.}{=} t_\mu - t_{PED}$, so a cosmic muon with t0=0 would have the same time, with respect to the local clock, of a muon generated by an interaction.

3.2.1 t_0 and the TTCrx fine delay

In order to perform the DT trigger fine synchronization using the t_0 of the cosmic events we cross-check the relationship between t_0 distribution of the tracks of a chamber and the TTCrx fine delay applied to that chamber. In 2007 several data "runs" have been collected to perform this analysis [24].

In the data collection, the chamber MB3 of a specific sector was requested to yield the L1A command when a local Trigger HH or HL was registered.

This means that have been acquired preferably events where the cosmic muon was "in phase" with the trigger of MB3. The TTCrx fine delay of the MB1, MB2 and MB4 has been moved in several sessions of measurements (13 "runs") at step of 2 ns from -12 ns to +12 ns leaving fixed the MB3 delay. Moving the TTCrx fine delay means to change the entire electronic system of a chamber, the trigger system and the TDC data acquisition. So, we expect that a diffent delay setting leads to a diffent reconstruction in-time of the segments.

The table below shows the "runs" features . The "run number", the number of MB3 triggers and the delays applied to MB1, MB2 ed MB4 with respect to MB3 are indicated.

RUN	MB1, MB2, MB4 delay
RUN 1860 Events: 49688	-12 ns
RUN 1861 Events: 33904	-10 ns
RUN 1862 Events: 49672	-8 ns
RUN 1863 Events: 47643	-6 ns
RUN 1864 Events: 49735	-4 ns
RUN 1866 Events: 49779	-2 ns
RUN 1858 Events: 30523	0 ns
RUN 1867 Events: 704	2 ns
RUN 1868 Events: 49778	4 ns
RUN 1871 Events: 49777	6 ns
RUN 1872 Events: 49748	8 ns
RUN 1873 Events: 45772	10 ns
RUN 1874 Events: 49789	12 ns

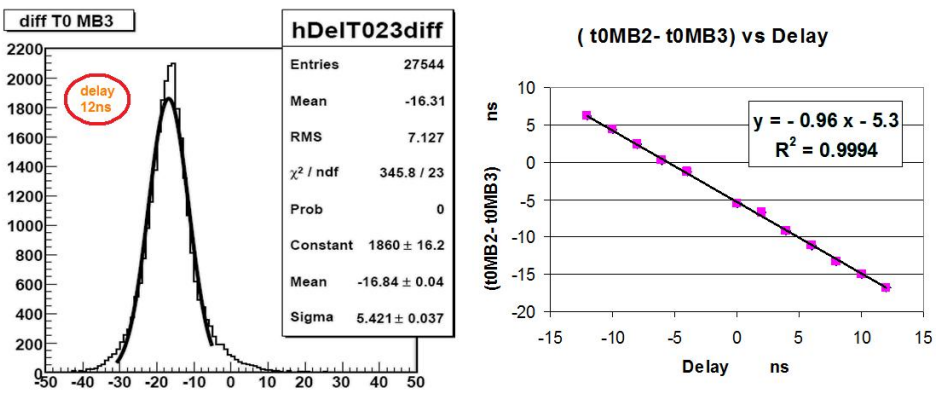

Figure 3.6: $\langle t_{0\ MB2} - t_{0\ MB3} \rangle$ *as function of the delay difference between the two stations.*

To see the linearity between t_0 and delay an analysis has been developed. The tracks that extend on superlayers ϕ are reconstructed with an associated t_0. For each value of TTCrx fine delay and for each chamber histograms showing the distributions of the difference between time t_0 in the MBx chamber and t_0 in the MB3 chamber ($t_0^{MBx} - t_0^{MB3}$, when the reconstructed muon track extend both on MB3 and MBx) have been constructed. Every distribution has been fitted with a gaussian function to obtain $\langle t_0^{MBx} - t_0^{MB3} \rangle$. In Fig. 3.6, as example, average values $\langle t_0^{MB2} - t_0^{MB3} \rangle$ are plotted as a function of the various delays of the 13 runs. Linearity and the relation 1:1 are clear. In the following table we report the fit results for all the chambers: the slopes of the fitting straight lines are almost equal to -1, confirming the linearity 1:1.

DT station	**Fit slope**
MB1	0.98 ± 0.12
MB2	0.96 ± 0.15
MB4	0.99 ± 0.10

3.3 Experimental setup

All our analysis have been done on the CMS run 68021 data [25]. The run consists of several millions of cosmic events collected with the magnetic field turned-on.

RUN 68021	
Events	20,000,000
Trigger	2 DT station bx coincidence, HLT was not filtering events
Magnetic field	3.8 T
Tracker	present
Data stream	"Monitor"

The run contains data relative to the whole CMS detection system but we will use only the Drift Tubes chambers information. For each DT chamber we have at our disposal trigger data and TDC data.

Off-line, the segment reconstruction has been done with 3-parameters fit (see section 2.2.2). Cosmic muons "standalone tracks" (section 2.2.2) have been also reconstructed. Segment, trigger and standalone data provide the information on the DT station that contains the segment or the trigger: it is thus possible to link triggers, segments and standalone tracks information event per event in order to use and to collect their peculiar features.

The triggers information are stored in a C++ class inside the CMS analysis frame CMSSW [26]. The class is *DTLocalTriggerCollection*. The relevant info contained in this class are:

- DT chamber of the trigger inside CMS (wheel, sector, chamber type)
- bx of the trigger
- quality of the trigger

The segments information are stored in the class *DTRecSegment4DCollection*. The relevant info contained in this class are:

- DT chamber of the segment inside CMS (wheel, sector, chamber type)
- number of the hits both in phi and in theta view
- 3D position of the segment inside the chamber
- inclination of the segment both in ϕ and in θ view
- $t_{0\phi}$ and $t_{0\theta}$ of the segment
- particle 3D momentum
- χ^2 parameter of the segment

The standalone track information are stored in the class *TrackCollection*. The relevant info we contained in this class are:

- DT chamber of every segment of the standalone track inside CMS (wheel, sector, chamber type)
- inclination of the track
- impact point of the track
- inner and outer position of the track
- particle momentum at the impact point, in the inner and outer points of the track
- number of the hits composing the track

We stored all the interesting data in a ROOT Tree [27].

The ROOT Tree contains many "entries". An entry is the ensemble of the data registered by the CMS detection system when the decision of to register the event has been taken. We have chosen to use only the DT chambers information and thus in the Tree we have stored only their data. The information registered in an entry belong to a wide time interval around the time of the event. For the Drift Tubes chambers, in each event, TDC

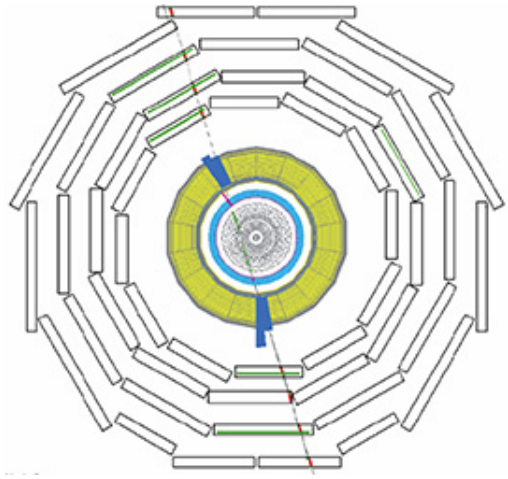

Figure 3.7: *A cosmic event at CMS.*

data are registered for a $\sim 3\mu$s wide time interval while Trigger data for a $\sim 1\mu$s wide time interval [1]. In each entry one muon event or more could be present. In Fig. 3.7 we show, as example, a typical CMS cosmic event.

3.4 HH Trigger efficiency plots with cosmic rays - CMS DT chambers trigger fine synchronization

Each reconstructed segment is associated to a t_0[2] that represents the time of passage of a cosmic muon with respect to the calibrated time pedestal t_{trig} (see 2.2.2). As told before we can link each trigger to the segment that has originated it. Thus, for each segment associated to a trigger, we can infer the time offset with respect to the t_{trig} of all the signals in a superlayer interested by the passage of a particle that lead to the trigger. As shown before the trigger response to a particle with an associated t_0 in a chamber with a TTCrx delay $= d_0$ is equivalent to the trigger response to a particle in-time with the machine clock (i.e. a particle with $t_0 = 0$) in a chamber with a TTCrx delay $= d_0 - t_0$. As shown in section 3.1.1 Fig. 3.2 the HH trigger efficiency is an indicator for the fine synchronization. We want to plot here the HH trigger efficiency as function of t_0; this is equivalent to plot

[1] The track segments and the triggers are relative, in each event, to hundreds of bx around the bx 12-13 (see section 2.2.2).

[2] In our analysis we will use the $t_{0\phi}$, more reliable than the $t_{0\ \theta}$ since it is computed on two-superlayers hits; from now on we refer to the $t_{0\ \phi}$ of each segment simply calling it t_0 .

the HH trigger efficiency as function of TTCrx fine delay (that is a method for the fine synchronization as explained in section 3.1.1).

The following analysis is performed on every CMS DT chamber:

- We build the histogram h containing the t_0s of all the segments assiciated with a trigger
- We build the histogram h^{HH} containing the t_0s of the segments assiciated with a High quality trigger (HH)
- We consider, as indicator for fine synchronization, the ratio of the two histograms that we call *HH relative trigger efficiency* and we define as $\mathrm{Eff}_{rel}^{HH} = \frac{h^{HH}}{h}$. We thus obtain automatically the HH trigger efficiency as function of time $\mathrm{Eff}_{rel}^{HH}(t_0)$

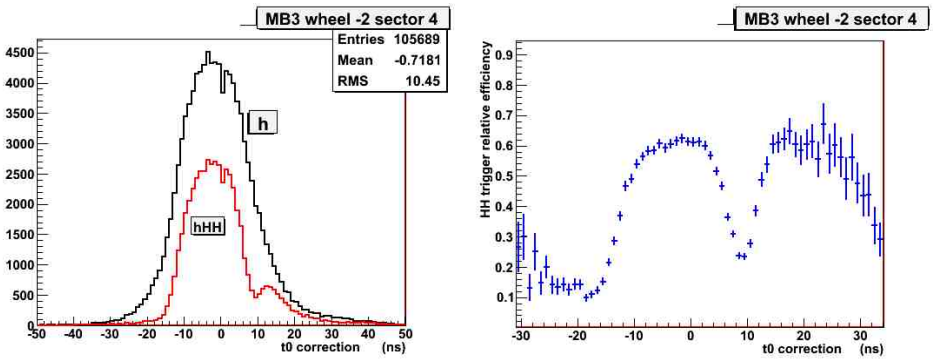

Figure 3.8: Left*: histograms h^{HH} (red) and h (black).* Right*: $Eff_{rel}^{HH} = \frac{h^{HH}}{h}$*

In Fig. 3.8 (left) we report, for the MB3 chamber of sector 4 of wheel YB-2, histograms that show the times t_0 for segments that have caused triggers of different quality: we have in black the times of all triggers, in red the times of HH quality triggers. We can use these histograms to evaluate the HH relative trigger efficiency [3] that, as told before, is an indicator for fine synchronization. The ratio of the histograms gives the Eff_{rel}^{HH} as function of time. We show in Fig. 3.8 (right) the HH relative trigger efficiency as function of time.

The Fig. 3.8 has an evident periodic shape in the $\simeq$ 25ns-wide regions around $t_0 = 0$ ns and $t_0 = 25$ ns; this is because this function represents the $\mathrm{Eff}_{rel}^{HH}(t)$ relative to two close bunch crossing. The part of the curve

[3]We call here the efficiency "relative" because is referred to the number of triggers. We may define also other efficiencies referred, for example, to the total number of the segments. In the following arguments we will use the HH relative trigger efficiency Eff_{HH}^{rel} defined above.

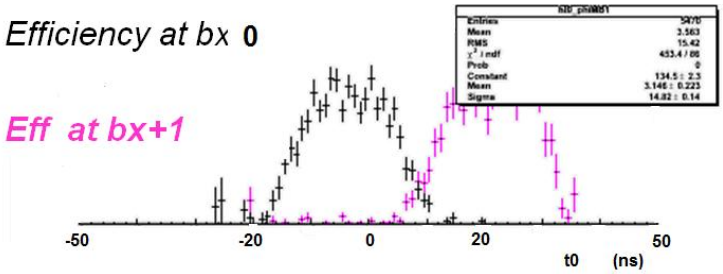

Figure 3.9: bx *separation in the efficiency plot*

around $t_0 = 0$ ns is relative to the segments associated at "bx= 0" (i.e. the most probable bx of a recorded events, see 3.3) while the part of the curve around $t_0 = 25$ ns is relative to the (few) segments associated at "bx= +1". In the efficiency plots like 3.8 we can separate these two contributes using the trigger information of bx number. The result is shown in Fig. 3.9. This is another prove that trigger efficiency has a periodic behavior in the 25ns-wide interval of each bunch crossing.

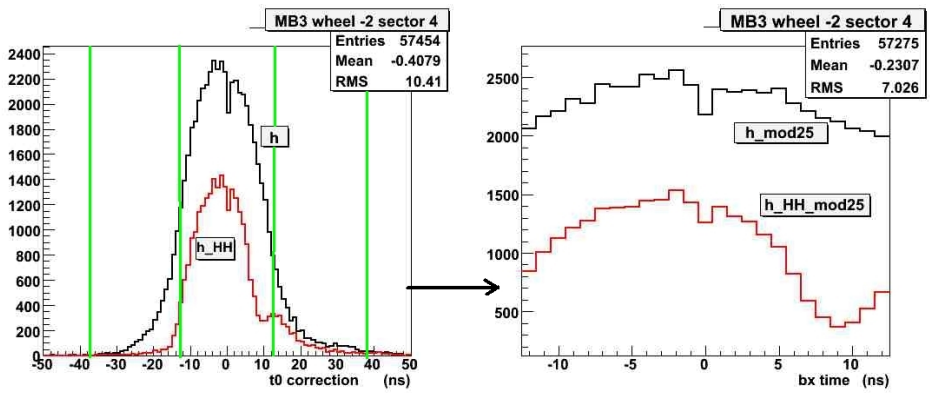

Figure 3.10: t_0 *trigger distribution in the 25ns wide time interval.*

In the light of this we can consider the sum of the close 25 ns wide intervals of the previously histograms h and h^{HH} as shown in Fig. 3.10. The new histograms show the distributions in time of the triggers and of the HH triggers in the 25 ns wide time interval of a bunch crossing. Their ratio (Fig. 3.11) is the HH relative trigger efficiency as function of time in the bx 25ns wide time interval. We note that the efficiency shape is the same of Fig. 3.2, with the typical drop of minimum efficiency and the almost constant efficiency region.

We call any plot like that of Fig. 3.11 *"efficiency plot"*.

We can improve our analysis for fine synchronization as follows (the following analysis is performed on every CMS DT chamber):

- We build the h histogram containing the t_0s of all the segments assiciated with a trigger
- We build the h^{HH} histogram containing the t_0 of the segments assiciated with a High quality trigger (HH)
- We sum the entries of both these histograms relative to the various 25 ns wide intervals (like shown in 3.10) obtaining the triggers distributions in time h_{mod25} and h^{HH}_{mod25} in a bx time interval
- We consider, as indicator for fine synchronization, the ratio of the two histograms h_{mod25} and h^{HH}_{mod25} that we call *HH relative trigger efficiency* and we define as $\mathrm{Eff}^{HH}_{rel\ mod25} = \frac{h^{HH}_{mod25}}{h_{mod25}}$. We thus obtain automatically the HH trigger efficiency as function of time $\mathrm{Eff}^{HH}_{rel\ mod25}(t_0)$
- We fit the efficiency plot using a polynomial of high grade (eighth grade) as shown in 3.11. We thus have $\mathrm{Eff}^{HH}_{rel\ mod25}(t_0)$ defined for every $t_0 \in [-12.5, 12.5]ns$
- In order to perform the fine synchronization, for each chamber, using the fit, we can evaluate the time of minimum efficiency

$$t_{0min} \in [-12.5, 12.5]ns \mid \mathrm{Eff}^{HH}_{rel\ mod25}(t_{0\ min}) = \min_{t_0} \left\{\mathrm{Eff}^{HH}_{rel\ mod25}(t_0)\right\}$$

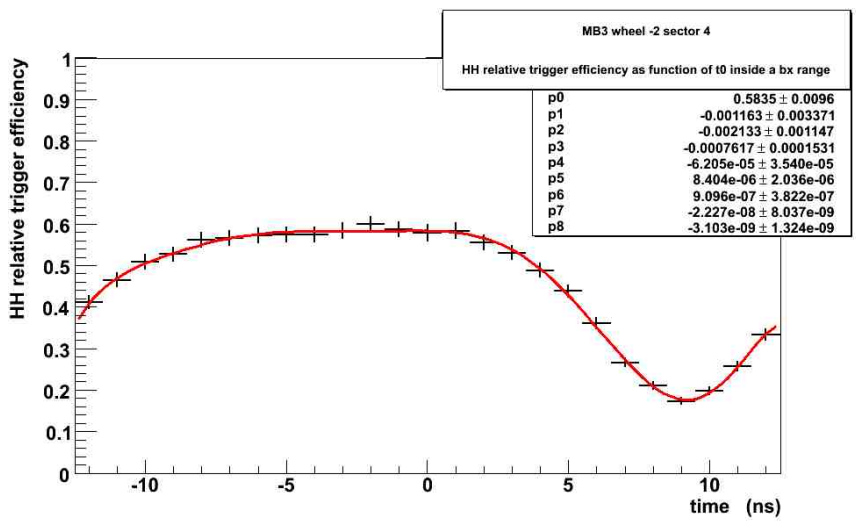

Figure 3.11: *Efficiency plot for MB3 station of sector 4 of wheel -2*

As example, for the efficiency function of 3.11 relative to chamber MB3 of sector 4 of wheel -2 we have the time of minimum efficiency:

$$t_{0\ min} = 9.3 \pm 0.3ns$$

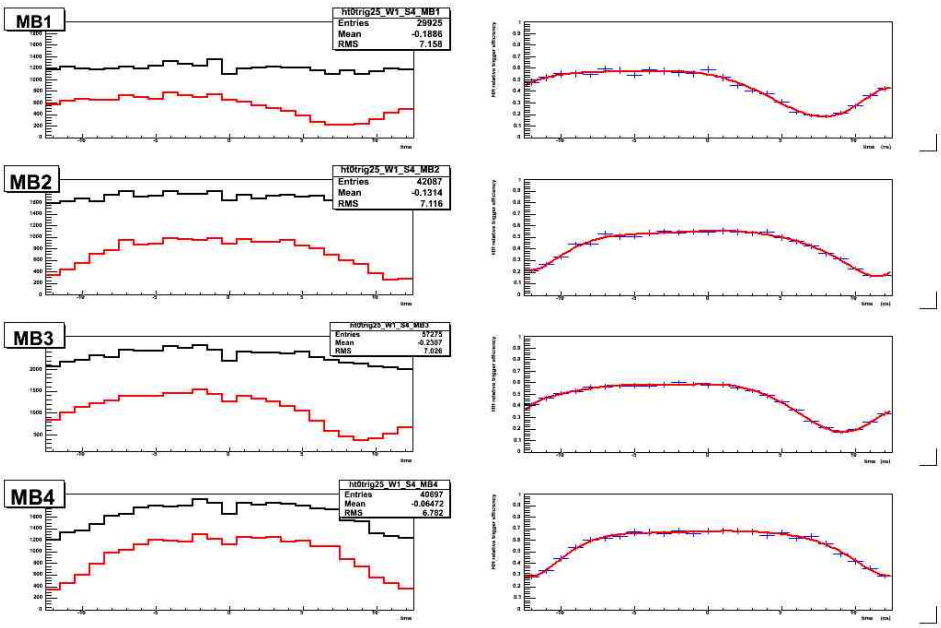

Figure 3.12: *Efficiency plots for the whole sector 4 of wheel -2*

We show in 3.12 the fitted HH trigger efficiency plots for the whole sector 4 of wheel -2 (chambers MB1 MB2 MB3 MB4).

All the $\mathrm{Eff}^{HH}_{rel\ mod25}(t_0)$ are actually relative to t_{trig} times, i.e. to the times extrapolated with a calibration (done with millions of events in every chamber). In the next session we will show how to refer the HH trigger efficiency to an absolute time reference.

3.4.1 HH trigger efficiency with respect to the chamber clock

The TTC system provides the machine clock distribution to all CMS DT chambers. Thus each DT chamber is equipped with a "clock". The clock is a square signal with period 25 ns (to be precise 24,951 ns). We want to use the clock of each chamber as absolute time reference. Up to now we have the $\mathrm{Eff}^{HH}_{rel\ mod25}(t_0)$, where t_0 is the time of passage of a particle in a chamber with respect to the calibrated time pedestal t_{trig}. How can we refer the HH trigger efficiency to the clock of the chamber?

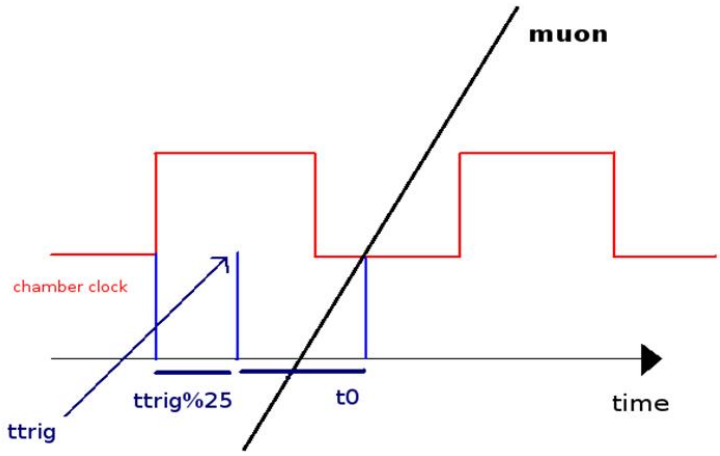

Figure 3.13: *Relevant times in a DT chamber. Clock fronts are the integers divisible for 25 of the TDC counts. The* t_0 *parameter of each segment is the time of passage of the muon with respect to the* t_{trig}.

Having all the t_{trig} we can extrapolate the clock counts. Clock fronts (in ns) are the integers divisible for 25 of the TDC counts. We have, for each chamber, the situation plotted in Fig. 3.13 .

All the t_{trig} used in the construction of segments of run 68021, calibrated for each superlayer of each chamber using the time box, are stored in a database.

For each DT chamber we can refer the HH trigger efficiency to the clock by simply shifting the zero of the time scale for the rest of the division by 25 ns of the t_{trig} that we indicate as $t_{trig}^{\%25}$.

$$\mathrm{Eff}^{HH}_{rel\ mod25}(t_0) = {}^{ABS}\mathrm{Eff}^{HH}_{rel\ mod25}(t_0 + t_{trig}^{\%25}) = {}^{ABS}\mathrm{Eff}^{HH}_{rel\ mod25}(t)$$

where in the last action we have defined $t \stackrel{def.}{=} t_0 + t_{trig}^{\%25}$. The time-zero ($t = 0$) of ${}^{ABS}\mathrm{Eff}^{HH}_{rel\ mod25}(t)$ corresponds to the chamber clock front. We call this time frame of reference *"bx time frame"*.

This is very important, we now know the DT chamber trigger behavior in every 25ns-wide time interval between two successive clock fronts. The trigger of the chamber behaves in this way always, every time the chamber receives the clock signal.

3.4.2 HH trigger efficiency, an effect due to hardware system

As described previously (sections 2.2.1 and 3.1.1) the level 1 trigger is entirely based on electronic devices. So we would expect the variation of HH trigger efficiency to be an electronic effect, entirely based on the hardware

characteristics of the chambers. We expect the HH trigger efficiency as function of the time t (i.e. time with respect to the clock front, an absolute time reference bound by the TTC clock signal with the electronic chain) to be the same for all the chambers of the same type, i.e. chambers that have the same hardware electronic system.

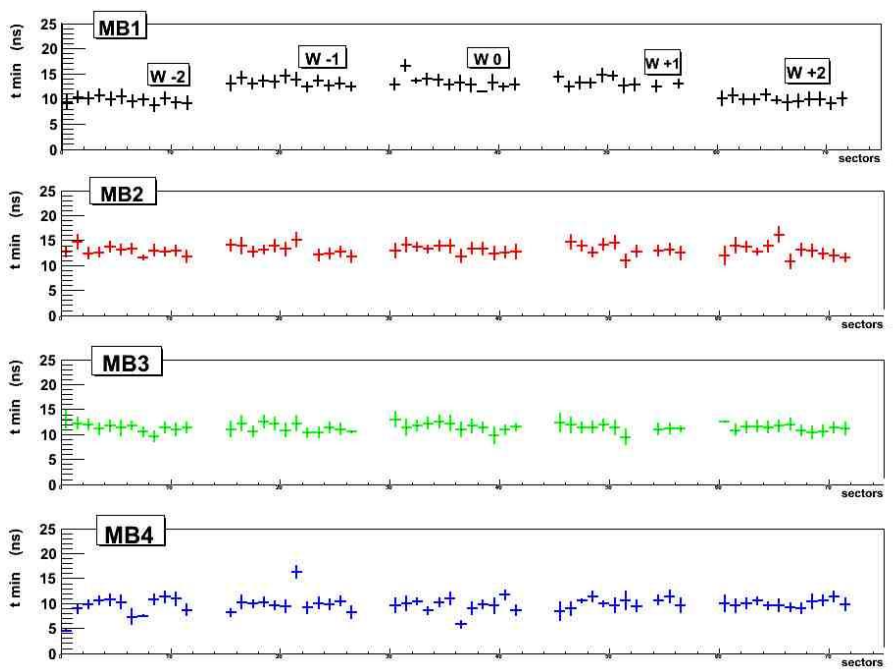

Figure 3.14: *t_{min} of all the CMS DT chambers*

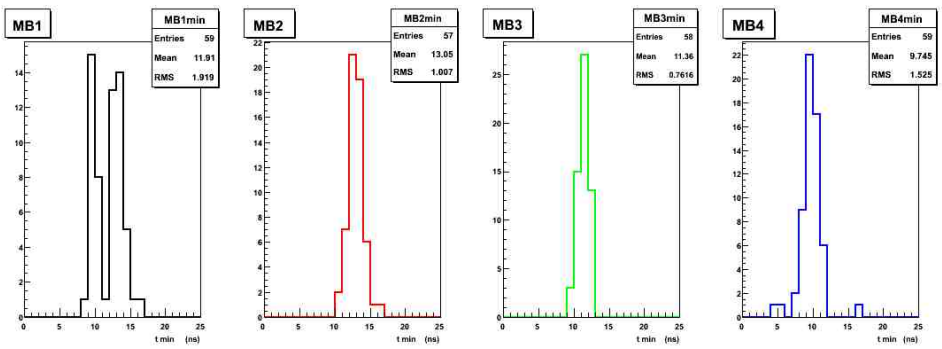

Figure 3.15: *t_{min} distribution for the four DT chamber types*

To confirm this we evaluate all the t_{min} in the *bx time frame* for all

the CMS chambers. Chambers of the same type [4] would have equal t_{min}s. In Fig. 3.14 we show the times of minimum efficiency t_{min} for all CMS chambers. The four graphics correspond to the four chamber types. In ordinate there is t, in abscissa chambers are grouped per wheel, every point is a different chamber, one of each type for each sector.

All the t_{min} in the four graphics of 3.14 are projected in the t-axis. The result is reported in the histograms of Fig. 3.15 showing the distributions of t_{min} for the four chamber types.

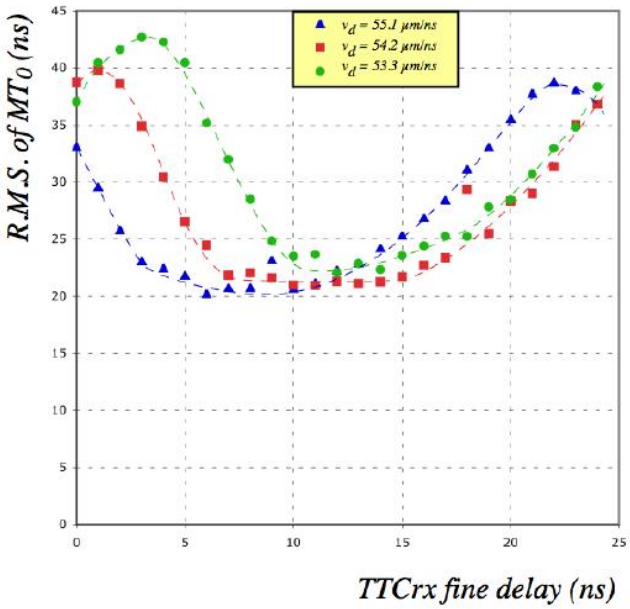

Figure 3.16: *Dependence by the drift velocity of the HH relative trigger efficiency*

We see that the t_{min}s are almost the same for each chamber type; they distribute normally (except in MB1 as we will see soon). This is exactly what expected. We note that in MB1 chambers of the wheels +2 and -2 the t_{min} is on average lower of 3-4 ns than in the other MB1chambers. This effect is due to the return of the magnetic field lines. In the MB1 chambers of wheels ± 2 there is a stronger magnetic field that change the drift velocity, and then the HH trigger efficiency shape. The effect of a different drift velocity on the HH trigger efficiency function as function of time ($\sim$ TTCrx delay) has been already measured and predicted in [23]. In Fig. 3.16 we see how the TTCrx fine delay value that maximize the synchronization indicator ($R.M.S.$ of MT_0) shifts for different drift velocities.

[4] there are four "types" of DT chambers: MB1,MB2,MB3,MB4. Chambers of the same type have the same hardware characteristics.

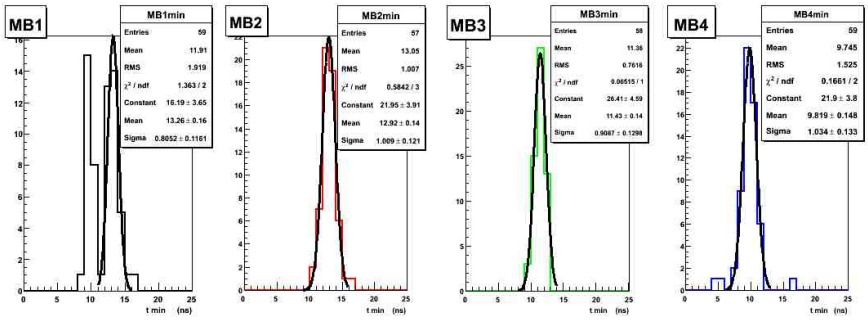

Figure 3.17: *t_{min} distribution for the four DT chamber types fitted with a Gaussian.*

In Fig. 3.17 the four t_{min} distributions are fitted with Gaussian functions. The fits give the mean values and the standard deviations of the t_{min} for the four chamber types. We report the results in table:

DT chamber	$< t_{min} >$	$\sigma(t_{min})$
MB2	12.9 ± 0.1 ns	1.0 ± 0.1 ns
MB3	11.4 ± 0.1 ns	0.9 ± 0.1 ns
MB4	9.8 ± 0.1 ns	1.0 ± 0.1 ns
MB1 (wheel 0 ± 1)	13.2 ± 0.1 ns	0.8 ± 0.1 ns
MB1 (wheel ± 2)	9.8 ± 0.1 ns	0.55 ± 0.1 ns

3.5 Conditions at LHC start-up

In the previous sections we have seen how the trigger efficiency in the 25 ns wide time range of a bx is a time function with a specific, known, shape. We want now to define a procedure for the trigger fine synchronization for the first LHC bunched beam. The muons from pp interaction will hit the DT chambers in a specific position in-time with respect to the clocks of the chambers. We want now to show how it is possible to optimize the trigger efficiency at the start-up by setting the TTCrx fine delay. We want to make the muons to hit all the DT chambers in the maximum efficiency range.

At LHC start-up the protons collisions will occur every 25 ns (time of bunch crossing). The muons, created by the pp collisions, will reach the Drift Tubes chambers at a fixed phase with respect to the bunch crossing time. The DT segments will be reconstructed using the 3-parameters algorithm, so we will have the t_0 for each segment. The DT segments will be constructed using approximated t_{trig} values initial values calculated from the cosmic calibrations. The t_0 distributions, in every chamber, will be tight since the muons will be generated every 25 ns (like in the bunched beam tests of 2004

which are referred the analysis of [23]). The t_0 distribution will be dominated substantially by statistic and systematic[5] errors since the protons collisions will occur in a very small time interval ($\sim$ 0.3 ns wide) and thus the muons could be considered almost perfectly synchronous. The t_0 distribution is expected to be Gaussian with a sigma of $\sim$ 2-3 ns [6].

In order to have an idea of this we use a Montecarlo simulation of the start-up conditions containing few thousand events. We are only interested in the segments information of the MC since we want to study the t_0 distributions in the chambers. For MC data we construct only the class *DTRecSegment4DCollection*, we store the data in a ROOT Tree.

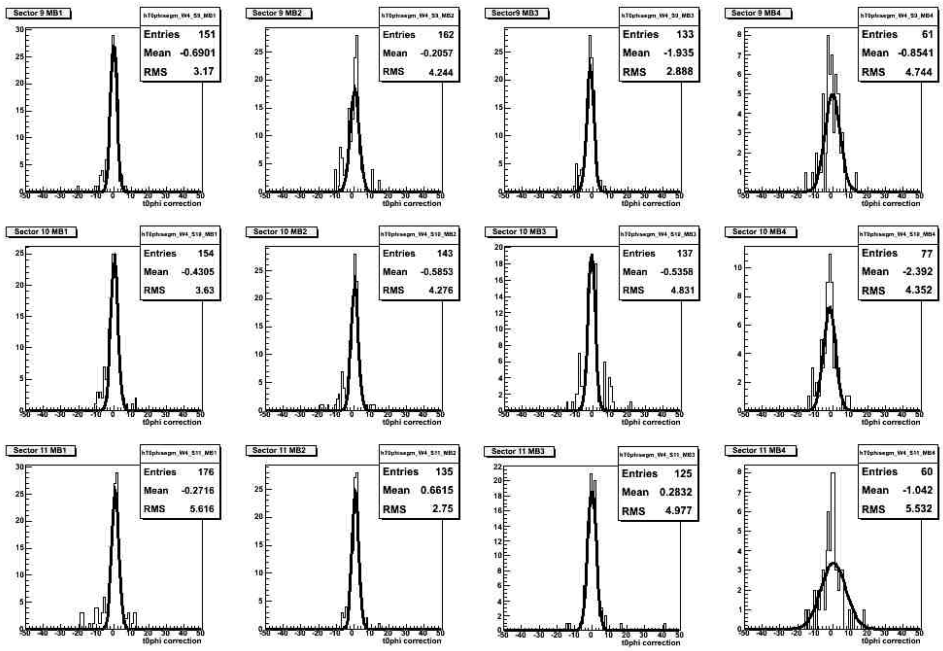

Figure 3.18: *t_0 distribution in some DT chamber at the LHC startup. Simulated data.*

In Fig. 3.18 we plot some t_0 distributions relative to different chambers (sectors 9-10-11 of wheel 2). The distributions contain only roughly one hundred of events each one but, as we can see, they are enough definite (all but someone like the bottom right one of Fig. 3.18). We see that, as expected, the t_0 distributions are much tighter than the t_0 distributions of cosmic muons. We perform a Gaussian fit on the t_0 distributions of all the 250 CMS DT chambers. We evaluate the resolutions (σ) of these distributions.

[5]Corrections can be done to the systematic errors effects as explained in the next chapter.

[6]In the next chapter we will evaluate the t_0 resolution.

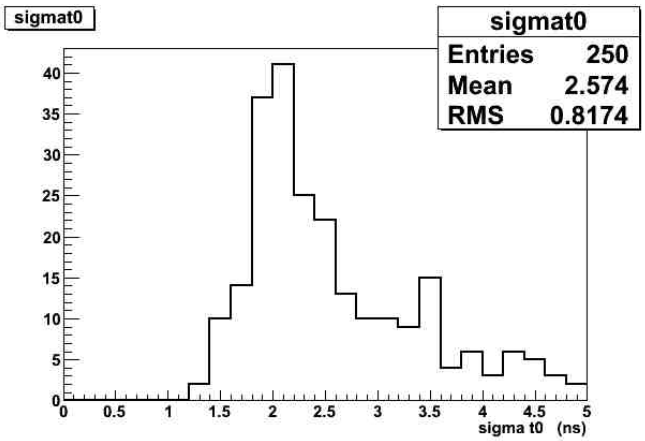

Figure 3.19: *σ of t_0 distributions in all the CMS DT chambers at the LHC startup. Simulated data.*

The plot of all the 250 σ of the t_0 distributions in the DT chambers is shown in Fig. 3.19 We see that the mean sigma is of the order of 2-3 ns (the tail on distribution is due to chambers that have very few events like the last distribution of Fig. 3.18). We must remember that these distributions contain only hundred events each one; let's note that having a sigma 2-3 ns the error of the mean value is 0.2-0.3 ns. We have a good identification of the mean value of the t_0 distribution using very few events.

3.5.1 Fine synchronization at LHC start-up

To perform the trigger fine synchronization for the LHC start-up means to set the right values of TTCrx fine delay in every DT chamber in order to make the muons from pp interaction to reach each chamber inside the interval of maximum efficiency. The function ${}^{ABS}\mathrm{Eff}^{HH}_{rel\ mod25}(t)$ for $t \in [0, 25]ns$ has an almost constant interval where the efficiency is maximum: this interval is approximately 10 ns wide. The muons at the LHC start up will distribute in time in all the DT chambers with a width of maximum 10 ns (see section 3.5). If the chambers are well synchronized the center of the t_0 distribution of the pp muons must be 12.5 ns far from the time point of minimum efficiency $t_{0\ min}$. We know from our analysis that t_{min} is at fixed position with respect to the clock fronts for every chamber type. So at the LHC start up only few hundred muon events in every DT chamber will be sufficient to perform the trigger fine sinchronization. The TTCrx fine delays of each chamber will have to be set in order to have the t0 distribution of each chamber centered 12.5 ns far from the point of minimum efficiency.

Let's sketch the fine synchronization procedure at the LHC start-up (the

following analysis is performed on every CMS DT chamber):

- The segments will be reconstructed using approximately values of time pedestals t_{trig}
- Using only a hundred of events we know the mean value $\langle t_0 \rangle$ of the tight t_0 distribution with an error of 0.2-0.3 ns
- We compute the distance from the $\langle t_0 \rangle$ to the clock front by adding $t_{trig}^{\%25}$ [7]; the $\langle t \rangle = (\ \langle t_0 \rangle + t_{trig}^{\%25}\ )\%25$ must be 12.5 ns far from t_{min}
- The TTCrx fine delay that must be applied is $= t_{diff} \stackrel{def.}{=} \langle t \rangle - (t_{min} - 12.5\text{ns})$

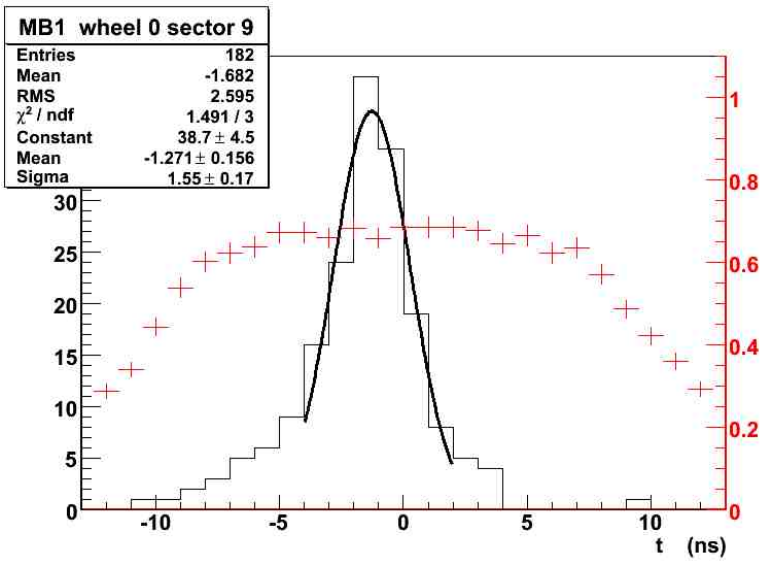

Figure 3.20: *Simulation: LHC start-up moment for fine synchronization. Position of the t_0 distribution with respect to the HH relative efficiency function.*

As example we report in Fig. 3.20 the simulation at the start-up moment for a test chamber (MB1, sector 9 of wheel 0). We see that the t distribution is centered approximately 14 ns far from the t_{min}. In order to have this chamber correctly synchronized we must apply a TTCrx fine delay of -1.2 ns.

[7] With %25 we intend the rest of the division for 25 .

Chapter 4

Search for Heavy Stable Charged Particles exploiting the track time resolution

Almost all the theoretical models for new physics beyond the Standard Model foresee the existence of new "exotica" particles below the TeV scale. The search for new particles is one of the main goals of the LHC. As presented in section 1 some versions of supersymmetry theory or extra-dimensions theories foresee the existence of new *"Heavy Stable Charged Particles" (HSCP)*, i.e. meta-stable particles charged under the $U(1)$ or $SU(3)$ gauge group [28]. In this chapter we study the possibility of searching for HSCP at the CMS experiment using the data of the Drift Tube chambers of the barrel. We are interested in the electrically charged HSCPs that behave like muons, crossing the whole CMS detector. These are characterized by low speed ($\beta \sim 0.5$) together with high momentum because of their great mass (of the order of hundreds GeV). The separation between muons and HSCP could be done by measuring the speed of particles that cross the muon system.

The Drift Tube chambers allow the reconstruction of track segments that assigns a time parameter t_0 together with the position and slope, as presented in the previous chapters (section 2.2.2). We can infer from t_0 the absolute time of passage of a particle in each DT chamber; using the time together with the position of the segments in the tracks it is possible to measure the speed of the muon-like particles. If we have a good resolution it will be possible to discriminate the kind of a particle by measuring its speed.

In this chapter we will firstly present some general features of the search for HSCP at CMS. Then we will develop the segment time analysis on cosmic data in order to optimize the time measurement taking into account the

systematic errors. The time parameters t_0 will be referred to a physical time scale. We will estimate the time resolution for cosmic-rays and the results will be compared to the simulated cosmic Montecarlo data.

We will develop an algorithm for β estimation. The β resolution and its sources of uncertainty will be analyzed.

Afterward we will develop the time analysis in order to apply it on the synchronous particles from pp interactions at the LHC. Our algorithms for time and β measurement will be tested on MC pp simulated data.

Finally a sample of ${}^{KK}\tau$ (300 GeV) will be analyzed. We will show how it is possible to discriminate between these HSCPs and muons by looking at the reconstructed particle speed.

4.1 HSCP features

In our analysis we will be interested in HSCPs carrying only electric charge. HSCPs arise in models in which one or more new states exist and which carry a new conserved, or almost conserved, global quantum number. Supersymmetry with R-parity and extra dimensions with KK-parity provide examples of such models. In these models the predicted meta-stable electrically charged particles are respectively the s-tau and the kk-tau. Their mass is related to the theory parameters that are unknown, but in large regions of the parameters space is predicted to be of the order of several hundred of GeV.

The typical signature of such HSCPs is:

- *A muon-like behavior*: the electrically charged meta-stable exotic particles are predicted to interact mostly electromagnetically crossing the whole CMS detector as a muon.

- *High momentum*: HSCPs could be produced by the Large Hadron Collider (LHC) as a result of direct pair-production processes or as final products of the decay chain of heavier exotic particles. In both cases the particles are predicted to have large momentum, of the order of several hundred GeV.

- *Low speed*: being massive these particles are characterized by low speed together with high momentum. The relativistic β factor is given in term of momentum p and energy E by the formula $\beta = \frac{p}{E}$. For a particle with a mass of the order of its momentum we see that the β factor assumes values significantly smaller than 1.

This signature is unique. If these particles are produced at the LHC and we are able to measure their speed with sufficiently good resolution we will be able to separate them from muons.

The following results are relative to an analysis performed on simulated HSCP data samples described in [29]. Supersymmetric $\tilde{\tau}_1$ events generation has been performed with PYTHIA [30] version 6.409 by enabling all sparticle production subprocesses. Right-handed KK τ simulated events have been generated using CompHEP [31] with the MUED model [32]. Full simulation of the particle propagation in the CMS apparatus is performed with the Geant4 [33] package. The standard Geant4 is not designed to handle the propagation in matter of exotic particles like HSCPs. The interaction of sleptons with matter can be described in terms of the standard electromagnetic interactions: for $\tilde{\tau}$ or KK-τ particles, all that is needed is to register the particles (by providing their physical properties like mass, spin, etc.) and the existing Geant4 processes like ionization and multiple scattering that the particles are supposed to undergo.

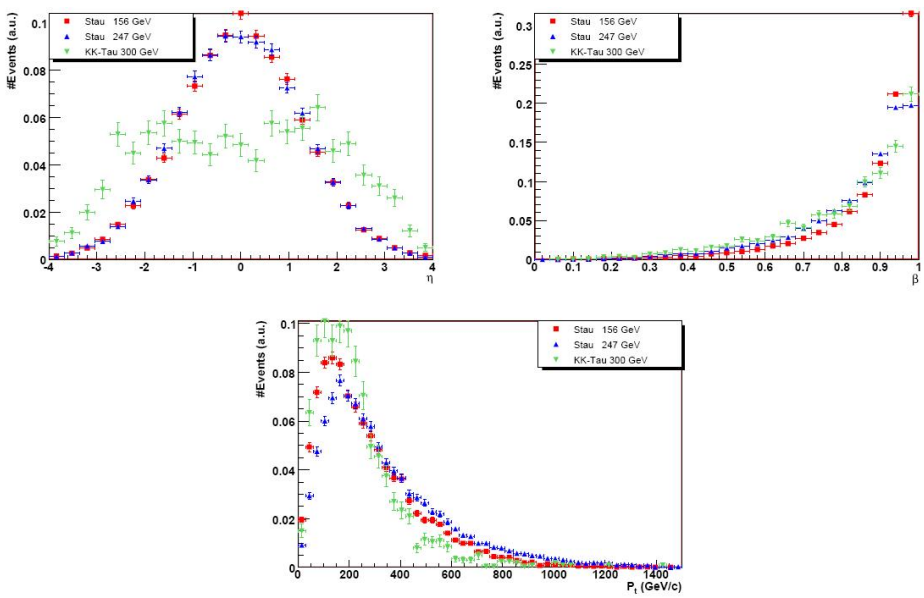

Figure 4.1: *Distributions of the β, η and p_T of all HSCPs in the event. In each plot the distribution from the two mGMSB $\tilde{\tau}_1$ and the MUED KK τ simulated samples are reported.*

As for the mGMSB $\tilde{\tau}_1$ samples, the details of the MUED KK τ generation and the distributions of some relevant kinematical variables are shown in table below and Fig. 4.1. The plots show the distributions of the β, η and p_T of all HSCPs in the simulated events. mGMSB and mUED models differ by the HSCP η distribution.

Data Sample	Cross sect (pb)	Nr events	Int $\mathscr{L}$ (fb^{-1})	HSCP in $\lvert\eta\rvert < 2.4$ (%)	HSCP in $\lvert\eta\rvert < 0.9$ (%)
mGMSB $\tilde{\tau}_1$ (156 GeV)	1.19	6899	5.78	97.6	72.6
mGMSB $\tilde{\tau}_1$ (247 GeV)	0.097	6899	71.1	97.5	70.9
mUED KK τ (300 GeV)	0.020	1000	50	84.7	40.9

4.1.1 Trigger for HSCP

At trigger level, a lepton-like HSCP has a high probability of being reconstructed as a muon. Reconstruction can fail, however, if the HSCP is too slow. In this case it will reach the muon system out of time with respect to typical relativistic muons and, therefore would either be reconstructed in the wrong bunch crossing or fail to be reconstructed at all because of quality cuts imposed by the Level-1 Trigger (L1) or High Level Trigger (HLT) algorithms.

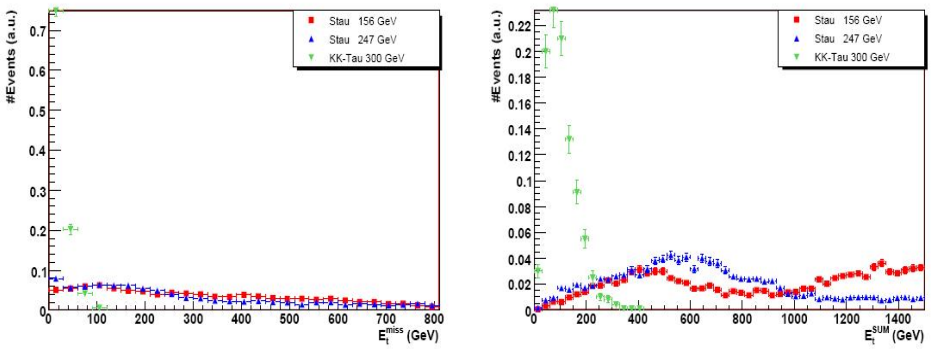

Figure 4.2: *Distribution of E_t^{miss} , E_t^{SUM} . In each plot the distribution from the two mGMSB $\tilde{\tau}_1$ and the MUED KK τ simulated samples are reported.*

HSCPs can also give rise to a sizeable missing energy, unless back-to-back pair production cancels out individual contributions. The missing energy trigger neither suffers from the timing issues described above, nor does it depend on whether HSCPs are reconstructed successfully as muons because muons are not expected to be considered in the missing energy estimate at trigger level. The missing energy trigger, as well as other calorimeter-based triggers (like E_t^{SUM}), can be very efficient for HSCP events. Plots of the missing transverse energy in the generated data sample are shown in Fig. 4.2 .

A comprehensive study has been performed on the generated samples in order to evaluate the expected trigger efficiencies and their dependence on the threshold. All the results are reported in [29].

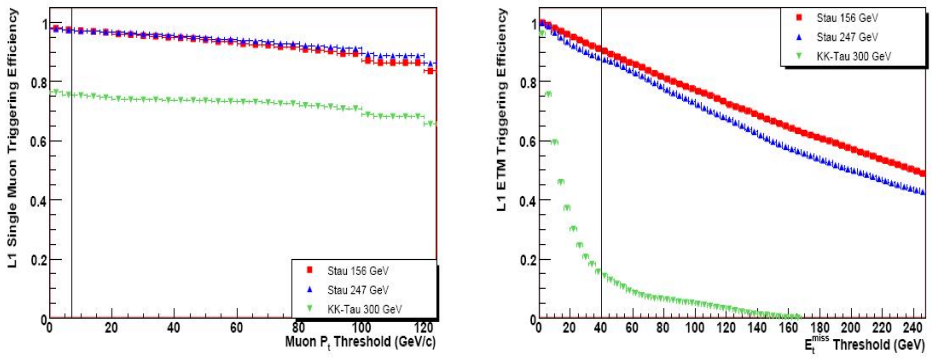

Figure 4.3: *Muon, MET, L1 trigger efficiency for the mGMSB $\tilde{\tau}_1$ and for the right-handed KK τ as a function of the corresponding trigger threshold.*

It has been shown that a Level-1 trigger efficiency of the order of 90% for $\tilde{\tau}$ and of the order of 80% for $^{KK}\tau$ can be reached at CMS with opportune thresholds on trigger parameters. We report some results in Fig. 4.3.

Even the HLT efficiency has been tested with similar good results.

4.1.2 Searching for the HSCP using the Drift Tube chambers of the barrel

Since the electrically charged HSCPs cross the whole detector like muons it results naturally to think about the opportunity of detecting them using the muon system. We are interested in particular in the opportunity of searching for HSCP using the drift tube chambers of the barrel. Generally speaking we can separate a HSCP particle from a muon by evaluating the speed. If we think that track segments are reconstructed in the DT chambers using the *3-parameters fit* (section 2.2.2) we immediately realize that a speed measurement is possible: indeed the 3-parameters fit assigns to each segment a time parameter t_0 together with the position information. Using the reconstructed standalone tracks composed by several segments we should be able to estimate the speed of particles from the time parameter t_0 of segments.

4.2 Track crossing times

In the following section we will study in details the features of the t_0 parameter of the segments and particularly the systematics. We will link it to

the time of flight of the particle by referring it to an absolute scale. Finally we will evaluate the obtainable track time resolution.

All our analysis are performed on the CMS run 68021 cosmic data [25] using the segments collection *DTRecSegment4DCollection* and standalone tracks collection *TrackCollection*. The characteristics of these data have already been reported in section 3.3.

The percentage of standalone legs with segments respectively in four, three, two and one chambers are reported in the following table summary. The percentage of segnets with the number of layers with associated hits in the ϕ view (from three up to eight) are reported as well.

Standalone tracks	
SA_{4st}/SA_{all}	50%
SA_{3st}/SA_{all}	35%
SA_{2st}/SA_{all}	11%
SA_{1st}/SA_{all}	4%
Segments	
$Seg_{8layers}/Seg_{all}$	63.7%
$Seg_{7layers}/Seg_{all}$	16.5%
$Seg_{6layers}/Seg_{all}$	4.3%
$Seg_{5layers}/Seg_{all}$	3%
$Seg_{4layers}/Seg_{all}$	8.6%
$Seg_{3layers}/Seg_{all}$	3.4%

From the angular distribution of cosmic-rays, the percentage of cosmics entering the detector in sector 4 and 10 (where chambers are horizontal) with an angle below than 45 degrees with respect to the normal direction of the chambers is 82% and goes below 18% in sectors 1 and 7 (where chambers are vertical). The CMS chambers have been built to have high reconstruction efficincy ($\sim$ 99%) for high energy particles coming from the interaction vertex, so with an angle of incidence less than 30 degrees. The local reconstruction efficiency decreases for larger angles.

4.2.1 Optimizing the time parameter t_0

In section 2.2.2 we introduced the t_0 parameter assigned to each segment when the reconstruction using the *3-parameters fit* is computed [1]. The t_0 represents the time correction with respect to the assumed time pedestal t_{trig} coming from the calibration procedure. This fact implies that if a particle crosses the middle of a DT chamber at time t_μ in the segment reconstruction

[1] From now on with t_0 we will always refer to the $t_{0\ \phi}$ computed with the fit on the hits on the two SL_ϕ.

we will have a $t_0 = t_\mu - t_{trig}$. Thus each segment hit is reconstructed from a TDC time t_{TDC} with a v_{drift} using the drift time

$$t_{drift,ij} = t_{TDC,ij} - t_{trig,j} - t_{0,ij} \tag{4.1}$$

where i is the measurement index and j the chamber index.

There are systematic effects that must be taken into account for computing the absolute time of each segment in a chamber. We can identify two contributes:

- *Signal propagation along the wire*: The electric signal generated by the avalanche of electrons propagates along the anode wire of each cell to the front-end discriminator (F.E.). Since the propagation time depends on the impact point, a correction must be applied event by event.

- *Track angle correlation*: due to the cell field shape for large angle tracks, the first ionization electrons arriving to the wire make a shorter path than the electrons released near the wire plane. It has been shown that the extra shift in time due to angle of incidence has a parabolic dependence with respect to $\tan\phi_{loc}$ [16].

Therefore the correct expression for the drift times should be:

$$t_{drift,ij} = t_{TDC,ij} - t_{trig,j} - t_{0,ij} - t_{w,ij} - t_{\alpha,ij} \tag{4.2}$$

where $t_{w,ij}$ is the signal propagation time along the anode wire, $t_{\alpha,ij}$ is the phenomenological correction used to take into account the nonlinearity of the space-time relation for inclined tracks.

The correction for these systematic effects has been evaluated and the results are reported in [16]. In Fig. 4.4, as example, is shown the $t_{0\ \theta} - t_{0\ \phi}$ as function of $\tan\phi$.

The correction with respect to the signal propagation time along the wire lead to a signal propagation velocity estimation. The results obtained in [16] gives a $v_{prop} = 24.0 \pm 0.1$ cm/ns .

Systematic corrections for cosmic data of run 68021

The previously results, relative to [16], have been obtained in particular experimental conditions. Cosmic data have been collected using two MB3 type DT chambers parallel to the ground in autotrigger mode. Being horizontal the chambers were uniformly illuminated.

The experimental conditions of our data collecting (run 68021) are different. Indeed the data are collected with the CMS chambers not uniformly illuminated. In section 2.2.2 we explained that t_{trig} from calibrations are mean values that change their physical meaning for different data collecting

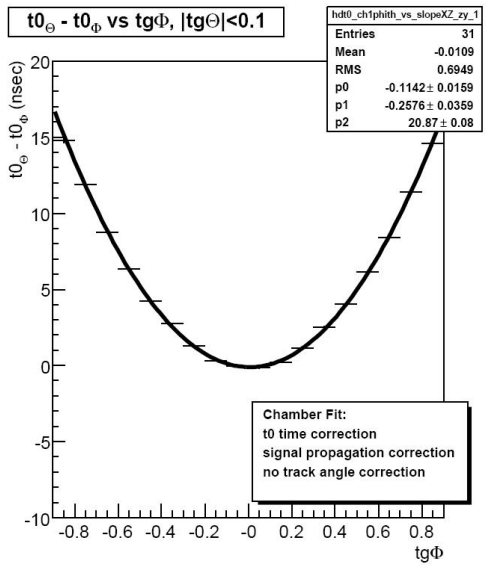

Figure 4.4: t_0 *sistematic dependences from the angle of incidence, [16].*

conditions: if each chamber is uniformly illuminated, which is the case for pp collisions, t_{trig} represents the time-zero of a muon crossing the chamber center, the average signal propagation time is equivalent to the propagation time for a signal produced in the middle of the wire while the angular effect would be symmetric with respect to the vertical direction. Instead during cosmic data taking the chambers are not uniformly illuminated. The CMS geometry has been studied in order to be optimized for detecting particles coming from pp interaction. For cosmic particles the CMS geometry is not advantageous: cosmic muons come from the top of CMS with an angular distribution symmetric with respect to the vertical direction. The cosmic distribution is asymmetric in z becuause the large majority of cosmic rays comes from the shaft above the wheel -2. The t_{trig} calibrated for one of these stations is calculated from a cosmic track distribution that has different symmetry from chamber to chamber. Thus, for our data, the systematic dependences must be evaluated chamber by chamber.

In addition to wire propagation and angle correction that must be done track by track we can have in each chamber a residual absolute offset, common to all segments in that chamber, due to particle distribution symmetry, data calibration and hardware settings. This absolute offset must be subtracted in order to make comparable the track times in different stations.

In the systematics correction the effect of the cosmic topology described above lead to a different constant terms in the wire position and angle of in-

cidence dependence. We can summarize the systematic correction procedure as follows (the following analysis is performed on every DT chamber):

- The dependence of t_0 as function of y_{loc} [2] is known from [16]. We thus correct the t_0 parameter:

$$\Delta t_{0,ij}^{wire} = \frac{1}{v_{prop}} \cdot y_{loc,ij} - \frac{1}{v_{prop}} \cdot \langle y_{loc,ij} \rangle_i$$

  where i is the measurement index, j the chamber index, being $v_{prop} =$ 24.0 cm/ns as measured in [16] and [17].

- The parabolic angular dependence of t_0

$$\Delta t_0^{ang}(\tan\phi_{loc}) = p_{0,j}^{ang} + p_{1,j}^{ang} \cdot \tan\phi_{loc,ij} + p_{2,j}^{ang} \cdot \tan^2\phi_{loc,ij}$$

  as computed in [16] has been used for removing angular systematic. $p_{0,j}^{ang}$ and $p_{1,j}^{ang}$ are almost equal to zero while $p_{2,j}^{ang} \simeq -20$ ns we can see in Fig. 4.4. We correct the t_0 parameter:

$$\Delta t_{0,ij}^{ang} = \Delta t_0 \left(\tan\phi_{loc,ij} - \langle \tan\phi_{loc,ij} \rangle_i\right)$$

  where i is the measurement index, j the chamber index.

- We call

$$t_{cor,ij} \stackrel{def.}{=} t_{0,ij} - \Delta t_{0,ij}^{wire} - \Delta t_{0,ij}^{ang}$$

  We evaluate the mean value of the $t_{cor,ij}$ distribution by fitting the distribution with a Gaussian. Considering $\langle t_{cor,j} \rangle$ as the absolute offset we reach the final correct time:

$$t_{ij} \stackrel{def.}{=} t_{cor,ij} - \langle t_{cor,ij} \rangle_i$$

  where i is the measurement index, j the chamber index.

As example we report in Fig. 4.5 the $t_{cor,ij}$ distribution for chamber MB3 of sector 3 of wheel +1, the residual offset is $\langle t_{cor,j} \rangle = -2$ ns.

[2] y_{loc} refers to the local frame of reference of each chamber where x_{loc} is the parallel to chamber direction in ϕ view, y_{loc} is the parallel to chamber direction in θ view while z_{loc} is the perpendicular to chamber direction. The zero of the ith-axis is located in the middle of the chamber length in the ith direction. There is also an angular frame of reference: ϕ_{loc} is the angle with respect to the perpendicular to chamber direction in the ϕ view while θ_{loc} is the angle with respect to the perpendicular to chamber direction in the θ view.

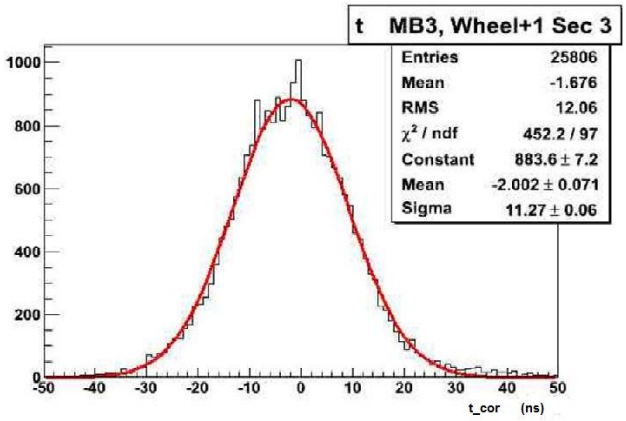

Figure 4.5: *$t_{cor,ij}$, i.e. time after correction for signal propagation along the wire and angle of incidence, distribution for chamber MB3 of sector 3 of wheel +1.*

4.2.2 t physical meaning

Let's focus now on the physical meaning of the time parameter t. The t_0, assigned to each segment when the reconstruction with 3-parameters fit is done, represents the time correction with respect to the time pedestal t_{PED}. We explained in section 2.2.2 that the segment reconstruction with the 3-parameters fit is particularly useful for cosmic data: indeed cosmic muons reach the chambers out-of-time with respect to the system clock. We have already pointed out the t_0 dependence from signal propagation and angle of incidence: the presence of these dependences means that even a particle in-time, synchronous with the clock, can be systematically reconstructed with a $t_0 \neq 0$. This can happen if, for example, the particle hits the chamber distant from the position which the t_{trig} refers (typically the center of the chamber) or if the particle hits the chamber with an angle different from zero. The t_{cor}, defined in section 4.2.1, makes the time correction independent from where the particle hits the chamber and with what inclination. A particle in-time will have the t_{cor} always equal to zero within the statistical error if the time calibration is correct. Finally the t, also defined in section 4.2.1, where the absolute offset $\langle t_{cor} \rangle$ is subtracted, makes comparable all the times in all the chambers. The $\langle t_{cor} \rangle$ subtraction adjusts the calibration errors: now the mean values of the t distributions are all equal to zero.

To understand what the time t really represents let's use the standalone tracks: all the times relative to the segments of a standalone track are equal if the path of the particle is equal to the average path. By looking at Fig. 4.6, relative to one standalone leg, we see that if a particle travels the average path, represented in figure by the blue track on the left, it will have all the times equal; in particular, if the first time is equal to zero, all the subsequent

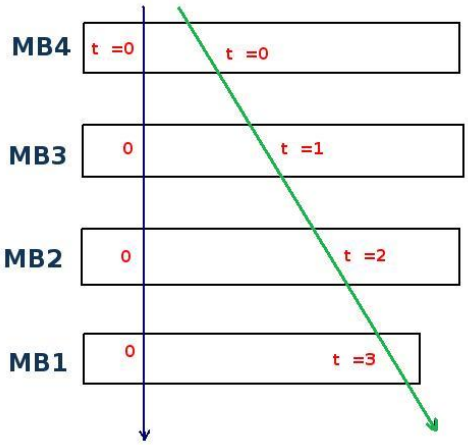

Figure 4.6: *Time parameters normalization inside one standalone leg.*

times will be equal to zero as well. Differently if the particle travels a longer path, for example because of its inclination, the time registered will be growing for successive chambers; in particular if the first time is equal to zero the subsequent times will be major then zero.

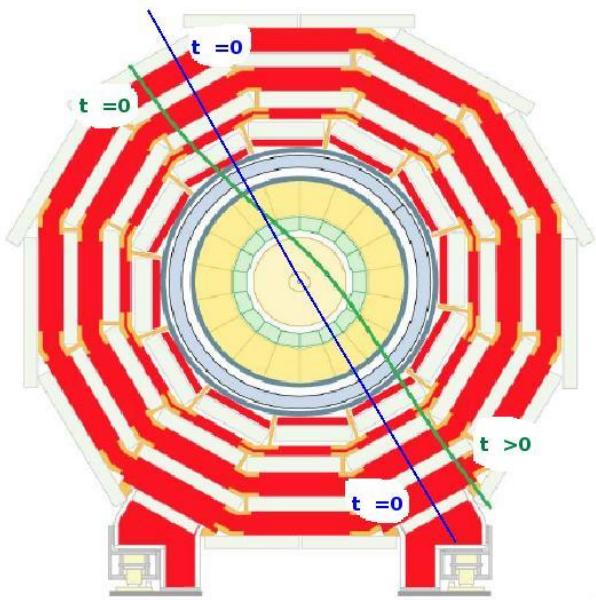

Figure 4.7: *Time parameters normalization inside CMS.*

Extending this fact to a global view we can say that the times of a global

muon track composed by two stand alone legs behave in the same way: times t are all equal for a path that is symmetrically composed by two average paths, they are different for longer or shorter paths. In Fig. 4.7 the situation is presented. The average path is the blue one: it has all the times equal. A longer path, as the green one in figure, has growing times for successive chambers.

It is now evident that a central role is played by the path lengths. In particular it is important to evaluate the mean paths traveled by the particles.

In the following analysis we will use the standalone tracks. Their main features are summarized in section 3.3. For every stand alone track we will be able to use the information relative to segments that compose the track.

Mean path estimation

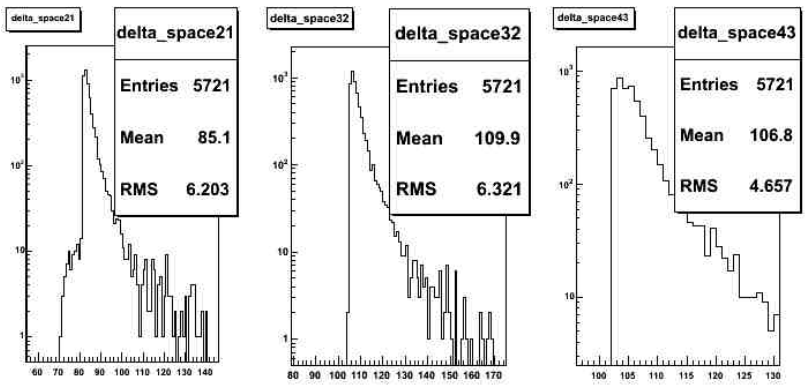

Figure 4.8: $d_{j,j+1}$ *distributions.*

Let's proceed step by step starting by evaluating the mean paths between successive chambers in each sector. For segments of a same standalone leg we use the following formulas to evaluate the distances traveled by the particles:

$$d_{12,i} = |\vec{x}_{1,i} - \vec{x}_{2,i}| \qquad \text{dist. MB1-MB2}$$

$$d_{23,i} = |\vec{x}_{2,i} - \vec{x}_{3,i}| \qquad \text{dist. MB2-MB3}$$

$$d_{34,i} = |\vec{x}_{3,i} - \vec{x}_{4,i}| \qquad \text{dist. MB3-MB4}$$

where i is the measurement index,$\vec{x}_{j,i}$ is the reconstructed position of the ith segment inside the jth chamber.

The $d_{jj+1,i}$ distributions are showed in Fig. 4.8. The average paths between the chambers are summarized in table.

$\langle d_{12} \rangle$	$\langle d_{23} \rangle$	$\langle d_{34} \rangle$
85cm	110cm	107cm

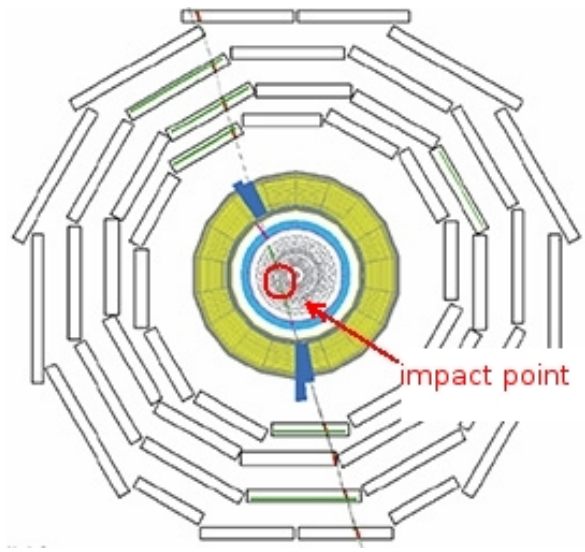

Figure 4.9: *Impact Point (IP) for cosmic muons.*

In order to extend the mean path evaluation to a global view inside CMS an important quantity must be introduced: the *impact point (IP)*. It is the closest to z-axis point of the cosmic muon trajectory. The impact point of a standalone track is shown in Fig 4.9. We use the IP position $\vec{x}_{IP}$, stored in the stand alone available information, to calculate the distance traveled by each cosmic muon inside CMS.

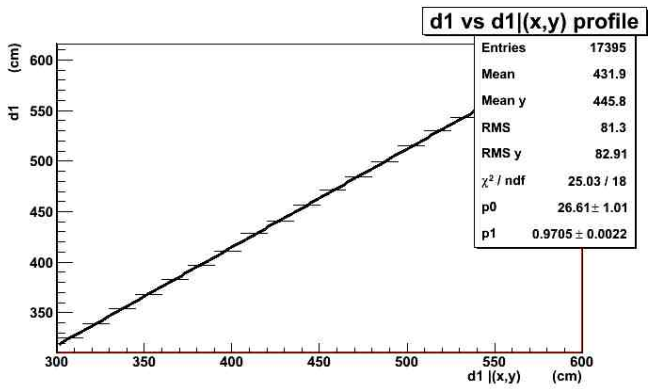

Figure 4.10: $|\vec{x}_{1,i} - \vec{x}_{IP,i}|$ *vs* $|\vec{x}_{1,i}|_{(x,y)} - \vec{x}_{IP,i}|_{(x,y)}|$ *scatter plot profile.*

The average path $d_{1,i} = |\vec{x}_{1,i} - \vec{x}_{IP,i}|$ between the impact point and the

segment in MB1 of each standalone leg depends just by the projection in the (x, y) plane. We verify that by dividing radially the internal zone of CMS obtaining outer circles of radius r. We construct the scatter plot

$$|\vec{x}_{1,i} - \vec{x}_{IP,i}| \quad \text{vs} \quad |\vec{x}_{1,i}\big|_{(x,y)} - \vec{x}_{IP,i}\big|_{(x,y)}|$$

where, as usual, i is the measurement index and with $X\big|_{(x,y)}$ we indicate the projection on the (x, y) plane. The scatter plot profile is reported in Fig. 4.10 .

We see that, for each radius r, the mean distance $\langle d_{1,r} \rangle$ is almost equal to the mean value of distance between the segment in MB1 and the outer circle of radius r projected in the (x, y) plane, i.e. $\langle |\vec{x}_{1}\big|_{(x,y)}| - r \rangle$. From now on we will assume

$$\langle d_{1,r} \rangle = \langle |\vec{x}_{1}\big|_{(x,y)}| - r \rangle$$

Physical time scale

We are now able to refer each t relative to a muon [3] track segment to an absolute scale $\mathbb{R}_t$. Having a track, if we fix a time-zero in a point of the track as zero of a time scale $\mathbb{R}_t$ we will be able to include each earlier or successive time parameter t in that scale.

Let's make an example. We have a track that extends on a whole sector (chambers from MB1 to MB4), composed by four segments, each one equipped with its space-temporal information $(\vec{x}_k, t_k)_{k=1,2,3,4}$ (k is the segment index). If we take t_1 as time-zero of the time absolute scale $\mathbb{R}_t$ the time parameters $(t_k)_{k=2,3,4}$ can be referred to $\mathbb{R}_t$ as follows:

$$t_k \longmapsto t_k - t_1 + \frac{\langle d_{1k} \rangle}{c} \in \mathbb{R}_t \tag{4.3}$$

where $\langle d_{1k} \rangle$ is the mean path between the chambers MBk and MB1 estimated in the previously subsection.

In substance what is done in formula 4.3 is to add to the measured times t the time of flight of muons relative to the mean paths between successive chambers.

4.2.3 DT time resolution

We want now to estimate the time t resolution. We can work using only one standalone leg per event. We take, for each standalone leg, the time differences $\Delta t_j = t_j - t_{j+1}$ $(j = 1, 2, 3)$ between the 3 couple of consecutive chambers MB1-MB2, MB2-MB3 and MB3-MB4 [4]. We normalize the Δt to

[3] Remember that all the detected muons travel almost at the speed of light c since their mass is ~ 130 MeV and their momentum at least of the order of several GeV.

[4] In the following analysis, in order to look at the best results obtainable with cosmics, we will limit to standalone legs composed by four segments each one.

the previously estimated mean paths between consecutive chambers using the formula:

$$\Delta t_{ij}^n = \Delta t_{ij} \frac{\langle d_{ij} \rangle}{d_{ij}}$$

where i is the measurement index and j the couple-of-chambers index. We have, for each stand alone leg, up to three estimation of the same quantity Δt^n. So we can pose the constraint on the r.m.s. of Δt^n of the to be under 3σ

$$\mathrm{RMS}_{\Delta t_i^n} = \sqrt{\frac{\sum_{j=1}^{3} (\Delta t_{ij}^n - \langle \Delta t_{ij}^n \rangle_j)^2}{2}} < 3 \cdot \sigma(\mathrm{RMS}_{\Delta t^n})$$

the distribution of $\mathrm{RMS}_{\Delta t^n}$ is shown in Fig. 4.11). In this way we cut the possible tails in the $(\Delta t_j^n)_{j=1,2,3}$ distributions.

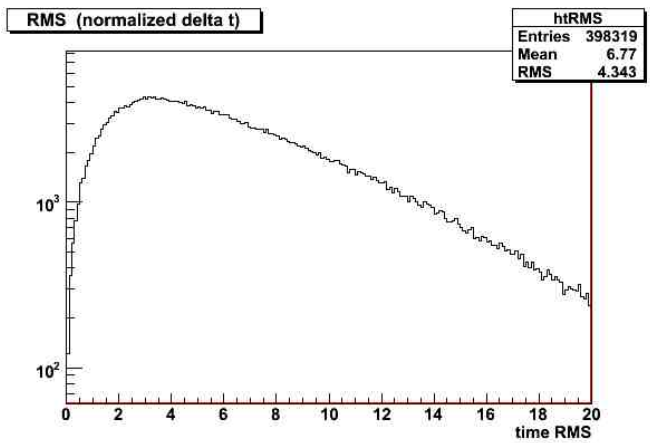

Figure 4.11: *$RMS_{\Delta t_i^n}$ distribution.*

The three $(\Delta t_j^n)_{j=1,2,3}$ distributions, relative to the three couples-of-chambers, are shown in Fig. 4.12 .

The resolution of these distribution is dominated by time error since the segment position is now within $\sim 100\mu$m and the track curvature in magnetic field in the external zone of CMS leads to a negligible correction on the path length. We have for these three distributions is $\sigma_{\Delta t^n} = 4.0 \pm 0.25$ ns that lead to a single time resolution:

$$\sigma_t = \frac{\sigma_{\Delta t^n}}{\sqrt{2}} = 2.8 \pm 0.18\text{ns}$$

Time at the Impact Point

The experimental conditions for predicting the entire particle motion $\vec{x}(t) : \mathbb{R}_t \rightarrow \mathbb{R}^3_{\vec{x}}$ are difficult. Indeed the forces that act on the particle are very

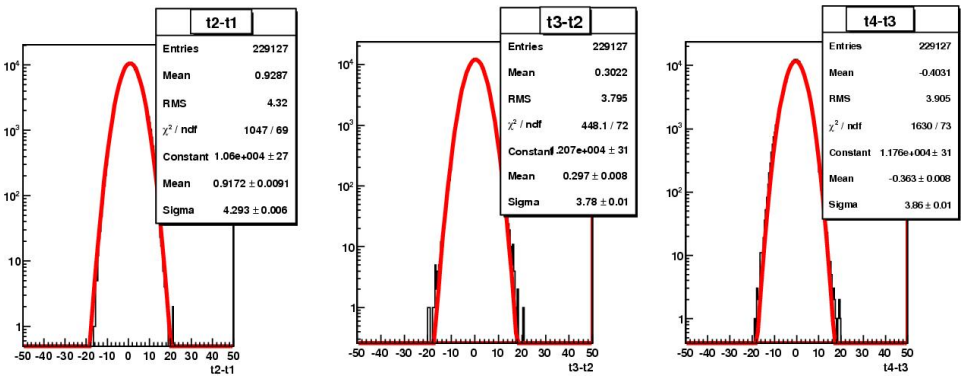

Figure 4.12: $(\Delta t_j^n)_{j=1,2,3}$ *distributions for cosmic data.*

complicated to describe: in addition to the magnetic force there are also the particle energy losses and the possibility of multiple scattering. There is also the finite precision in the measurement of initial position and momentum that makes difficult to propagate in space and time the informations from the information relative to one point of the particle trajectory. What we can do from an experimental point of view is to measure as more features of the particle motion as possible. The more information we have the more we will be able to reconstruct the whole particle motion $\vec{x}(t)$. Let's summarize the available information relative to a cosmic muon standalone leg:

- 3D position of every segment
- Time t of every segment
- Position of the impact point IP

We see that for each segment we have both the spatial and the temporal information. We want now to associate a time parameter t similar to a segment's one to the IP. By knowing the position of the segments and the IP and times of the segments together with the speed of a cosmic muon that is always $\sim c$ we can associate a time t_{IP} to the IP by using the formula:

$$t_{IP} = t_k + \frac{|\vec{x}_k - \vec{x}_{IP}|}{c} - \frac{\left|\vec{x}_k\big|_{(x,y)} - \vec{x}_{IP}\big|_{(x,y)}\right|}{c} \qquad \text{for the upper sectors}$$

$$t_{IP} = t_k - \frac{|\vec{x}_k - \vec{x}_{IP}|}{c} + \frac{\left|\vec{x}_k\big|_{(x,y)} - \vec{x}_{IP}\big|_{(x,y)}\right|}{c} \qquad \text{for the lower sectors}$$

where k is the index relative to the kth segment. The formula is different between upper and lower sectors because of the fact that cosmic muons come from the top of CMS and thus they arrive at the IP after crossing the upper

sectors and before crossing the lower ones. Note that we don't consider the track curvature in magnetic field. This fact will lead to a not negligible error. This t_{IP} is a time parameter similar to the t_k of the segments: the t_{IP} will be equal to t_k if the cosmic muon travels the average path, otherwise t_{IP} will be larger or smaller than t_k if the cosmic muon travels a longer or shorter path than the mean one. For a standalone leg we can have up to four t_k. We can thus average on the k index to improve the resolution of t_{IP}.

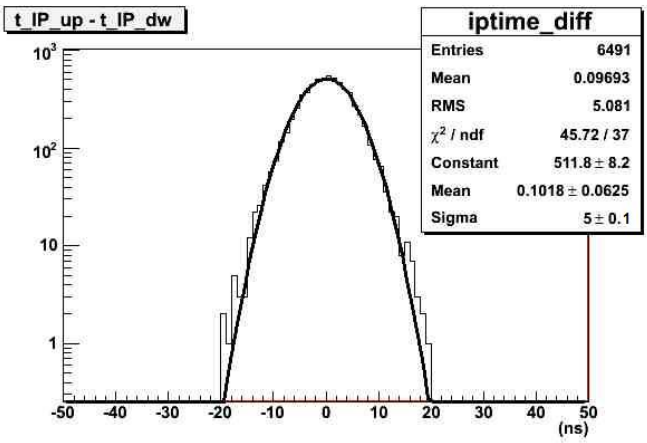

Figure 4.13: $t_{IP}^{up} - t_{IP}^{dw}$ *distribution.*

In order to test our algorithm for t_{IP} we proceed as follows:

- We select the cosmic events where we have a muon crossing the whole CMS detector leaving two standalone legs. An example of such event is reported in Fig. 3.7. We select the events by requiring compatibility between the two standalone leg parameters.

- We estimate t_{IP} for the upper (t_{IP}^{up}) and lower (t_{IP}^{dw}) leg by averaging in the four available $(t_{IP,k})_{k=1,2,3,4}$.

- Belonging to the same muon track t_{IP}^{up} and t_{IP}^{dw} would be equal, so we calculate the difference $t_{IP}^{up} - t_{IP}^{dw}$. Then we fill an histogram with all the differences $t_{IP}^{up} - t_{IP}^{dw}$.

The histogram of $t_{IP}^{up} - t_{IP}^{dw}$ distribution is shown in Fig. 4.13.

We see that, as expected, the distribution is Gaussian with a $\sigma = 5.0$ ns . The resolution relative to t_{IP} results

$$\sigma_{t_{IP}} = \frac{\sigma_{(t_{IP}^{up} - t_{IP}^{dw})}}{\sqrt{2}} = 3.5 \text{ ns}$$

The t_{IP} resolution is worse than the resolution relative to t_k: the error in distance estimation $|\vec{x}_k - \vec{x}_{IP}|$ is not negligible. The t_{IP} is estimated using the four times $(t_k)_{k=1,2,3,4}$ and the position information $(\vec{x}_k)_{k=1,2,3,4}$ and $\vec{x}_I P$ and then averaging on the k index. If we had only the time error σ_t we would expect a resolution $\sigma_{t_{IP}} = \frac{\sigma_t}{\sqrt{4}} = \frac{2.8\text{ns}}{2} = 1.4$ ns. Instead we have a $\sigma_{t_{IP}} = 3.5$ ns . So the contribute to $\sigma_{t_{IP}}$ due to the distances is $\sigma_{dist} = \sqrt{\sigma^2_{t_{IP}} - \left(\frac{\sigma_t}{\sqrt{4}}\right)^2} = \sqrt{3.5^2 - 1.4^2} ns = 3.2$ ns. The contribution to t_{IP} resolution due to distances evaluation is thus dominant. The percentages are:

- time contribution: $\frac{\sigma_t^2/4}{\sigma^2_{t_{IP}}} = 16\%$
- space contribution: $\frac{\sigma^2_{dist}}{\sigma^2_{t_{IP}}} = 84\%$

4.2.4 Time resolution comparison between real cosmic data results and MC cosmic simulated data

A MC simulated cosmic data sample is available [34] [35]. There are still absolute offsets in the t_0 distributions. As done for the real data in section 4.2.1 we subtract them to time parameters. If our analysis on real data is correct its results will have to be in agreement with the simulation.

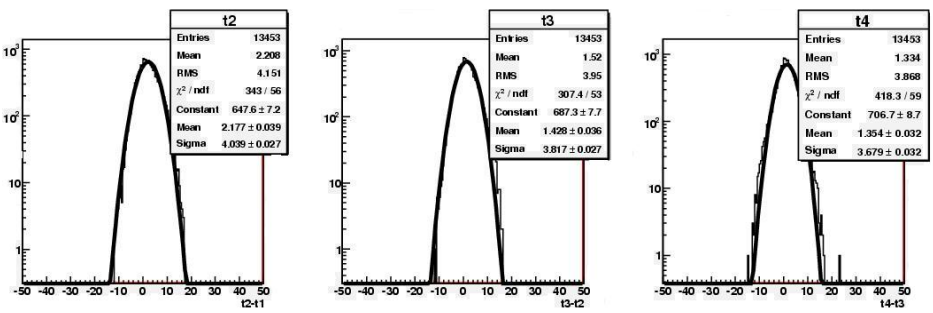

Figure 4.14: $(\Delta t^n_j)_{j=1,2,3}$ *distributions for MC simulated cosmic data.*

In Fig. 4.14 are reported, for MC data, the histograms of Δt^n. The average on these three distributions give a mean $\sigma_{\Delta t^n} = 3.65 \pm 0.21$ ns that lead to a single time resolution:

$$\sigma_t = \frac{\sigma_{\Delta t^n}}{\sqrt{2}} = 2.59 \pm 0.15\text{ns}$$

The histogram of $t^{up}_{IP} - t^{dw}_{IP}$ distribution for MC simulated cosmic data is shown in Fig. 4.15.

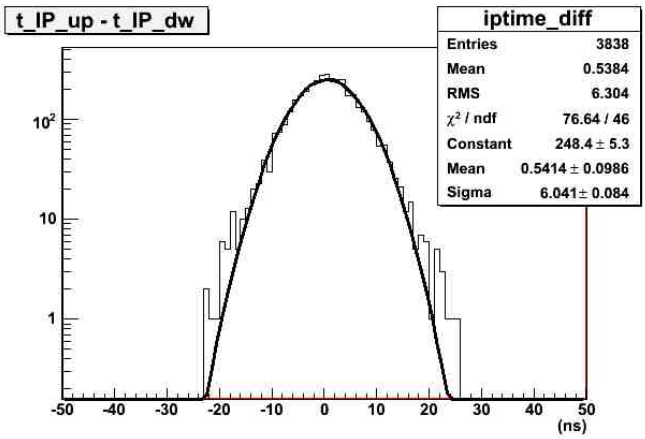

Figure 4.15: $t_{IP}^{up} - t_{IP}^{dw}$ *distribution for MC simulated cosmic data.*

The distribution is Gaussian with a $\sigma = 6.0$ ns. The resolution relative to t_{IP} results $\sigma_{t_{IP}} = 4.25$ ns .

We see that the time resolutions we obtain using real cosmic data are compatible with those predicted by the simulation. There are few differences that would require a detailed analysis on the systematics in the MC data construction. We are not interested in a detailed analysis of the MC data so we limit to show that the results are compatible.

4.2.5 DT time resolution for synchronous particles

In order to perform all the analysis on the LHC data we need to develop an algorithm for the speed evaluation to be applied to muons created by collisions, which have a different topology with respect to cosmic muons: they come from a small region around the interaction point and they are synchronous with the machine clock.

In order to evaluate the DT time resolution at the LHC, when mostly synchronous particles will reach the muon detection system, we use a MC data set [36] with muons in the final state. The analysis on the MC can be done using exactly the same data collections of cosmic data (described in section 3.3). The only difference is that we use data collection class *StandAloneMuons* in place of *TrackCollection*. This class contains tracks with the constraints to come from the primary interaction vertex. For every segment composing a track we have, as usual, the time parameter t and the position $\vec{x}_k$.

The time parameters t are already corrected for the signal time of propagation, for the angle of incidence and other offset effects. MC data have

the quality of the data taken in the best experimental conditions.

Muons in the pp simulation comes from a small space region around the interaction vertex and are all created every 25 ns. The normalization of times t for data relative to synchronous muons is different than normalization for cosmic data. Synchronization of drift tubes is made to ensure that a muon coming from the interaction vertex and traveling the mean path produces a track with all times equal to zero. The difference with respect to the cosmic rays is that now a particle reaching the muon detection system travels for a path that can deviate little from the mean one. We assume, for each event, the time at the production to be always equal to zero since, for every bunch crossing, the interaction occur within a 0.3 ns wide time interval.

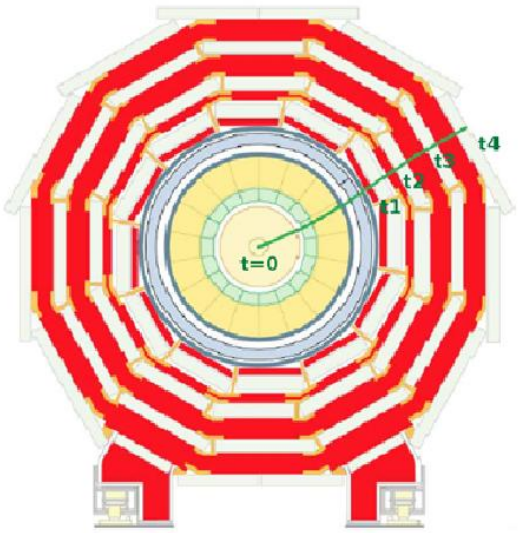

Figure 4.16: *Time parameters for a prompt particle. The time at the interaction vertex is zero within 0.3 ns .*

Fig. 4.16 shows the time parameters t for a particle coming from a pp interaction. The time of creation of the particle is zero within 0.3 ns. If the particle travels at the speed of light all the segment parameters $(t_k)_{k=1,2,3,4}$ will be equal to zero within the time resolution. Only if a particle had $\beta < 1$ its segments would have time parameters t_k different from zero.

We perform on the MC data the same analysis of section 4.2.3, using the time differences Δt_k. We require the $\mathrm{RMS}_{\Delta t_i} < 3 \cdot \sigma(\mathrm{RMS}_{\Delta t})$. The results we obtain are reported in Fig. 4.17 .

The obtained single time parameter t resolution is

$$\sigma_t = \frac{\sigma_{\Delta t}}{\sqrt{2}} = 1.86 \pm 0.24\mathrm{ns}$$

We see that for synchronous particle from pp interactions we expect to

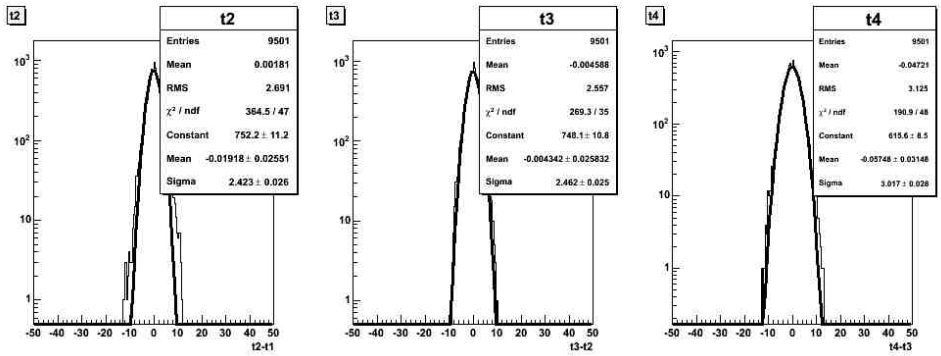

Figure 4.17: $(\Delta t_j)_{j=1,2,3}$ *distributions for MC simulated pp muons.*

achieve much better time resolution with respect to the cosmic data. The MC data, as described before, simulates the detector response to physical events in the best experimental conditions. From a practical point of view we need to optimize the detecting system (in term of calibration and correction for systematic effects) to be able to reach such time resolution.

4.3 β measurement

In the previous section we have seen how to refer the time parameters t_0 coming from segment reconstruction to an absolute time scale $\mathbb{R}_t$ that have a precise physical meaning. Thus now we have enough space-temporal information to evaluate the speed of particles. In this section we will firstly see what is the resolution in the $\beta = v/c$ parameter we can reach using the cosmic data. Then we will extend our analysis to prompt pp muons MC simulated data.

The topology characteristic of the cosmic muons is different from the topology of the prompt pp muons, so we must develop different algorithms for β calculation to be applied to cosmic muons and pp muons. All these algorithms will be based on times and distances evaluation. A good resolution in β is necessary in order to separate muons from HSCP candidates at the LHC. We will evaluate the β resolution and its sources of uncertainty.

4.3.1 β measurement for cosmic data

The first β estimation can be done considering separately the data relative to each one standalone leg for each event. Obviously in this way we will not reach a good resolution since the time resolution is of the order of ~ 3 ns and the time of flight of muons inside one standalone leg (~ 3 m long) is of the order of ~ 9 ns . Anyway, just to start, let's evaluate the β parameter

for each standalone leg using the formula

$$\beta_{ij}^{-1} = \frac{c \cdot \Delta t_{ij}^{n} + \langle d_j \rangle}{\langle d_j \rangle}$$

where i is the measurement index, $j = 1, 2, 3$ the couple-of-chambers index, Δt_{ij}^{n} the normalized time difference between successive chambers defined in section 4.2.3.

Using only standalone legs composed by four segments we can average on the j index since we have always three β estimations.

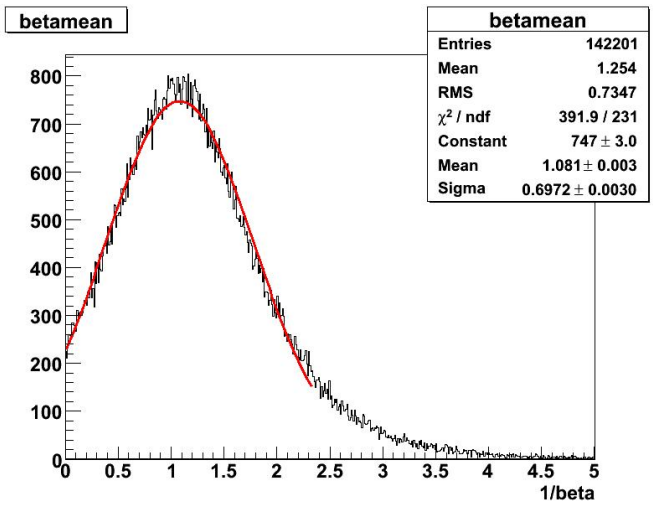

Figure 4.18: β^{-1} *distribution.*

We plot the $\langle \beta_{ij}^{-1} \rangle_j$ distribution in Fig. 4.18. We see that, as expected, we have a bad resolution: $\frac{\sigma_{\beta^{-1}}}{\beta^{-1}} \simeq 70\%$.

Improving the β resolution

We must improve the resolution in the measurement of β parameter of the tracks. Since we cannot improve the time resolution the only way is to consider larger traveled distances. Moreover to consider only the information available inside one only standalone leg per event is too restrictive: at the LHC running we will have the times relative to all the pp interactions. Indeed the pp collisions will occur every 25 ns within a 0.3 ns wide time interval. This means to have at our disposal, for each event, the time-zero relative to the particle instant of creation at the interaction vertex, thus it will be possible to measure the particle speed considering the path from the center of CMS ($\sim$ 7 m long).

For cosmic data analysis we can use the time parameter relative to the interaction point t_{IP} described in section 4.2.3 to have a "time-zero" for a close to vertex position. t_{IP} is calculated from the segment times of a standalone leg $(t_k)_k = 1, 2\ldots$ assuming a particle traveling at the speed of light, as described in section 4.2.3. Thus if we used the information of one standalone leg to evaluate both the t_{IP} and β we would incur in a logical bias since the t_{IP} that would be used to calculate β already contains the assumption that $\beta = 1$.

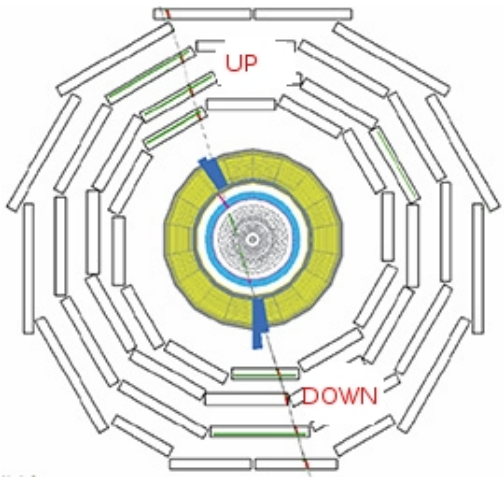

Figure 4.19: *Event selection: we require a muon that cross the whole detector leaving two standalone leg.*

What can be done is to use the cosmic events which contains a cosmic muon crossing the whole CMS detector leaving two standalone legs (events already used in section 4.2.3). We call the upper standalone leg SA^{up}, the lower SA^{dw} (see Fig. 4.19). We can calculate the t_{IP} from the SA^{up}, then we use this t_{IP}^{up} as time zero for the SA^{dw} and vice-versa. In this way we avoid the logical bias. We can have up to four β estimations, one for each chamber. We calculate β^{-1} using the formula:

$$(\beta^{-1})_{ij}^{dw} = \frac{c \cdot (t_{ij}^{dw} - t_{IP,i}^{up}) + \left| \vec{x}_{ij}^{dw}\big|_{(x,y)} - \vec{x}_{IP,i}^{up}\big|_{(x,y)} \right|}{|\vec{x}_{ij}^{dw} - \vec{x}_{IP,i}^{up}|} \qquad \text{for the } SA^{dw}$$

$$(\beta^{-1})_{ij}^{up} = \frac{c \cdot (t_{IP,i}^{dw} - t_{ij}^{up}) + \left| \vec{x}_{ij}^{up}\big|_{(x,y)} - \vec{x}_{IP,i}^{dw}\big|_{(x,y)} \right|}{|\vec{x}_{ij}^{up} - \vec{x}_{IP,i}^{dw}|} \qquad \text{for the } SA^{up}$$

Where i is the measurement index, $j = 1, 2, 3, 4$ the chamber index, the apex ^{dw} refers to quantity calculated from SA^{dw} data, apex ^{up} refers to quantity calculated from SA^{up} data.

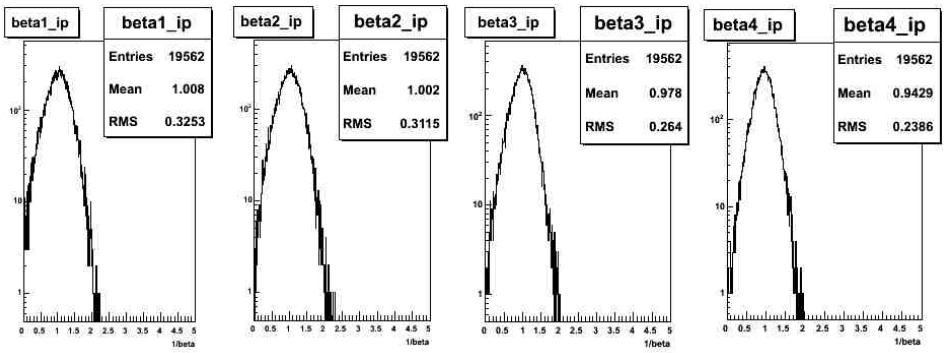

Figure 4.20: $(\beta_j^{-1})_{j=1,2,3,4}$ *distributions.*

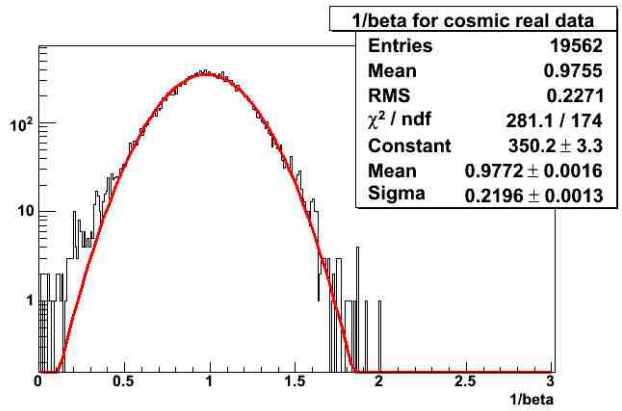

Figure 4.21: $\langle\beta^{-1})_{ij}\rangle_j$ *distribution.*

We plot in Fig. 4.20 the four distributions $(\beta_j^{-1})_{j=1,2,3,4}$.

We see that the resolution becomes better for the farthest chambers since the distance increases. In order to improve the resolution, for each measurement i, we can average on the j index $\langle\beta_{ij}^{-1}\rangle_j$ considering the r.m.s. of the distributions of figure 4.20 as weights $(w_1, w_2, w_3, w_4) = (0.32, 0.31, 0.26, 0.23)$. We can also perform a cut on the r.m.s. of the $\langle\beta^{-1})_{ij}\rangle_j$:

$$\mathrm{RMS}_{\beta_i^{-1}} = \sqrt{\frac{\sum_{j=1}^{4}(\beta_{ij}^{-1} - \langle\beta_{ij}^{-1}\rangle_j)^2}{3}} < 3 \cdot \sigma(\mathrm{RMS}_{\beta_i^{-1}})$$

The $\langle\beta^{-1})_{ij}\rangle_j$ distribution is shown in figure 4.21. We obtain the resolution:

$$\frac{\sigma_{\beta^{-1}}}{\beta^{-1}} = \frac{\sigma_\beta}{\beta} = 22\%$$

Sources of uncertainty in β estimation

Let's analyze what are the quantities that contribute to β^{-1} resolution $\sigma_{\beta^{-1}} = 0.22$ For each event, the β estimation has been performed using the following formula:

$$\langle(\beta^{-1})_{ij}\rangle_j = \frac{\sum_{j=1}^{j=4} \frac{1}{w_j^2} \frac{c\cdot(\pm t_{ij} \mp t_{IP,i}) + d_{\perp,ij}}{d_{ij}}}{\sum_{j=1}^{j=4} \frac{1}{w_j^2}} \tag{4.4}$$

The variables inside this formula are:

- The chambers time parameters t_{ij}
- The time at the impact point $t_{IP,i}$
- The distances d_{ij}

From section 4.2.3 we know the intrinsic resolution of the times:

- $\sigma_t = 2.8$ ns
- $\sigma_{t_{IP}} = 3.4$ ns

We can use the error propagation for formula 4.4 to evaluate the contribute of time resolution to the global $\sigma_{\beta^{-1}} = 0.22$. Propagating the errors for formula we have:

$$\sigma_{\beta^{-1}} = \sqrt{f_t^2 + f_{t_{IP}}^2 + f_{dist.}^2 + f_{corr.}} =$$

$$= \sqrt{\sum_{j=1}^{4} \left(\frac{\partial\beta^{-1}}{\partial t_j}\right)^2 \sigma_{t_j}^2 + \sum_{j=1}^{4} \left(\frac{\partial\beta^{-1}}{\partial t_{IP}}\right)^2 \sigma_{t_{IP}}^2 + f_{dist.}^2 + f_{corr.}}$$

We can write down explicitly the time terms as:

- $f_t^2 = \sum_{j=1}^{4} \left(\frac{\partial\beta^{-1}}{\partial t_j}\right)^2 \sigma_{t_j}^2 = \frac{c^2\sigma_t^2 \sum_{j=1}^{4} \frac{1}{w_j^4}\left(\frac{1}{\langle d_j\rangle^2}\right)}{(\sum_{j=1}^{4} 1/w_j^2)^2}$
- $f_{t_{IP}}^2 = \sum_{j=1}^{4} \left(\frac{\partial\beta^{-1}}{\partial t_{IP}}\right)^2 \sigma_{t_{IP}}^2 = \frac{c^2\sigma_{t_{IP}}^2 \sum_{j=1}^{4} \frac{1}{w_j^4}\left(\frac{1}{\langle d_j\rangle^2}\right)}{(\sum_{j=1}^{4} 1/w_j^2)^2}$

The correlation effect is expected to be small because the times t_j and t_{IP} are measured independently for the two standalone legs. Moreover the correlation between the times and the distances would be small because the main errors in the distances evaluation come from the extrapolation of the track in the central zone of CMS. In Fig. 4.22 are shown the scatter plots

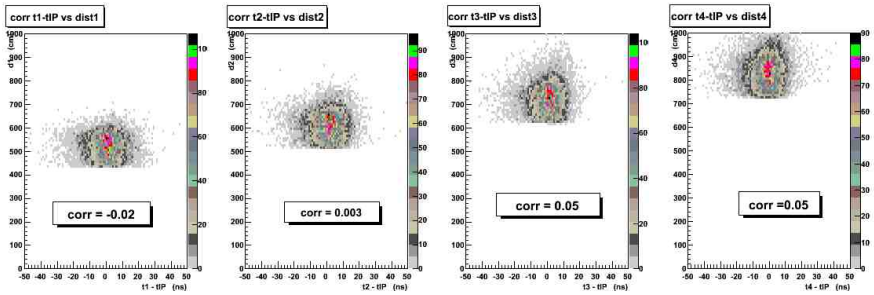

Figure 4.22: *Scatter plots:* $t_j^{dw} - t_{IP}^{up}$ *vs* d_j

of distances d_j as function of times $t_j^{dw} - t_{IP}^{up}$. These plots show that there is no correlation between these variables. Thus we can pose $f_{corr.} = 0$.

The relative weights of the two time variables in the final resolution $\sigma_{\beta^{-1}}$ can be evaluated:

- $\frac{f_t^2}{\sigma_{\beta^{-1}}^2} = 11\%$
- $\frac{f_{t_{IP}}^2}{\sigma_{\beta^{-1}}^2} = 19\%$

The time uncertainty contribute for a 30% to the β^{-1} resolution. The remaining 70% has to be linked to the distances estimation. As previously shown in section 4.2.3 for the t_{IP}, the track extrapolation trough the central zone of CMS toward the impact point lead to the most relevant sources of uncertainty.

4.3.2 Comparison between real cosmic data results and MC cosmic simulated data

We now perform the same analysis of the previously section 4.3.1 on the MC simulated cosmic data already used in section 4.2.5

The $\langle\beta^{-1})_{ij}\rangle_j$ distribution is reported in figure 4.23

We obtain a resolution of $\frac{\sigma_\beta}{\beta} \simeq 26\%$, similar to the resolution obtained in 4.3.1 for real data.

We thus have another confirmation that our results are almost well reproduced by simulation.

4.3.3 β measurement for MC pp simulated data

In order to develop an algorithm for β estimation for synchronous particles from pp interaction we have at our disposal two Montecarlo simulated data

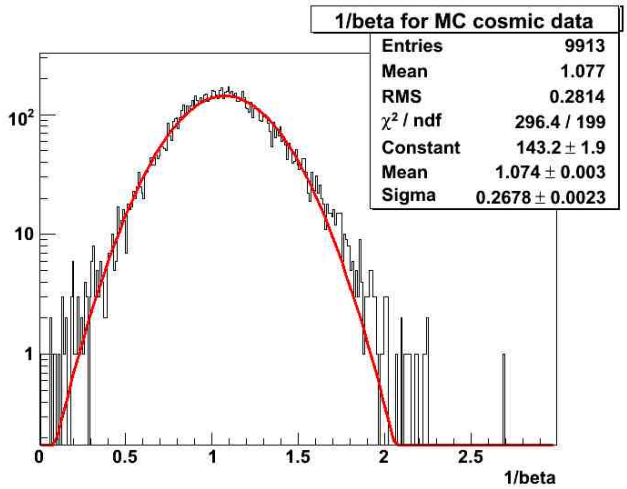

Figure 4.23: $\langle\beta^{-1})_{ij}\rangle_j$ *distribution for MC simulated cosmic data.*

set. Both contain muons in the final state. The MC first contains the simulation of the physical process $pp \to J/\psi \to \mu\mu$ [36], the second, more generally, is a simulation of processes that contain almost a muon in the final state $pp \to \mu X$ [36].

We expect, for MC pp simulated data, a better β^{-1} resolution than the $\sigma_{\beta^{-1}}$ obtained in section 4.3.1 for cosmic data. The uncertainty due to t_{IP} would be now absent since the bunch crossing time is know within 0.3 ns; this lead to a reduction at least of the 19% of $\sigma_{\beta^{-1}}$ (see section 4.3.1). Even the t resolution for MC pp data is smaller than the cosmic t resolution, as calculated in section 4.2.5.

The most relevant effect is expected to act on the 70% of the β^{-1} resolution fraction due to distances. Indeed the CMS design has been optimized to see the collisions products. Muons from pp collisions come from a small space region around the interaction vertex, and the standalone reconstruction itself has been designed in order to reconstruct particles coming from the center of CMS.

We estimate beta parameter from MC stand alone tracks using the formula:

$$\beta_{ij}^{-1} = \frac{c \cdot t_{ij} + |\vec{x}_{ij} - \vec{x}_{IP,i}|}{|\vec{x}_{ij} - \vec{x}_{IP,i}|}$$

where i is the measurement index, j the chamber index. The $|\vec{x}_{IP,i}|$ is expected to be $\simeq 0$.

For each measurement i, we average on the j index [5] $\langle\beta^{-1})_{ij}\rangle_j$ in order to improve the resolution. We also perform a cut on the r.m.s. of the $\langle\beta^{-1})_{ij}\rangle_j$:

[5] Now we require the presence of at least three segments per standalone track.

we require the ith r.m.s. to be below the 3σ.

$$\text{RMS}_{\beta_i^{-1}} = \sqrt{\frac{\sum_{j=1}^{N}(\beta_{ij}^{-1} - \langle\beta_{ij}^{-1}\rangle_j)^2}{N-1}} < 3 \cdot \sigma(\text{RMS}_{\beta_i^{-1}})$$

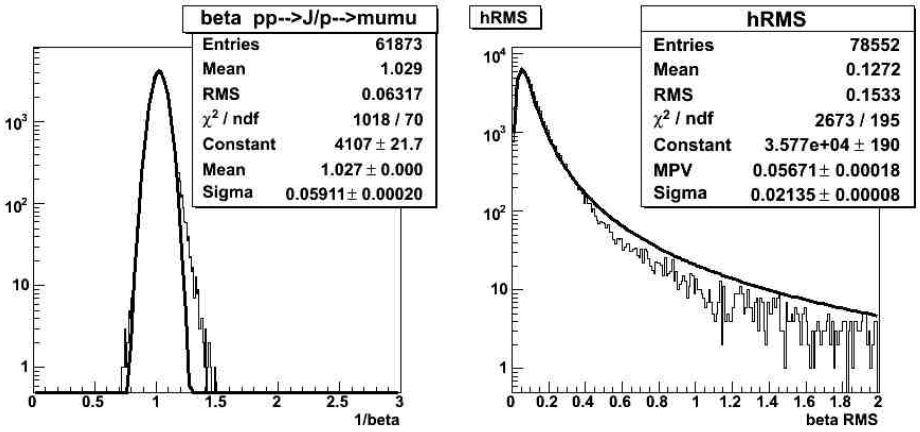

Figure 4.24: $\langle\beta^{-1})_{ij}\rangle_j$ *and* $RMS_{\beta_i^{-1}}$ *distribution for MC* $pp \to J/\psi \to \mu\mu$

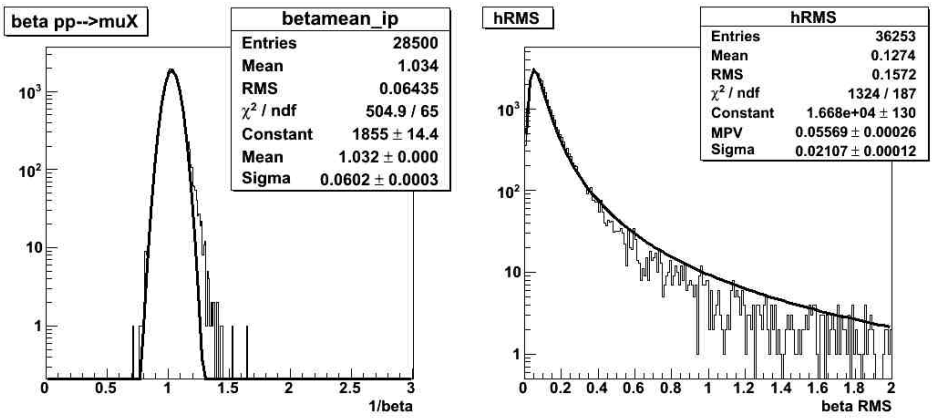

Figure 4.25: $\langle\beta^{-1})_{ij}\rangle_j$ *and* $RMS_{\beta_i^{-1}}$ *distribution for MC* $pp \to \mu X$

The $\langle\beta^{-1})_{ij}\rangle_j$ distribution for MC $pp \to J/\psi \to \mu\mu$ is shown in figure 4.24 together with the $\text{RMS}_{\beta_i^{-1}}$ distribution.

The $\langle\beta^{-1})_{ij}\rangle_j$ distribution for MC $pp \to \mu X$ is shown in figure 4.25 together with the $\text{RMS}_{\beta_i^{-1}}$ distribution.

For both our MC data samples we obtain a resolution

$$\frac{\sigma_\beta}{\beta} \simeq 6\%$$

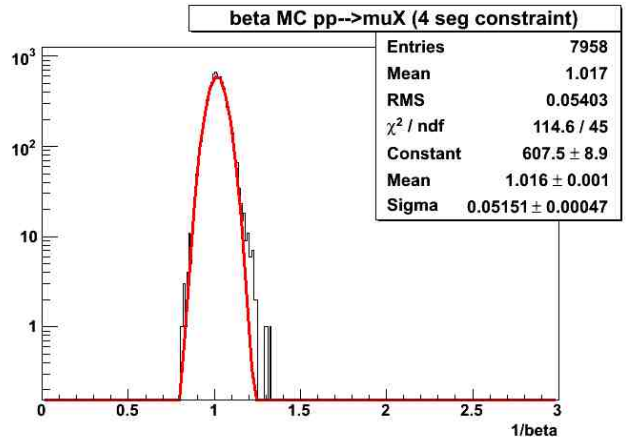

Figure 4.26: $\langle\beta^{-1})_{ij}\rangle_j$ *distribution for MC pp* $\rightarrow \mu X$ *. Four segment per standalone leg are required.*

We note the presence of some tails around the highest values of β^{-1}. If we require the presence of four segments per standalone track the tails are almost totally cut as shown in Fig. 4.26 and the resolution results

$$\frac{\sigma_\beta}{\beta} = 5.1\%$$

Let's estimate the contribute of time uncertainty $\sigma_t = 1.86$ ns to β^{-1} resolution $\sigma_{\beta^{-1}} = 0.051$. Using the formulas of section 4.3.1 we find:

$$\frac{f_t^2}{\sigma_{\beta^{-1}}^2} = 97\%$$

So if we had only the time uncertainty σ_t we would obtain the β^{-1} resolution:

$$\sigma_{\beta^{-1}} = |f_t| = |\sigma_t|\sqrt{\sum_{j=1}^{4}\left(\frac{\partial\beta^{-1}}{\partial t_j}\right)^2} = 0.049$$

We thus conclude that now the $\sigma_{\beta^{-1}}$ is dominated by σ_t effect as we expect.

We have seen that the most relevant difference between cosmic and pp data is due to distances estimation. The time resolution of MC pp data is

$\sigma_t = 1.86$ ns and, dominating the β^{-1} resolution, leads to a $\sigma_{\beta^{-1}} = 0.051$. Nevertheless, as told in section 4.2.5, the time resolution $\sigma_t = 1.86$ predicted by the MC will be very difficult to reach with real data since it would require perfect calibration and correction of the systematic effects. So let's see what would be the $\sigma_{\beta^{-1}}$ if we had the more relaxed $\sigma_t = 2.8$ ns ,that we have measured from our real cosmics, in a scenario where $\sigma_{\beta^{-1}}$ is dominated by the time resolution σ_t :

$$\sigma_{\beta^{-1}} = |f_t| = |\sigma_t| \sum_{j=1}^{4} \sqrt{\left(\frac{\partial \beta^{-1}}{\partial t_j}\right)^2} = 0.073$$

Even having a time resolution $\sigma_t = 2.8$ (which is an upper limit to our performance, as it was already measured with cosmics) we would reach a good resolution for β^{-1} measurement.

4.4 HSCP data sample analysis: $^{KK}\tau$

We now analyze a MC data sample that simulates the production at the LHC of kaluza-klein $^{kk}\tau$ [37]. $^{KK}\tau$ are massive (300 GeV) muon-like particles predicted by universal extra dimensions theories (UED). These particles, being so massive, are predicted to have beta significantly lower than 1.

We have available for the analysis both segment and track information (classes *standAloneMuons* and *DTRecSegment4DCollection*). This data sample contains no trigger information. So the time parameters t of the segments are computed assuming the correct bx assignment.

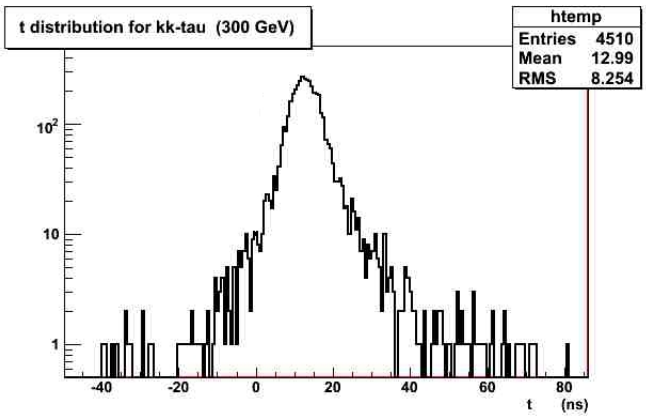

Figure 4.27: *Time parameter t of DT segments distribution for $^{KK}\tau$ data sample.*

The time parameter t distributions for all the segments is shown in Fig. 4.27. As expected these HSCPs reach the Drift Tubes chambers out of

time because of their low speed, so it will be possible to measure their β parameter.

In order to have an idea of the statistic reduction in the $^{KK}\tau$ data sample caused by the quality cuts we report in the following table a summary of our data sample characteristics. We indicate the fraction $\frac{SA_N}{SA}$ of standalone legs composed by N segments and the fraction $\frac{Seg_n}{Seg}$ of segment composed by n hits in the ϕ view.

Standalone tracks	
SA_{4st}/SA_{all}	29%
SA_{3st}/SA_{all}	33%
SA_{2st}/SA_{all}	26%
SA_{1st}/SA_{all}	12%
Segments	
$Seg_{8layers}/Seg_{all}$	48%
$Seg_{7layers}/Seg_{all}$	17%
$Seg_{6layers}/Seg_{all}$	12%
$Seg_{5layers}/Seg_{all}$	7%
$Seg_{4layers}/Seg_{all}$	11%
$Seg_{3layers}/Seg_{all}$	5%

4.4.1 β measurement for $^{KK}\tau$

In order to evaluate the beta parameter for standalone tracks we apply the same algorithm used for pp muons in section 4.3.3, also requiring the presence of at least three segments for each stand alone track and posing the constraints on the beta RMS:

$$\beta_{ij}^{-1} = \frac{c \cdot t_{ij} + |\vec{x}_{ij} - \vec{x}_{IP,i}|}{|\vec{x}_{ij} - \vec{x}_{IP,i}|}$$

$$\mathrm{RMS}_{\beta_i^{-1}} = \sqrt{\frac{\sum_{j=1}^{N}(\beta_{ij}^{-1} - \langle\beta_{ij}^{-1}\rangle_j)^2}{N-1}} < 3 \cdot \sigma(\mathrm{RMS}_{\beta_i^{-1}})$$

where i is the measurement index, j the chamber index and N the number of segments per standalone track.

We obtain the results shown in Fig. 4.28. The β^{-1} distribution for $^{KK}\tau$ is shown together with the distribution of prompt muons. β^{-1} values for $^{KK}\tau$ (red) are distributed almost uniformly between 1.5 and 2. The tails of the distributions extends up to 2.3 and down to 1.3 . We see that the two distributions are almost totally separated with the resolution for prompt muons ($\frac{\sigma_\beta}{\beta}\big|_{\beta=1} = 6\%$).

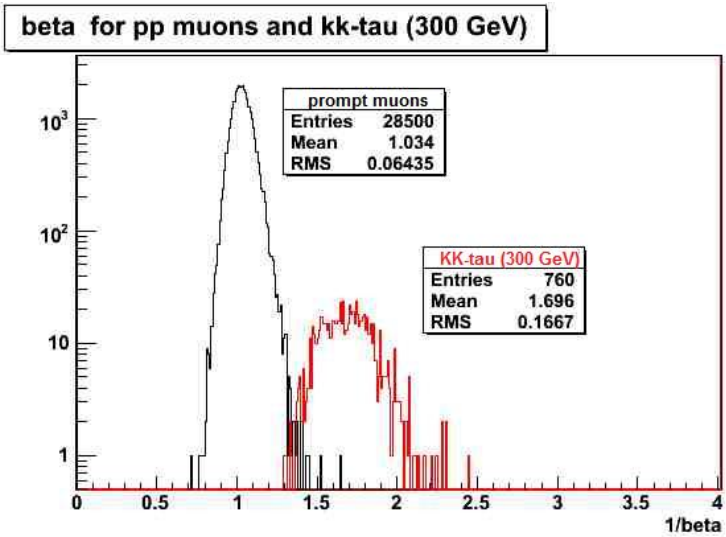

Figure 4.28: *β^{-1} distribution for ${}^{KK}\tau$ is together with the distribution of prompt muons.*

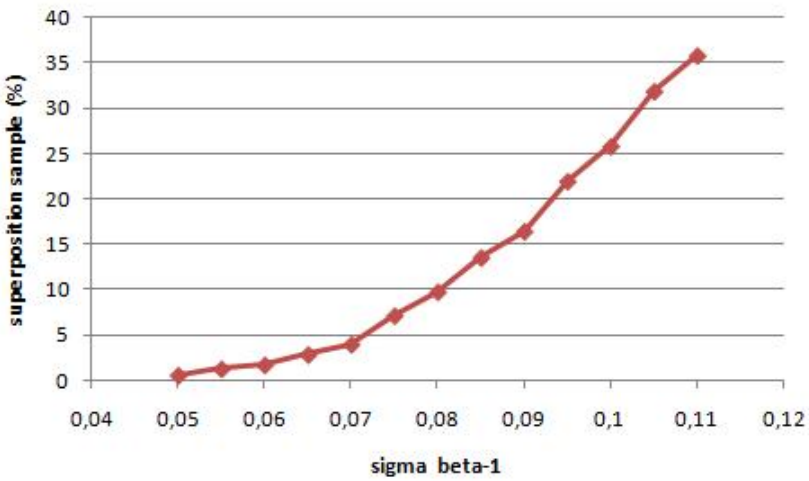

Figure 4.29: *Percentage of events of the ${}^{KK}\tau$ sample that superposes to muon β^{-1} Gaussian distribution as function of $\sigma_{\beta^{-1}}$*

The resolution we have for MC pp muons is very good, there is almost no superposition between HSCP and muons. We can thus evaluate what would be the percentage of HSCP sample that would superimpose to prompt muons range at lower resolutions. In Fig. 4.29 is shown the percentage of events of the ${}^{KK}\tau$ sample that superposes to muon β^{-1} Gaussian distribution as

function of $\sigma_{\beta^{-1}}$. The considered range of β^{-1} prompt muons Gaussian distribution is $[\langle\beta^{-1}\rangle - 5\sigma, \langle\beta^{-1}\rangle + 5\sigma]$.

It is clear that, even at the lower beta resolution computed with the worse-case time resolution , the two distributions are well separated.

Conclusions

Almost all the analysis we have developed in this thesis work are based on the segment reconstruction performed using the *3-parameters fit*. Starting by a time parameter t_0 assigned, together with the 3D position information, to each segment in the off-line reconstruction procedure we have developed two independent analysis: the DT local trigger fine synchronization and the particle speed evaluation. Let's analyze separately the results we have obtained for the two analysis.

DT local trigger fine synchronization

In chapter 3 we have developed a method for DT local trigger fine synchronization based on cosmic data analysis. Many algorithms for fine synchronization already exist, based both on trigger and TDC data but are all based on the so called "delay scan", that means a lot of data acquisition "runs" with different delay settings. The fine synchronization performed using cosmic data has the advantage of using only one, fixed delay setting and to find out the best delays values for all the chambers by exploiting the flat distribution in time of the cosmic rays and the time parameters t_0 assigned to the track segments.

In addition to this we have pointed out the fact that the trigger efficiency is an effect due to hardware system of the chambers: stations of the same type have the same trigger efficiency dependence from the absolute "clock time", i.e. the time reference equipped within all the chambers by the TTC system. This is very important since means that at the LHC start-up, when the time of passage of synchronous muons inside all the DT chambers will be know within a sufficiently tight time interval, we will be able to individuate immediately the correct delay setting that must be applied to each station, being the "clock time" an absolute time frame of reference always available.

We conclude that thanks to this analysis at the LHC start-up will be possible to perform the DT trigger fine synchronization almost immediately, using only few hundreds of events per chamber.

Separation between HSCP candidates and muons using the DT chambers data

The chapter 4 has been devoted to speed evaluation for the particles that cross the muon detection system. This is central in order to separate HSCP candidates from the muons background. The algorithm for β parameter estimation is based both on temporal and spatial information of the track segments.

In section 4.4.1 the β estimation for an HSCP sample leads to the conclusion that a resolution $\frac{\sigma_\beta}{\beta}\big|_{\beta=1}$ smaller than $\sim 10\%$ is required at the LHC running in order to have good separation between HSCP candidates and muons background.

The β estimation for cosmic data, MC pp simulated data (sections 4.3.1 and 4.3.3) and the analysis on its sources of uncertainty (sections 4.3.1 and 4.3.3) show that a good resolution in β is obtainable even with the time resolution that we actually measure for cosmic real data ($\sigma_t \sim 3$ ns) if the distances are correctly evaluated.

The main sources of uncertainty in β estimation for cosmic data are linked to distances (section 4.3.1). This comes from the imperfect reconstruction of the cosmic standalone. At the LHC we will reach a much better reconstruction of the particles paths as shown by the MC simulated data since the topology of the pp collisions will be exploited and the magnetic field correctly mapped. In addition the tracker will be used to improve the path estimation. In this case the β resolution will dominated by the time uncertainty σ_t as show in section 4.3.3.

The σ_t we actually measure for real cosmic data is 2.8 ns . In a scenario were the σ_β is dominated by time resolution we obtain $\frac{\sigma_\beta}{\beta}\big|_{\beta=1} = 7.5\%$, that is a good result. However we can aspire to a better time resolution with the LHC collisions data: again the topology of pp collisions will be exploited. With the chambers uniformly illuminated it will be possible to perform a better time pedestal calibration and systematic errors correction. The MC data shows that a resolution of the order $\sigma_t \sim 2$ ns ($\frac{\sigma_\beta}{\beta}\big|_{\beta=1} \simeq 5\%$) is possible.

Bibliography

[1] CMS Physics Technical Design report, Vol I: *Detector Performance and Software*, CERN/LHCC 2006-001, CMS TDR 8.1, Cap I

[2] CMS Physics Technical Design report, Vol I: *Detector Performance and Software*, CERN/LHCC 2006-001, CMS TDR 8.1, Cap III

[3] CMS Physics Technical Design report, Vol I: *Detector Performance and Software*, CERN/LHCC 2006-001, CMS TDR 8.1, Cap III

[4] CMS Physics Technical Design report, Vol I: *Detector Performance and Software*, CERN/LHCC 2006-001, CMS TDR 8.1, Cap IV

[5] CMS Physics Technical Design report, Vol I: *Detector Performance and Software*, CERN/LHCC 2006-001, CMS TDR 8.1, Cap V

[6] CMS Physics Technical Design report, Vol I: *Detector Performance and Software*, CERN/LHCC 2006-001, CMS TDR 8.1, Cap VI

[7] CMS Physics Technical Design report, Vol I: *Detector Performance and Software*, CERN/LHCC 2006-001, CMS TDR 8.1, Cap IX

[8] The TEVNPH Working Group, *Combined CDF and DØ Upper Limits on Standard Model Higgs-Boson Production with up to 4.2* fb^{-1} *of Data*, FERMILAB-PUB-09-060-E CDF Note 9713 DØ Note 5889

[9] CMS Technical Design report: *The Trigger and Data Acquisition project, Volume I – The Level-1 Trigger*, CERN/LHCC 2000-038, CMS TDR 6.1, Cap I

[10] CMS Technical Design report: *The Trigger and Data Acquisition project, Volume I – The Level-1 Trigger*, CERN/LHCC 2000-038, CMS TDR 6.1, Cap II

[11] CMS Technical Design report: *The Trigger and Data Acquisition project, Volume I – The Level-1 Trigger*, CERN/LHCC 2000-038, CMS TDR 6.1, Cap VIII

[12] CMS Technical Design report: *The Trigger and Data Acquisition project, Volume I – The Level-1 Trigger*, CERN/LHCC 2000-038, CMS TDR 6.1, Cap IX

[13] CMS Muon Technical Design report, CERN/LHCC 1997-32

[14] N.Amapane et al.: *Offline Calibration Procedure of the CMS Drift Tube Detectors*, 2008

[15] R.Veenhof: *Garfield, a Drift-Chamber Simulation Program User's Guide*,CERN Program Library W5050

[16] M. Benettoni et al.: *CMS DT Chambers: Optimized Measurement of Cosmic Rays Crossing Time in absence of Magnetic Field*, CMS Note-2008/017

[17] F.R. Cavallo et al.: *Test of CMS Muon Barrel Drift Chambers with Cosmic Rays*, CMS Note 2003/017.

[18] Fouz M.C. Et al. , *Measurement of the Drift Velocity in the CMS Barrel Muon Chambers During the CMS Magnet Test and the Cosmic Challenge*, CERN-CMS Note 2008/003

[19] C.Albajar et al.: *Test beam anlysis of the first CMS Drift Tube muon chamber*, Nucl. Instrum. Meth. A 525 (2004)

[20] Bellato,Bellan et al.: *Results on Local Muon Reconstruction in DT chambers from analysis of CRAFT data*, CMS Note 2009/xxx/DRAFT2

[21] R. Fruhwirth, *Application of Kalman Filtering to Track and Vertex Fitting*, Nucl. Instrum. and Methods A262 (1987) 444.

[22] V. Innocente, M. Maire, and E. Nagy, *GEANE: Average Tracking and Error Propagation Package*, CERN Program Library, IT-ASD W5013-E (1991)

[23] M. Aldaya et al.: *Fine synchronization of the muon drift tubes local trigger*,CMS Note-2006/002

[24] M.Meneghelli, A.T.Meneguzzo, *Studio dell'efficienza del "trigger" delle camere a deriva di CMS con raggi cosmici*, Università di Padova, tesi di laurea, 2007

[25] `https://twiki.cern.ch/twiki/bin/view/CMS/ /TMD_HLT_8E29_CRAFT68021`

[26] `http://cms-cpt-software.web.cern.ch/cms-cpt-software/General`

[27] `http://root.cern.ch`

[28] M. Fairbairn et al., Phys. Rept. 438 (2007) 1-63, hepph/0611040

[29] A.Rizzi et al.: *Search for heavy stable charged particle with 100* pb^{-1} *and 1* fb^{-1} *at CMS experiment*, CMS Analysis Note 2007/049

[30] T. Sjostrand, S. Mrenna and P. Skands, JHEP 0605 (2006) 026, hep-ph/0603175

[31] E. Boos et al. (CompHEP Collaboration), Nucl. Instrum. Meth. A 534, 250 (2004).

[32] `http://home.fnal.gov/kckong/mued/`

[33] S. Agostinelli et al., Nucl. Instrum. Meth. A506, 250-303 (2003).

[34] `https://twiki.cern.ch/twiki/bin/view/CMS/CMSCGEN`

[35] Philipp Biallass and Thomas Hebbeker,: *Improved Parametrization of the Cosmic Muon Flux for the Generator CMSCGEN*, CMS IN 2007/033

[36] `https://twiki.cern.ch/twiki/bin/view/CMS/`
`/ProductionSummer2008#Summer08_Full_Simulation_SM_Prod`

[37] `https://twiki.cern.ch/twiki/bin/view/CMS/HscpSample223`